UC San Diego
UC San Diego Electronic Theses and Dissertations

Title

Developing oxide semiconductors and graphene field-effect transistors for next-generation electronic and electrochemical sensing

Permalink
https://escholarship.org/uc/item/2676419c

Author
Lee, Alex Wootae

Publication Date
2023

Peer reviewed|Thesis/dissertation

eScholarship.org Powered by the California Digital Library
University of California

UNIVERSITY OF CALIFORNIA SAN DIEGO

Developing oxide semiconductors and graphene field-effect transistors for next-generation electronic and electrochemical sensing

A Dissertation submitted in partial satisfaction of the requirements
for the degree Doctor of Philosophy

in

Materials Science and Engineering

by

Alex Wootae Lee

Committee in charge:

Professor Prabhakar Bandaru, Chair
Professor Shadi Dayeh
Professor Tse Nga Ng
Professor Yuan Taur

2023

Copyright

Alex Wootae Lee, 2023

All rights reserved.

The Dissertation of Alex Wootae Lee is approved, and it is acceptable in quality and form for publication on microfilm and electronically.

University of California San Diego

2023

DEDICATION

To my family, who supported me throughout my entire Ph.D. study and to my sister, Dr. Sora Lee, who always encouraged and helped me during hardship.

To my academic advisor, Prof. Prabhakar R. Bandaru, who supported and guided me through my Ph.D. research and future career.

TABLE OF CONTENTS

DISSERTATION APPROVAL PAGE iii

DEDICATION iv

TABLE OF CONTENTS v

LIST OF FIGURES vii

LIST OF TABLES xiv

ACKNOWLEDGEMENTS xv

VITA xvii

ABSTRACT OF THE DISSERTATION xviii

INTRODUCTION 1

1. Oxide semiconductor for device applications 1

2. Graphene field-effect transistor (FET) for sensing applications 4

Chapter 2. Hydrogen-Defect Termination in SnO for p-Channel TFTs 8

2.1 Introduction 8

2.2 Experimental Methods 10

2.3 Material Characterization of hydrogen defect terminated SnO 11

2.4 Electrical characterization of hydrogen defect terminated SnO-TFTs 19

2.5 The device and material computation for identifying the origin of subgap defects 25

2.6 Conclusion 30

2.7 Acknowledgement 31

Chapter 3. Switching Mechanism behind the Device Operation Mode in SnO-TFT 32

3.1 Introduction 32

3.2 Experimental Methods 34

3.3 Material Characterization of back-channel engineered SnO film 35

3.4 TFT Characterization of back-channel engineered SnO-TFT ... 38
3.5 Understanding subgap defect density of states (DOS) for back-channel engineered SnO. 48
3.6 Ambipolar SnO-TFT based CMOS-like inverter ... 54
3.6 Conclusion ... 58
3.7 Acknowledgement ... 59
Chapter 4. Towards the ultimate limit of analyte detection in graphene based field-effect transistors ... 60
4.1 Introduction ... 60
4.2 Thermodynamics approach in GFET aptasensor ... 62
4.3 Graphene characterization and device preparation ... 65
4.4 Analyzing *Ap* distribution on graphene surface via EIS and AFM ... 69
4.5 The LoD dependency of GFET aptasensor with varying Ap incubation condition ... 79
4.6 Acknowledgement ... 92
Conclusion and Future Work ... 93
5.1 Summary ... 93
5.2 Future Work ... 96
REFERENCES ... 98

LIST OF FIGURES

Figure 1. 1 (a) The SnO crystal structure, and (b) the schematic representation of the hybridization of valence band maximum (VBM) in SnO. 2

Figure 1. 2 The scheme illustrates a chemical and biosensor configuration consisting of a recognition element (receptor) attached to the transducer to selectively detect the analyte of the interest. The transducer converts the biorecognition event on its surface into a quantifiable signal before transmitting it for further processing. 5

Figure 2. 1 The structure of 10.5 nm SnO films deposited on silica glass substrates. Glancing angle X-ray diffraction patterns of unannealed and annealed SnO film at 250 – 510 ^{o}C. 12

Figure 2. 2 Film parameters extracted from Glancing angle X-ray reflectivity patterns of a unannealed SnO film, and annealed SnO film at 250 ^{o}C, 280 ^{o}C, 330 ^{o}C, 360 ^{o}C, and 390 ^{o}C. (Top) The surface roughness, (middle) film thickness, (bottom) film density are illustrated.. 13

Figure 2. 3 (a) Optical absorption spectra of unannealed and annealed (250-510 ^{o}C) 10.5 nm SnO films. (b) The variation of direct and indirect bandgap of unannealed and annealed SnO films as a function of annealing temperatures. 14

Figure 2. 4 AFM images of (a) unannealed and hydrogen-annealed films at (b) 250 ^{o}C, (c) 360 ^{o}C, and (d) 510 ^{o}C in pure NH_3.. 15

Figure 2. 5 (a) Sn 3d 5/2 and 3d 3/2 and (b) O1s core level spectra for unannealed film and annealed films at 250-450 ^{o}C in NH_3... 16

Figure 2. 6 (a) Hole density of SnO films measured by Hall-effect at room temperature. (b) Bulk SnO channel defect density extracted from the channel thickness dependency of s-values of SnO-TFTs. 17

Figure 2. 7 (a) Hole density of SnO films measured by Hall-effect at room temperature. (b) Bulk SnO channel defect density extracted from the channel thickness dependency of s-values of SnO-TFTs. 18

Figure 2. 8 (a) Variation of transfer characteristics for SnO TFTs with different channel thicknesses of 7.5, 10.5, and 13.5 nm after NH_3 annealing at 280 °C. TFT parameters are as following: (b) V_{TH}, (c) s-value and D_{it}, (d) saturation and linear mobility, and (e) on-to-off current ratio and off current at V_{GS} = 60 V. 19

Figure 2. 9 (a) Variation of the transfer characteristics for unannealed and annealed SnO TFTs with a 7.5 nm thick channel. TFT parameters are as following: (b) V_{TH}, (c) *s*-value and D_{it}, (d) saturation and linear mobility, and (e) on-to-off current ratio and off-current at V_{GS} = 60 V. 22

Figure 2. 10 (a) The variation of transfer characteristics of SnO-TFTs with different channel thickness of 6, 7.5, 10.5 and 15 nm after NH_3 annealing at 360 °C. The listed TFT parameters are (b) V_{TH}, (c) *s*-value and D_{it}, (d) saturation and linear mobility, and e) on-to-off current ratio and off- current level. 24

Figure 2. 11 Measured (symbols) and simulated (lines) transfer curves at V_{DS} = −20 V for (a) the vacuum-annealed, (b) oxygen-annealed, and (c) hydrogen-annealed TFTs. (d)

Corresponding subgap DOSs were extracted from the device simulations for the vacuum-annealed (blue), oxygen annealed (yellow), and hydrogen-annealed TFTs (red). 25

Figure 2. 12 (a) Oxygen vacancy (V_o), (b) tin vacancy (V_{sn}), (c) interstitial site for oxygen (O_i) and hydrogen (H_i), and (d) oxygen vacancy− hydrogen complex (H_o) in SnO. (e) Formation energies of these native defects as a function of Fermi level under Sn-rich limit condition. 27

Figure 2. 13 (a) Transfer characteristics of a p-channel-SnO TFT (red line) with V_{DS} = 10 V and n-channel a-IGZO TFT (blue line) at VDS = 20 V. The dashed lines show $(I_{DS})^{1/2}$−V_{GS} plots. (b) VTCs of the complementary inverter. The input voltage (V_{IN}) was scanned from −6 to +6 V with supply voltages (V_{dd}) of 1−10 V... 29

Figure 3. 1 The GIXRD of SnO films before and after surface wet-etching and ALD-Al_2O_3 passivation at 300 ^oC. The powder diffraction data (PDF #04-005-4540) was used to identify the measured pattern. A halo peak around ~24° is due to the glass substrate. 36

Figure 3. 2 (a) The optical absorption spectra of SnO film before and after surface wet-etching and ALD-Al_2O_3 passivation at 300 ^oC. The $(\alpha h\nu)^2$ vs. hν and $(\alpha h\nu)^{1/2}$ vs. hν plots for (b) pristine, (c) surface-etched, and (d) ALD-Al_2O_3 passivated SnO films. 37

Figure 3. 3 (a) The variation of transfer characteristics for SnO-TFTs before and after back-channel surface defect modification. Output characteristics for (b) pristine, (c) back-channel surface etched, and (d) ALD-Al_2O_3 passivated TFT. The deposition temperature for ALD-Al_2O_3 passivation layer is at 300°C.. 38

Figure 3. 4 The (a) transfer and (b-c) output characteristics of back-channel (BC) etched SnO:H TFTs after ALD-Al_2O_3 BC layer formation at 80 °C and 300 °C.................................... 42

Figure 3. 5 (a) The transfer characteristics of SnO-TFTs with ALD-Al_2O_3 passivated layer deposited at different temperatures. The output characteristics of SnO-TFTs with ALD-Al_2O_3 temperature at (b) 80 °C (c) 200 °C (d) 250 °C, and (e) 300 °C. 44

Figure 3. 6 (a)-(c) shows the variation of transfer characteristics of annealed SnO-TFTs in ammonia (NH_3), forming gas (H_2), and air-annealing conditions. The corresponding device parameters are listed in **Table 3.4.**... 46

Figure 3. 7 The (a) transfer and (b-c) output characteristics of air-annealed SnO:H TFTs with different annealing temperature after ALD-Al_2O_3 BC layer formation at 80 °C.............. 48

Figure 3. 8 (a) Effective subgap DOSs extracted from the field-effect conductance analysis for *p*-channel pristine, back-channel surface etched, and ambipolar SnO-TFTs with ALD-Al_2O_3 passivation layer deposited at 250 and 300 °C. E_{QF} denotes a quasi-static Fermi level... 49

Figure 3. 9 (a) Normalized photoconductance decay spectra for the pristine SnO film (black), back-channel surface etched SnO film (blue), and ALD-Al_2O_3 passivated (red) SnO films at 300 °C. The inset shows the μ-PCD reflectivity signal spectra. (b) The illustration of proposed hole trapping/emitting process at shallow state for the slow decay................................. 51

Figure 3. 10 The observed and calculated photoconductance decay curves for (a) pristine, (b) surface-etched, and (c) ALD-Al_2O_3 passivated SnO films at 300°C............................... 52

Figure 3. 11 (a) Voltage transfer characteristic (VTC) of ambipolar SnO-TFT based CMOS-like inverters at the first (positive V_{DD} and positive V_{IN}) (right) and third quadrant (negative

V_{DD} and negative V_{IN}) (left). The insets indicate the schematic of CMOS-like inverter circuits. 54

Figure 3. 12 The voltage transfer characteristics (VTC) of the ambipolar SnO-TFT based CMOS-like inverters in the first quadrant. Blue solid line: ideal V_{INV} condition. Red solid line: *n*-channel operation V_{INV} (V_{OUT}=V_{IN}–$V_{TH,n}$). The V_{INV} are switching threshold voltage corresponding to V_{DD} from 30V to 50V (step +5V), respectively. 55

Figure 3. 13 The voltage gains for ambipolar SnO-TFT-based inverters for first and third quadrants (10 devices). The average voltage gains are 64.1±12.0 and 48.8±6.8 for the first and third quadrants, respectively. 58

Figure 4. 1 (a) The binding free energy of Guanine-rich *Ap* ($\Delta G_{bind, Ap}$), labeled (1), (2), (3), (4) and (5) – see *text,* may be correlated to the limit of detection (LoD), as indicated through the dashed line. We have obtained, through experiment, the *limit* indicated by the white cross, using the T30695 *Ap* optimally linked to the PBASE bound to the graphene surface. 63

Figure 4. 2 (a) Optical microscopy image of the GFET (scale bar: 100 µm) and the graphene channel on SiO2 substrate (inset). (b) The Raman spectroscopy of graphene/SiO2, the Raman peak intensity is normalized to that of the 2D peak intensity 65

Figure 4. 3 The graphene field effect transistor (GFET) fabrication processes[], include (a) electrode patterning and definition, by photolithography, (b) oxide (SiO2) deposition, (c) Transfer of graphene onto the oxide. 67

Figure 4. 4 (a) The physical interpretation of the non-faradic EIS circuit model. electrode resistance (R_e), electrolyte resistance (R_s), cable capacitance (C_c), Warburg diffusion impedance (W),

interfacial resistance (R_{int}) and electrical double layer capacitance (C_{EDL}) may be obtained, from the plot, as represented in the *inset* equivalent baseline circuit model. 69

Figure 4. 5 **(a)** The estimated C_{EDL} as a function of the PBASE concentration placed on the graphene surface of the FET. The top *inset* represents the corresponding EIS circuit model and the bottom *inset* indicates a schematic of the pyrene group of the PBASE attachment to the graphene. 71

Figure 4. 6 (a) Nyquist plot for the graphene FET immobilized with PBASE concentration of 10 mM, 100 μM, and 1 μM for 30 minutes. The *inset* shows a magnified view of the impedance spectra at high frequency. (b) The variation of the solution resistance: R_s, and the electrode resistance: R_e, with PBASE concentration. 72

Figure 4. 7 AFM imaging of graphene surface covered with 100 nM *Ap,* after **(a)** 8 minutes, **(b)** 30 minutes, and **(c)** 120 minutes. A schematic of the inferred coverage is indicated on the *left* of each image. In **(a)**, the h represents the PBASE unlinked graphene surface. The height profiles correspond to the line trace shown in the AFM images. 75

Figure 4. 8 AFM imaging (over a 5 μm x5 μm area) for the (a) 8 minutes *Ap* incubated graphene surface, and (b) corresponding image with height scale in the range of -2.50 nm to -4.00 nm, indicating the possibility of spaces, gaps, or holes on the surface – see **Figure 4.7**, on the surface. 76

Figure 4. 9 AFM imaging (over a 1 μm x1 μm area) for the (a) bare graphene, (b) PBASE attached graphene, and subsequently with the *Ap* incubated for (c) 8 minutes, (d) 30 minutes, and (e) 120 minutes. The corresponding height profile and RMS roughness are shown. 77

Figure 4. 10 (a) The variation of the I_{ds}-V_g characteristics as a function of the preparation of the GFET for Pb^{2+} detection, comparing (i) pristine graphene, with the characteristic after (ii) attachment of the PBASE linker onto the graphene: purple, followed by (iii) addition of the Ap (10 μM): blue, and then (iv) ethanolamine (EA) addition: green. 79

Figure 4. 11 (a) Measured C_T of the GFET as a function of the V_g, (b) The variation of the C_T (at V_g =0) under at AC frequency. The inset represents the deployed capacitance model. ... 80

Figure 4. 12 (a) The change in the V_D (ΔV_D) with [Pb^{2+}], as a function of the *Ap* incubation time. A Hills-Langmuir model (with parameters listed in the *inset*) incorporating the influence of the *Ap* incubation times, i.e., at 30 min: red, 2 h: yellow, and 4 h: blue, was used for modeling the associated *Ap* occupation and the binding kinetics. 83

Figure 4. 13 (a) The I_{ds}-V_g characteristics as a function of the added Pb^{2+} , *i.e.,* the [Pb^{2+}], in the range of 100 aM to 100 nM under a fixed *Ap* addition of 100 nM. (b) The change in the Dirac voltage: ΔV_D, as a function of the [Pb^{2+}] with various *Ap* additions, all incubated for 30 minutes; the measured data were fit to the Hill-Langmuir model 86

Figure 4. 14 The variation of DV_D, as a function of [Pb^{2+}] at various *Ap* incubation times, with the data fit to the Hill-Langmuir model (dashed line). 89

Figure 4. 15 (a) The ΔV_D measured from 100 nM of ions, *e.g.,* Ca^{2+}, Co^{2+}, Fe^{3+}, and Al^{3+}, that may confound the detection of the chosen Pb^{2+} analyte. The threshold ΔV_D ($\Delta V_{D,\ Thresh.}$) represents the lower ΔV_D limit of the GFET aptasensor that can distinctly identify the presence of Pb^{2+} 90

LIST OF TABLES

Table 2. 1 Comparison of the measured and simulated TFT parameters of SnO-TFTs. Hole density was obtained by the Hall-effect measurement of thin film samples. Acceptor density is a setting value for T-CAD simulation. 26

Table 3. 1 The TFT parameters of pristine and back-channel surface modified SnO-TFTs for *p*-channel mode shown in **Figure 3.3**. 40

Table 3. 2 The device parameter extracted from ALD passivated back-channel etched device shown in **Figure 3.4**. 43

Table 3. 3 *P*- and *n*-channel device parameters corresponding to transfer and output characteristics shown in **Figure 3.5** 45

Table 3. 4 The TFT parameters extracted from the devices shown in Figure 3.6 47

Table 3. 5 The photoconductance decay parameters extracted from Figure 3.10 52

Table 4. 1 The determined Limit of Detection (LoD) as a function of the Ap incubation time... 85

Table 4. 2 The estimated LoB (Limit of Blank) and LoD (Limit of Detection) as a function of added *Ap* concentration, with the *Ap* incubated for 30 minutes. 88

Table 4. 3 Calculated LoB and LoD as a function of the *Ap* incubation time, with *Ap* concentration of 100 nM. 89

ACKNOWLEDGEMENTS

I would like to express gratitude to my current and previous academic supervisor Dr. Prabhakar R. Bandaru, and Kenji Nomura, respectively, who provided the support and guidance through my research and career development. I appreciate that I joined their group and received the support and advice to grow as an independent researcher and a problem-solver. From Dr. Bandaru, I gained a lot of inspiration, motivation, and knowledge for my thesis research.

I would like to express gratitude to my family – my parents, Inseock Lee and Kilja Kim, and my older sister, Sora Lee. In 2007, my parents made a difficult decision to immigrate to the U.S. in their late 40's. With leaving their home county, they made countless sacrifices for my sister and me. Without their support, love, and prayers, I wouldn't be able to finish writing my thesis. My sister, Sora Lee, is the first Ph.D. holder in my family who graduated in Materials Science and Engineering from Penn State University. Her support and knowledge helped me throughout my Ph.D. study in Materials Science and Engineering. I am proud to have them as my family, whom I love and respect deeply. I also thank all my relatives, who support me with prayers and love.

Next, I want to thank my thesis dissertation committees: Dr. Shadi Dayeh, Dr. Tina Ng, and Dr. Yuan Taur for serving on my committee, and their advice, support, and encouragement throughout my research works.

I also want to thank all my group members. I want to thank the help from Dr. Yongliang Dong, and Shreyam Natani for the fabrication and characterization of the graphene field-effect transistor. I want to thank Dr. Hidenori Yamada for the valuable suggestions in the physical models of my research projects. In addition, I give thanks to Li Cheng, Kesong Wang, Pranjali Khajanji, Ramteja Kondakindi, Putian He, Kassra Eshraghi for all the help and support in the lab.

I would like to thank Dr. Deependra Kumar Ban for his collaboration in incorporating graphene field-effect transistors with biomolecular sensor development. I want to thank him for his time and valuable guidance in both experiments and paper preparations.

Last but not at least, I give all thanks and glory to God who came to my life and leads me as my Savior, Father, and Shepherd with his great love. With his everlasting love, I am able reach the milestone of graduating with a Ph.D.

The material in this dissertation is based on the following papers which are published or submitted.

Chapter 2, in full, is a reprint of the material as it appears in Lee, Alex; Le, Dong; Matsuzaki, Kosuke, and Nomura, Kenji, "Hydrogen-Defect Termination in SnO for p-channel TFTs." *ACS Appl. Electron. Mater.* 2020, 2 (4), 1162–1168. The dissertation author was the primary investigator and author of this paper.

Chapter 3, in full, is a reprint of the material as it appears in Lee, Alex; Zhang, Yong; Huang, Chi-Hsin; Matsuzaki, Kosuke, and Nomura, Kenji, "Switching Mechnism behind the Device Operation Mode in SnO-TFT." *Adv. Electron.* Mater. 2020, 5, 2000742. The dissertation author was the primary investigator and author of this paper.

Chapter 4, in full, has been submitted for publication of the material as it may appear in Dong, Yongliang; Lee, Alex; Ban, Deependra; Wang, Kesong; Bandaru, Prabhakar, "Femtomolar Level-Specific Detection of Lead Ions in Aqueous Environments, Using Aptamer-Derivatized Graphene Field-Effect Transistors." *ACS Appl. Nano Mater.* 2023, 6 (3), 2228–2235., and Lee, Alex; Dong, Yongliang; Natani, Shreyam, and Bandaru, Prabhakar, "Towards the Ultimate Limit of Analyte Detection in Graphene-based Transistors" *Nano letter* (under review). The dissertation author was the primary researcher and author of this paper.

VITA

2018 Bachelor of Science in Materials Science and Engineering,
Rutgers University, New Brunswick, NJ, United States

2019 Master of Science in Materials Science and Engineering,
University of California San Diego, La Jolla, CA, United States

2023 Doctor of Philosophy in Materials Science and Engineering,
University of California San Diego, La Jolla, CA, United States

ABSTRACT OF THE DISSERTATION

Developing oxide semiconductors and graphene field-effect transistors for next-generation electronic and electrochemical sensing

by

Alex Wootae Lee

Doctor of Philosophy in Materials Science and Engineering

University of California San Diego, 2023

Professor Prabhakar Bandaru, Chair

Since the recent development of Indium-Gallium-Zinc-Oxide (IGZO) thin-film transistor (TFT), oxide semiconductors have received considerable attention and are widely used as a TFT backplane for the state-of-art active-matrix flat panel display. However, the device application of oxide-TFTs is limited to unipolar devices due to the absence of high-performance *p*-channel oxide TFTs. This limitation poses a significant challenge in advancing oxide device technology, particularly in realizing complementary metal-oxide semiconductor (CMOS) inverter circuits.

Tin monoxide (SnO) emerges as a promising oxide semiconductor to develop high-performance *p*-channel oxide-TFTs due to relatively good hole mobility and low-temperature

processability below 300 °C. But their device performances are still largely behind *n*-channel oxide TFTs (e.g., IGZO, ZnO) because of high-density subgap defects (10^{20} cm^{-3}) originated from oxygen vacancy (V_o). By incorporating hydrogen annealing after pulse laser deposition (PLD), V_o induced hole traps in SnO were effectively reduced by forming Sn-H bonds, improving TFT mobility to ~1.8 cm^2/Vs and I_{on}/I_{off} ratio to ~10^5. In addition, the subgap defects were further suppressed by adding back-channel passivation layer, allowing SnO-TFTs to exhibit ambipolar behavior by alleviating the fermi-level pinning near valence band (VB) defects.

Lead (Pb^{2+}) exposure is a serious health concern that possesses detrimental effects on public health, causing irreversible damage to minors. Both conventional and home kit detection methods face limitations such as high cost or poor reliability and limit of detection (LoD). In addition to studies on oxide semiconductors, I will discuss the label-free graphene field-effect transistor (GFET) based aptamer sensor (aptasensor) specific to Pb^{2+} sensing. The surface of chemical vapor deposition (CVD) synthesized graphene is functionalized with Pb^{2+} specific aptamer (*Ap*), a single-stranded DNA oligonucleotide, serving as a receptor probe binding to linker molecules on graphene. The binding of the target Pb^{2+} to the *Ap* is transduced into the modulation of the electrical current through graphene FET. The theoretical LoD of GFET aptasensor is discussed based on thermodynamic prediction of probe – linker – channel surface binding energies. The surface density of *Ap* on graphene is optimized by monitoring minimization of capacitance via electrochemical impedance spectroscopy (EIS) to reach uniform *Ap* distribution, avoiding steric hinderance due to *Ap* clustering. The record sensor sensitivity was demonstrated with LoD of ~ 7.0 fM, reaching the LoD predicted from the theoretical thermodynamic prediction.

INTRODUCTION

1. Oxide semiconductor for device applications

Thin-film transistors (TFTs) are the type of field-effect transistor (FET) that utilize a variety of thin layers of semiconducting film, a dielectric layer, and metal contacts on the insulating substrate. Apart from the conventional metal-oxide-semiconductor FET (MOSFET) technology that utilize the bulk silicon for both semiconductor and substrate, TFTs technology have a variety choose for both semiconductor (*e.g.* metal oxides[1-3], and organic semiconductor[4-6]) and substrate (*e.g.* glass[7-9] ,and polymer[10-12]), unleashing the potential of transistor beyond the bulk silicon. The TFT fabrication technology has a similar duration of history almost match to the complementary metal oxide semiconductor (CMOS) technology, but it took several decades before achieving enough maturity to reach the actual production.[13] The commercial application of TFTs is primarily focused on display applications which utilize channel materials including amorphous hydrogenated silicon (a-Si:H), low-temperature polysilicon (LTPS), and Indium-gallium-zinc-oxide (a-IGZO).[14]

Oxide semiconductors for TFTs application particularly received much attention since the a-IGZO-TFT was published in back in 2004.[15] Compared to conventional channel material (*e.g.* a-Si:H for TFT-LCD) used for display application, oxide-TFTs can take an advantage in terms of optical transparency and low-cost of processing, and device stability and reliability.[16] In addition, the superior device performances such as high TFT mobility over 10 $cm^2V^{-1}s^{-1}$, low voltage operation, and low off-current characteristics make a-IGZO an ideal material to develop various high-performance active-matrix flat panel display (AMFPD) such as large-sized liquid crystal display (AMLCD), and organic light-emitting diode (AMOLED), flexible display, and micro-LED.[17-19] Beyond their usage in display applications, oxide-TFTs are continuously extending

their applications to the broader area, including low-power Internet of Thing (IoT) device, energy harvesting, and biomedical sensing technology.[20-26] However, the device application of oxide-TFTs is limited to unipolar devices due to the absence of high-performance *p*-channel oxide TFT, the critical drawback of current oxide device technology.[27-30] For display application, CMOS TFTs could greatly reduce the need for complex circuit compensation and external driving TFTs as well as significant power reduction for switching between ON and OFF states.[32] Since low-power enabled complementary metal-oxide-semiconductor (CMOS) technology, which consists of *n*- and *p*-channel transistor, is a critical component in current electronics, developing oxide-TFT based CMOS inverter circuit is the greatest challenge to move oxide device technology to next step.[32,33] The high-performance *p*-channel oxide semiconductor could also potentially help to further develop advanced display by offering more cost and process efficiency compared to state-of-arts low-temperature polysilicon oxide (LTPO) technology, typically formed by *n*-channel a-IGZO and *p*-channel LTPS, currently available to fabricate low power & high-resolution mobile display.

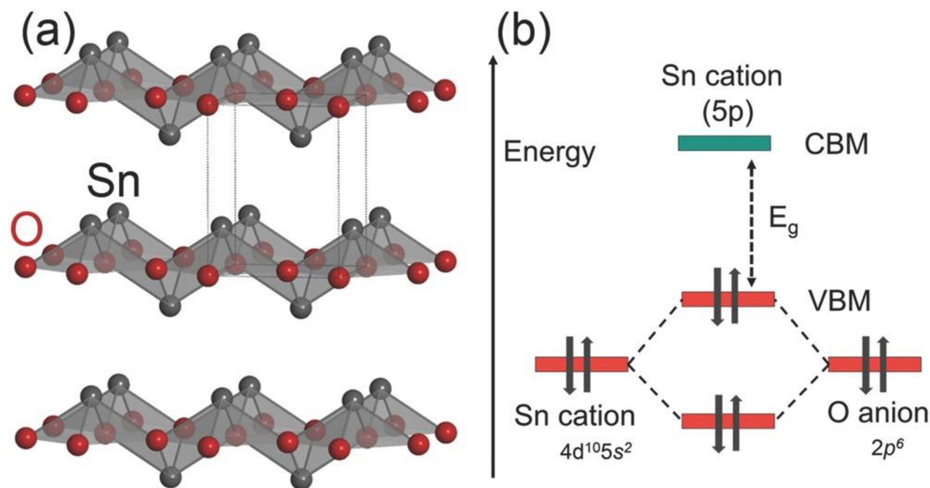

Figure 1. 1 (a) The SnO crystal structure, and (b) the schematic representation of the hybridization of valence band maximum (VBM) in SnO.[34]

Figure 1.1 a) The SnO crystal structure, and b) the schematic representation of the hybridization of valence band maximum (VBM) in SnO.[34]

So far, several *p*-type oxides have been discovered and studied to develop the high-performance *p*-channel oxide TFT such as Tin monoxide (SnO) and cuprous oxide (Cu_2O).[34] SnO is particularly the point of interest due to the high intrinsic mobility ~ 60 cm^2/Vs[35], which can be attributed to the low effective mass of holes due to its distinctive orbital arrangement (**Figure 1.1**). The valence band maximum (VBM) of SnO is formed by the hybridization of Sn 5s and O 2p orbital, mitigating the localized oxygen p orbital and creating better hole conduction path.[34,36] Also, the co-contribution of Sn 5s orbital to the VBM and Sn 5p orbitals to the conduction band minimum (CBM) makes SnO conducts both electron and hole, opening up new opportunities for oxide semiconductors in ambipolar applications.[34,37,38] However, although many efforts on SnO based oxide-TFT development have been devoted, their device performance are still largely behind as compare to other known *n*-channel oxide-TFTs (e.g. IGZO and ZnO) due to the high-density subgap defect over 10^{20} cm^{-3}.[33,39] Therefore, the reduction of subgap defect is a key for realizing high-performance *p*-channel oxide-TFTs.

In our work, we present a hydrogen subgap defect termination for developing *p*-type and ambipolar oxide SnO. Hydrogen is strongly believed as an electron donor for most *n*-type oxides such as ZnO and a-IGZO which causes severe device degradation in *n*-channel oxide TFTs because of the generation of excess electron carrier.[40] However, we found that hydrogen could effectively terminate the subgap hole traps, which is originated from oxygen vacancy in SnO by forming Sn−H bonds. By incorporating hydrogen annealing after pulse laser deposition (PLD), V_o induced hole traps in SnO were effectively reduced by forming Sn-H bonds, improving TFT mobility to ~1.8 cm^2/Vs and I_{on}/I_{off} ratio to ~10^5. The origin of subgap defect and the role of hydrogen in SnO

were discussed based on the computational device and material simulation. In addition, the subgap defects were further suppressed by adding atomic layer deposition (ALD) back-channel passivation layer, allowing SnO-TFTs to exhibit ambipolar behavior with *p*-channel mobility of 1.2 cm^2/Vs, and *n*-channel mobility of 0.03 cm^2/Vs by alleviating the fermi-level pinning near valence band (VB) defects.

2. Graphene field-effect transistor (FET) for sensing applications

Lead exposure is a rising health concern that could possess the detrimental effects to public health.[41-43] The recent outbreaks from city of Flint, Michigan and Newark, New Jersey, USA revealed that the majority of population in a modern city can be highly vulnerable and easily affected to lead contamination.[44-47] The consequence of direct intake of lead could be particularly critical to underaged minors. The lead contamination higher than 15 ppb (~72 nM) in drinking water and blood lead level higher than 100 μg/L (0.48 μM) would leading to damage in brain and nervous system, slowed growth and development, and hearing and speech problem.[48,49] The conventional methods such as inductively coupled plasma mass spectrometry (ICP-MS), atomic emission spectrometry (AES), and atomic absorption spectroscopy (AAS) are proven to be accurate and widely accepted but involved with labor-intensive sample collection and preparation, time-consuming process, and costly instrument.[43,50-52] In comparison, commercially available at-home kits detection method can take advantage of low-cost and accessibility, but their reliability, specificity and detection range are uncertain, typically ~10 mg/L (~48 μM).[41] Hence, the development of the new biosensor is necessary.

Over the past decade, field-effect transistors (FET) biosensor has considered as a highly promising candidate for next-generation biosensor due to their high sensitivity, rapid detection and the ease of integration into the electronic manufacturing process.[53-55] A biosensor based on FET

comprises various functional components, as depicted in **Figure 1.2**, to generate and detect analyte-specific signals. Key elements include the recognition element (such as antibodies, single-stranded DNA, or ion-sensing membranes) and the transducer. The recognition element facilitates binding with target probes, generating a signal indicative of the analyte's presence and concentration. In biosensors, the recognition element is typically attached to the transducer's solid surface layer through immobilization. The transducer, in turn, is responsible for converting quantitative or semi-quantitative information about the target into a measurable signal, such as current, potential, or temperature change. Recent developments in FET based sensors have been mostly focused on low-dimensional materials incorporating two-dimensional (2-D) and 1-D structures due to their high surface-to-volume ratio and high charge carrier mobility[56-58], leading to superior sensitivity as in the instance of single atom sheet constituted Graphene FET (GFET).[59-61]

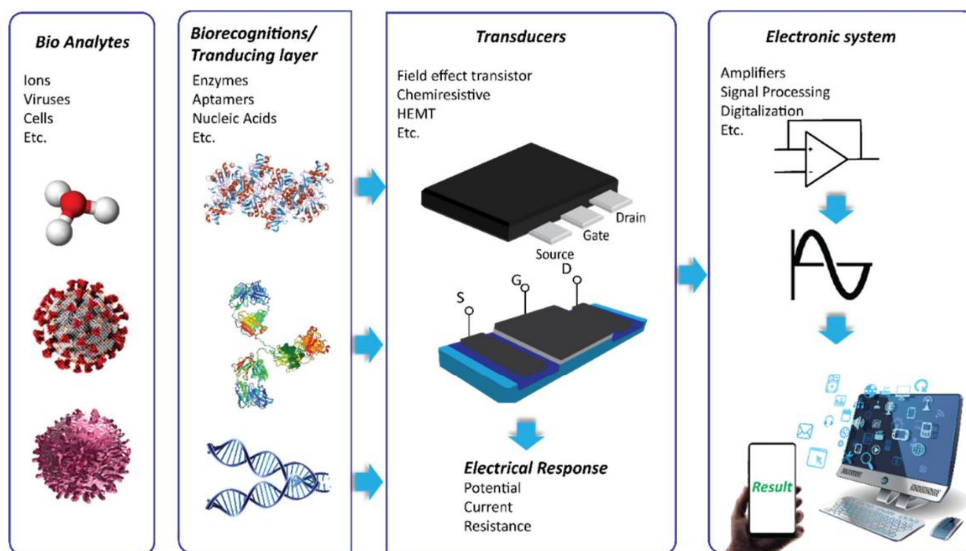

Figure 1. 2 The scheme illustrates a chemical and biosensor configuration consisting of a recognition element (receptor) attached to the transducer to selectively detect the analyte of the interest.[62] The transducer converts the biorecognition event on its surface into a quantifiable signal before transmitting it for further processing. This processed signal can then be interpreted by the end user.

Typically, the surfaces of GFET sensors have attached linker molecules (*e.g.,* 1-pyrenebutanoic acid *N*-hydroxysuccinimidyl ester: PBASE) and bioreceptors, such as aptamers (*Ap*), antibodies, and enzymes for specific binding to the target analyte.[63-65] With respect to *Ap*, single-stranded DNA or RNA oligonucleotides, are particularly attractive due to the enhanced stability, high selectivity, and ease of further modification (/adaptation) from (/to) various functional groups.[66-68] By utilizing PBASE and *Ap* as a linker and receptor probe, we presented the graphene FET based *Ap* sensors (aptasensor) for Pb^{2+} specific detection. Top electrolyte gating scheme was used for the improved efficiency.[69–72] The graphene layer in the GFET was functionalized with specific *Ap* receptor probes.[73–76] The binding of the target Pb^{2+} to the *Ap* is transduced into modulations of the electrical current through the GFET.

The estimation of the limit of detection (LOD) for our fabricated GFET aptasensor by analyzing it from a thermodynamic standpoint. This assessment involves considering the Gibbs binding energy (ΔG) related to the total binding energies of *Ap*-linker-channel surfaces, leading to expected LoD to the level of ~10 fM. Therefore, achieving such a LoD level is feasible through proper optimization of experimental protocols and procedures. Practical optimization involves monitoring the sequential adhesion process: (i) PBASE onto graphene, (ii) *Ap* onto PBASE, and finally (iii) the analyte, such as Pb^{2+}, onto *Ap*. The effective approach for achieving this optimization is through charge monitoring, specifically focusing on electrical capacitance. At the individual FET device level, electrochemical impedance spectroscopy (EIS) can be employed for this purpose. For instance, differences in electrical double layer capacitance (C_{EDL}) can be anticipated when measured on a pristine graphene surface as compared to a surface modified with linkers and *Ap*.

We demonstrate how optimization of sensing protocols yields ultrasensitive lead ion concentration: [Pb^{2+}], specific detection, at the single femtomolar (fM) level significantly improving, by orders of magnitude, extant reported values.[73−77] Furthermore, the specificity was substantially enhanced to the fM level. Comparing to earlier GFET related work, it was indicated that the use of 8−17 nucleotide (NT) DNAzyme[75,76] (with dsDNA) for Pb^{2+} detection enabled through the cleavage of one strand in the presence of Pb^{2+}, yielded an LoD of ~0.2[75] and ~0.02 nM[76] with gold (Au) nanoparticle decorated GFET, with specificity at 0.5[72] and 0.1 nM[73], respectively. While DNAzymes show strong Pb^{2+} affinity, their large size and related structural rigidity[78] make lower LoD difficult. In other studies,[67,68] a guanine (G)- enriched *Ap* placed on the graphene surface was reported to have an LoD of 2 μM[68] with a SiO_2 back-gated GFET and an LoD of ~0.8 nM[67] of Pb^{2+} on an HfO_2-gated GFET, with specificity ~48 nM.[67]

In comparison to those of previously reported studies on Pb^{2+} detection, we show that the LoD and the specificity for [Pb^{2+}] detection may be improved significantly by order of magnitude. We adapted a G-quadruplex structured *Ap*-based modality for label-free Pb^{2+} detection, yielding LoD as low as ∼ 7 fM and specific determination of [Pb^{2+}] at 100 fM. The LoD was found to be critically dependent on the *Ap* concentration and incubation time, which regulates the amount of immobilized *Ap* on the graphene surface. An optimal sensing protocol was determined through extensive experimentation, *e.g.* atomic force measurement (AFM). Overall, it was found out that the sensitivity can be related to 1) the doping-induced carrier density (n_0) and carrier mobility (μ) of the graphene arising from an *Ap*−Pb^{2+}−Gquadruplex (APG) formation, and 2) the optimized *Ap* distribution on graphene surface to avoid the steric hinderance, e.g. *Ap* clustering that trigger the reduction of the binding affinity.

Chapter 2. Hydrogen-Defect Termination in SnO for p-Channel TFTs

2.1 Introduction

Developing high-performance oxide thin-film transistor (TFT) has been a subject of interest because of ever-increasing demands for next-generation flexible electronic devices.[79–81] *n*-type oxide semiconductors such as amorphous Indium-Zinc-Gallium-Oxide (a-IGZO) are intensively studied for channel material for TFT and achieved excellent device performances, including high TFT mobility (≈10 $cm^2 V^{-1} s^{-1}$), low operation voltage (~3 V), and low off-current characteristics as well as excellent mechanical flexibility and low-cost processability.[82] Therefore, *n*-channel a-IGZO-TFT is successfully commercialized in the market and widely used as a TFT backplane in the state-of-art active-matrix flat panel display such as large-sized high-resolution organic light-emitting diode and low-power consumption active-matrix liquid crystal display.[83–85] The next major challenge faced in oxide semiconductor technology is to develop complementary metal-oxide semiconductor (CMOS) inverter circuits for future ubiquitous device applications. So far, several CMOS inverters based on oxide-TFTs have been demonstrated with *n*-type oxide a-IGZO and *p*-type oxides such as SnO, Cu_2O, and organic semiconductors.[86–88] However, different fabrication process involved in *n*- and *p*-type materials results in complicated circuit design and integration, leading to the production of the impractical circuit.[90]

The difficulty of developing high-performance *p*-channel oxide TFTs mainly attributes to the nature of valence band maximum (VBM) of metal oxide, which consists of the localized oxygen 2p orbitals with a strong directivity.[86] Therefore, the hole carrier transport is easily degraded by the structural defects and impurities. In order to address this issue, a major breakthrough is essential at the stage of material development. SnO is a promising oxide semiconductor to develop *p*-channel oxide TFTs because of its attractive properties such as

relatively high hole mobility (≈2 $cm^2 V^{-1} s^{-1}$) and low temperature processability below 300 °C.[30,90] So far, several attempts to reduce subgap defects in SnO, such as the film growth optimization, formation of the passivation layer, and post-thermal annealing, have been proposed to improve the device performances.[91-94] Post-thermal annealing is the most simple and prevalent technique to improve the film quality and is widely used in a-IGZO based oxide-TFT technology.[95] However, the conventional thermal-annealing with uncontrolled atmosphere is limited for these *p*-type materials because the metal cation Sn^{2+} in SnO has more stable higher oxidation states such as Sn^{4+}, leading to formation of undesirable high oxidation states.[96] The formation of these high oxidation state results the severe degradation of the device performances. Therefore, it is imperative to develop effective defect termination techniques for *p*-type oxides to improve the device performance.

In this chapter, the hydrogen defect termination of SnO is introduced for developing high performance *p*-channel TFT and high gain CMOS like inverter circuit. Ch. 2.2 will introduce the experimental methods used to 1) deposit and anneal SnO film, 2) fabricate the TFTs, and 3) measure the electrical characteristic of the devices. Ch. 2.3 shows the material characterization to identify the material properties of unannealed and annealed SnO film. Ch. 2.4 demonstrates the electrical characteristic of the device with extracted device parameters. Ch. 2.5. exhibits the results of computational devices and material simulations that were used to investigate the origins of subgap defects and the impact of hydrogen in SnO.

2.2 Experimental Methods

2.2.1 Thin film deposition and device fabrication

Thin Film and Device Fabrication. SnO thin films were deposited at RT by pulse laser deposition (PLD) with a KrF excimer laser (wavelength 248 nm, pulse frequency 10 Hz). A polycrystalline SnO-sintered body was used as a target of PLD. The oxygen partial pressure (PO_2) during the deposition was optimized and fixed at 2×10^{-4} Pa. The laser energy density was set to ~1.5 J cm^{-2}. Silica glass substrates were used for fundamental material characterization of SnO films, and n+-Si substrates with SiO_2 with 100 nm were used for TFT fabrication. The SnO films are subjected to the post-thermal annealing for an hour in pure NH_3 gas or forming gas (H concentrating ~4.9%). Bottom-gate and top-contact, inverse-staggered, TFT structures were fabricated by standard photolithography with chemical wet etching. The SnO island structure was patterned by etching with 1 M of HCl. Indium tin oxide (ITO, Sn doping concentration of 10% with respect to Indium) was used for the source and drain electrodes. The channel width (W) and length (L) were 300 and 50 μm, respectively, with the W/L ratio of 6.

2.2.2 Thin Film and device Characterization

Film structures were examined by glancing angle X-ray diffraction (GIXRD) (Cu α radiation at an acceleration voltage of 50 kV, emission current of 50 mA, and an incident angle of 0.5°). Film thickness and film density were evaluated by grazing-incidence X-ray reflectivity (GIXRR) measurements. Optical transmittance and reflectance spectra were measured using a UV−vis spectrophotometer to extract the net absorption spectra of the films. Carrier concentrations and Hall mobilities were estimated from Hall measurements with an AC magnetic field modulation using the van der Pauw configuration. X-ray Photoemission spectroscopy (XPS) measurements were carried out with Al Kα (hν = 1486.6 eV) at RT. The films were transferred into the XPS apparatus without an extra surface cleaning, and the binding energy was corrected by the C 1s core

levels. The surface morphology was observed by atomic force measurement (AFM). TFT characteristics were measured by a semiconductor parameter analyzer at RT in the air in the dark and analyzed by a TFT device simulator ATLAS to extract the subgap DOSs of SnO active channels. The constant mobility model and crystalline subgap DOSs were employed. The first-principle calculation based on the density functional theory with gradient generalized approximation Perdew−Burke−Ernzerhof was performed by using the Vienna Ab initio Simulation Package (VASP) to clarify the origin of hole trap and the effect of hydrogen annealing for SnO TFTs. A 108-atom supercell (3 × 3 × 3 unit cells) was used for the defect calculations. The planewave cutoff energy and Monkhorst−Pack special k points were 400 eV, and 2 × 2 × 2, respectively. The formation energies (Ef) of defects for Sn-rich limits are determined by $E_f[defect^q] = E_{tot}[defect^q] - E_{tot}[perfect] + \sum_i n_i \mu_i + q(\epsilon_F + EVBM)$, where $E_{tot}[perfect]$ and $E_{tot}[defect^q]$ are the total energy of supercell containing the defects in a charged state q. ni and μ_i are the number removed from or to add to the reservoir, and i is the chemical potential of atoms, respectively.

2.3 Material Characterization of hydrogen defect terminated SnO

2.3.1 Microstructure of polycrystalline SnO films

Figure 2.1 shows glancing angle X-ray diffraction (GIXRD) patterns of the unannealed and annealed SnO films at different temperatures. The film thickness is 10.5 nm for the unannealed films. Only two haloes are observed around ~22 and 29° from the glass substrate and SnO layer, respectively, for the unannealed film. The lack of a sharp diffraction peak corresponding to the crystalline phase, i.e., PbO-type SnO, indicates that the film is amorphous. A series of diffraction peaks arising from SnO crystals is clearly seen from the films annealed over 280 °C, and no

impurity phases including SnO_2 and Sn metal are detected. All the annealed films are poly-crystalline without preferred crystal orientation. As the annealing temperature raises over 390 °C, we confirmed that the small peaks attributed to β-Tin started appearing at round $2\theta \sim 31^{o}$. Sharp diffraction peaks of β -Tin were observed from the film annealed at 450 °C, indicating that SnO was converted to Tin metal.

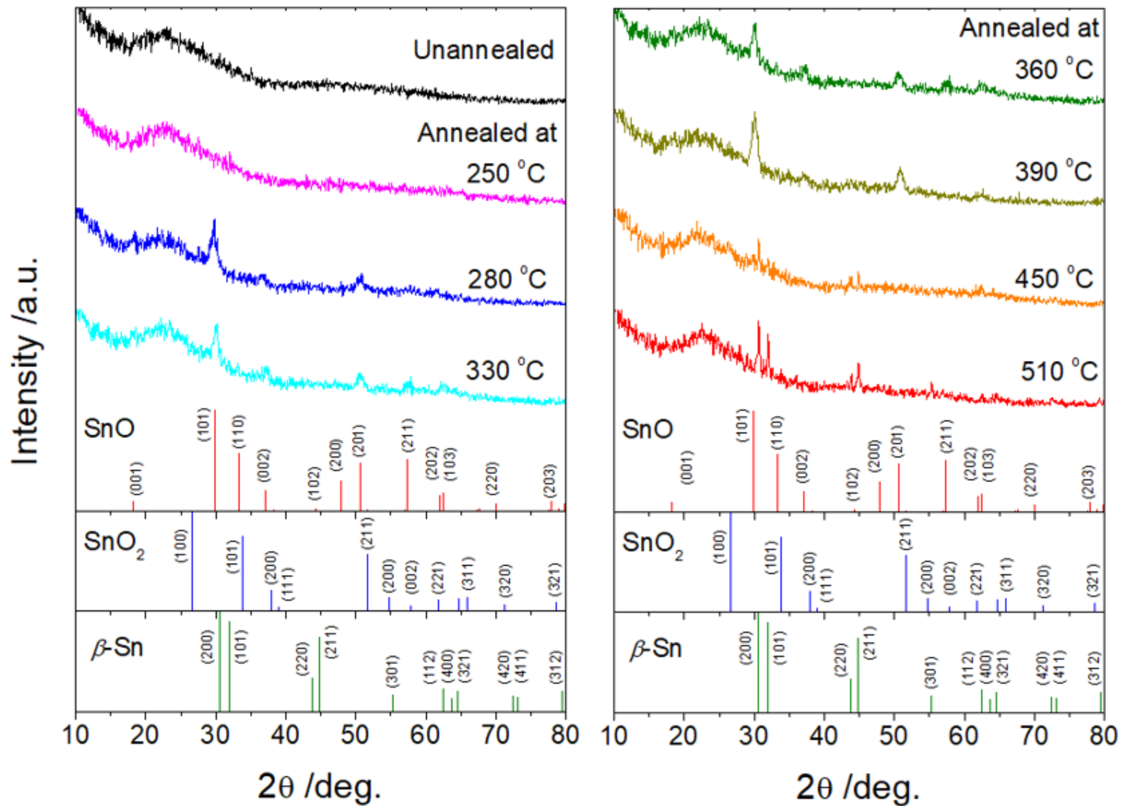

Figure 2. 1 The structure of 10.5 nm SnO films deposited on silica glass substrates. Glancing angle X-ray diffraction patterns of unannealed and annealed SnO film at 250 – 510 °C.

2.3.2 Film parameters (e.g. film density, thickness, and surface roughness) for polycrystalline SnO films

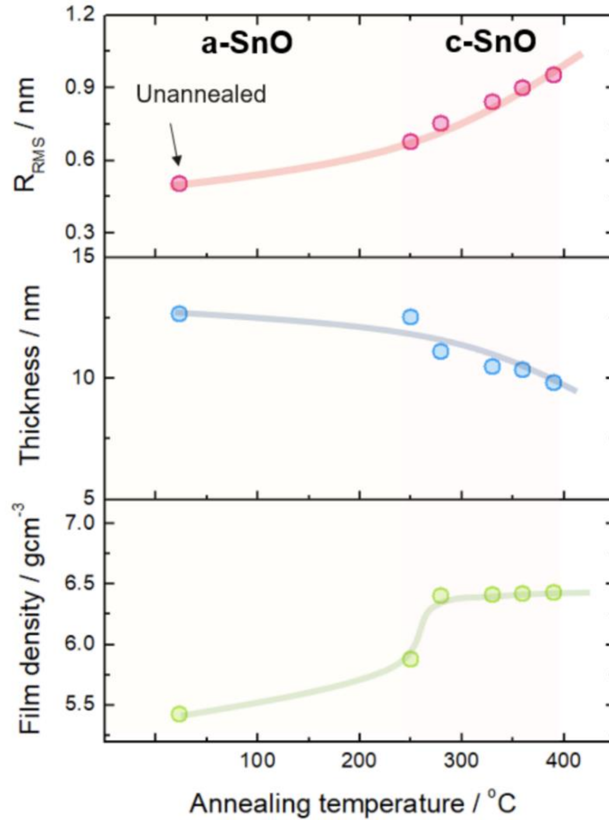

Figure 2. 2 Film parameters extracted from Glancing angle X-ray reflectivity patterns of a unannealed SnO film, and annealed SnO film at 250 °C, 280 °C, 330 °C, 360 °C, and 390 °C. (Top) The surface roughness, (middle) film thickness, (bottom) film density are illustrated.

Figure 2.2 shows the film parameters extracted from the measured and simulated glancing angle X-ray reflectivity (GIXRR) spectra for unannealed and annealed SnO films. All the XRR spectra are well-reproduced by simulations using simple one-layer film/glass model and provided accurate film thickness, film density and surface roughness. The film density of unannealed amorphous film is ~ 5.42 g cm^{-3}, about ~15.3% lower than that of the reported crystalline-SnO (~6.39 g cm^{-3}). The films become denser by thermal annealing, and the film density of crystalline SnO films annealed over 280 °C reaches the ideal film density of SnO with 6.39 g cm^{-3}. The film

roughness is likely to become rougher due to the poly-crystal grain formation, but the surface still maintains an atomically flat surface with RRMS ~1nm for the poly-SnO films.

2.3.3 Optical absorption spectra of polycrystalline SnO films

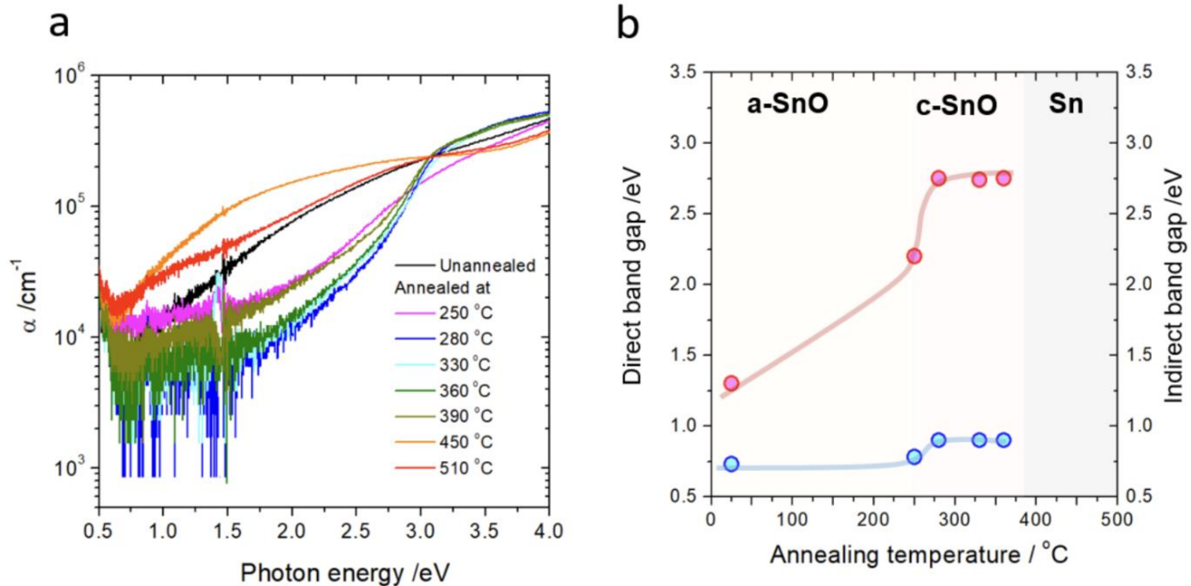

Figure 2. 3 (a) Optical absorption spectra of unannealed and annealed (250-510 °C) 10.5 nm SnO films. (b) The variation of direct and indirect bandgap of unannealed and annealed SnO films as a function of annealing temperatures.

Figure 2.3 shows the corresponding optical absorption spectra of unannealed and annealed SnO films with a thickness of ~10.5 nm. Intense and broad absorption over 105 cm^{-1} appears in the optical absorption spectrum of the unannealed film, indicating that the unannealed films involved very high-density subgap defect (~10^{20} cm^{-3}). Such a high-density subgap defect can cause no TFT operation because of the Fermi level pinning and the reduction of effective electrical field induced by a gate bias.[97] For the films annealed at 280-360 °C, the strong absorption is visible at >3 eV and weak absorption below the absorption edge, which corresponds to direct and indirect transition, are observed. **Figure 2.3(b)** plots the direct and indirect bandgap, which are

estimated from the plots of (αhν) 2 vs. hν and (αhν) 1/2 vs. hν, for unannealed and annealed SnO films. Prior to the post-thermal annealing, amorphous unannealed SnO film exhibits direct band gap of ~ 1.3 eV, half of reported bandgap SnO. After NH_3 annealing over 280 °C, the c-SnO films exhibit the direct bandgap with 2.7 eV and indirect bandgap of 0.8 eV, respectively, which are in good agreement to the reported data.[29]

2.3.4 Film surface structure of polycrystalline SnO films

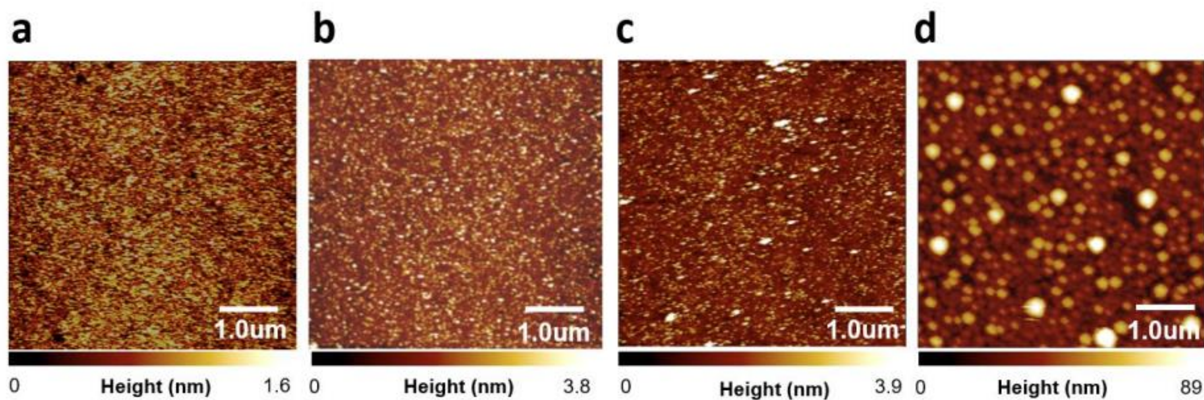

Figure 2. 4 AFM images of (a) unannealed and hydrogen-annealed films at (b) 250 °C, (c) 360 °C, and (d) 510 °C in pure NH_3

Figure. 2.4 shows the atomic force microscopy (AFM) images for unannealed and hydrogen annealed films at several annealing temperatures. Atomically flat and featureless surface structure with RRMS ~1.2 nm is observed in the unannealed film (**Figure 2.4(a)**). The annealed films (**Figure. 2.4 (b) and (c)**) show polycrystalline grain structure composed of nano-crystalline SnO with the grain size of ~10-15 nm. On the other hand, the high-temperature annealed film at 510 °C exhibits a very large grain structure (grain size of ~50-150 nm), which can be attributed to Sn metal peak observed from XRD result of **Figure 2.1**.

2.3.5 XPS analysis of polycrystalline SnO films

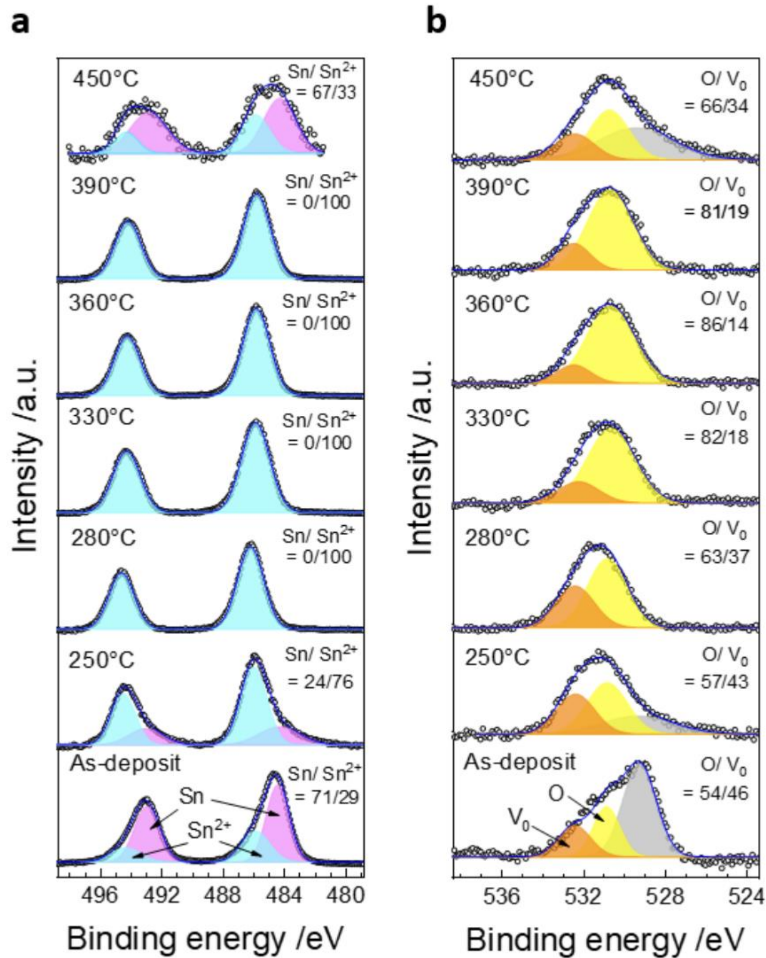

Figure 2. 5 (a) Sn 3d 5/2 and 3d 3/2 and (b) O1s core level spectra for unannealed film and annealed films at 250-450 °C in NH_3.

Figure 2.5 shows a) the Sn 3d (Sn 3d 5/2 and 3d 3/2) and b) the O1s core level spectra for the unannealed film and annealed films at 250-450 °C in NH_3. (Sn 3d core level) For the unannealed film and the annealed film at 250 °C, two valence states attributed to Sn (0) metal state at the binding energy (B.E.) of 484.5 and 492.9 eV and Sn(II) state at B.E. 486.0 and 494.4 eV for Sn 3d $_{5/2}$ and $_{3/2}$, respectively, indicating that these films are clearly composed of the mixed-phase of Sn and SnO. The Sn/SnO ratio is also shown in the figure as similar to other reported work.[95] On the other hand, the Sn 3d core spectra exhibit only Sn (II) oxidation state when the films are

annealed at 280-390 ^{o}C, indicating that the films are a single phase of SnO. The Sn metal starts to appear again by high temperature annealing over 450 ^{o}C (O 1s core level) The O 1s core spectra for all the films show the additional peak assigned to oxygen vacancy (V_o) at the B.E. 532.2 eV together with O-Sn bonding states at B.E. 530.8 eV.[98] For the unannealed film and annealed film at 250 ^{o} C, the O 1s core are differentiated into three chemical states including O-Sn and V_o states. The V_o is gradually reduced with the increase of annealing temperatures and saturated with the O/V_o ratio of ~80/20 at 330 ^{o}C.

2.3.6 Dependency of annealing temperature to Hole density of SnO films and bulk channel defect density in SnO-TFTs

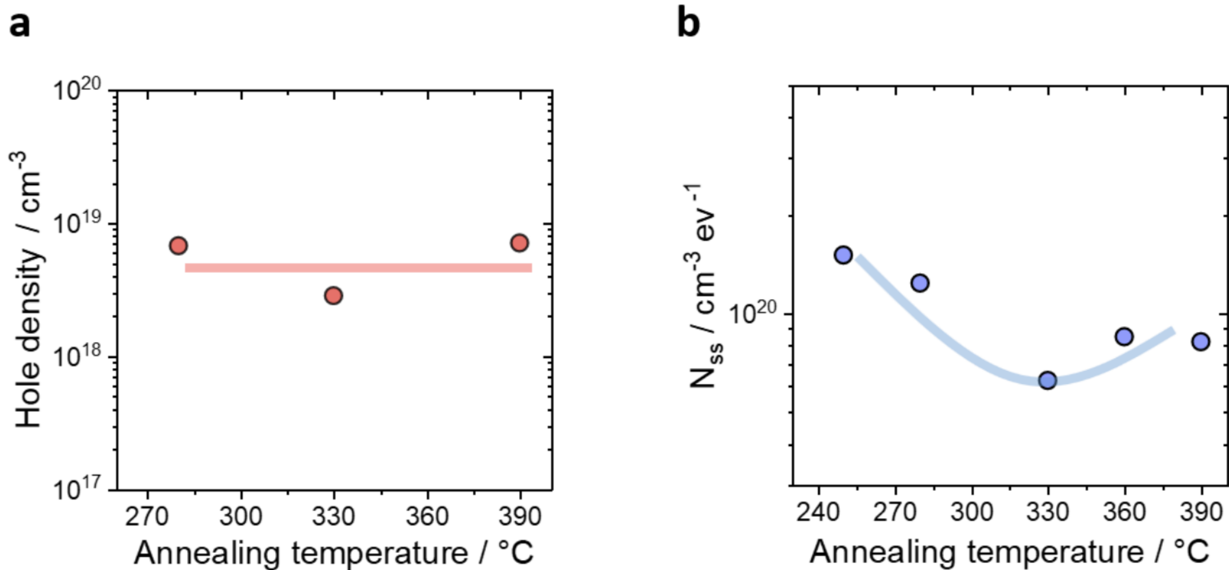

Figure 2. 6 (a) Hole density of SnO films measured by Hall-effect at room temperature. (b) Bulk SnO channel defect density extracted from the channel thickness dependency of s-values of SnO-TFTs.

Figure 2.6 (a) and **(b)** shows the variation of the Hole density of SnO films and the bulk channel defect density (N_{ss}) of SnO-TFT with different annealing temperature. Hole density of SnO films determined by Hall-effect measurement at room temperature. SnO bulk channel defect density was extracted from the channel thickness dependency of *s*-values of SnO-TFTs. The hole

density is remained almost unchanged while the N_{ss} is affected by the annealing temperature. The clear reduction of N_{ss} is observed from annealing temperature over 300 ºC.

2.3.7 RBS and HFS analysis for atomic concentration for unannealed and annealed SnO films

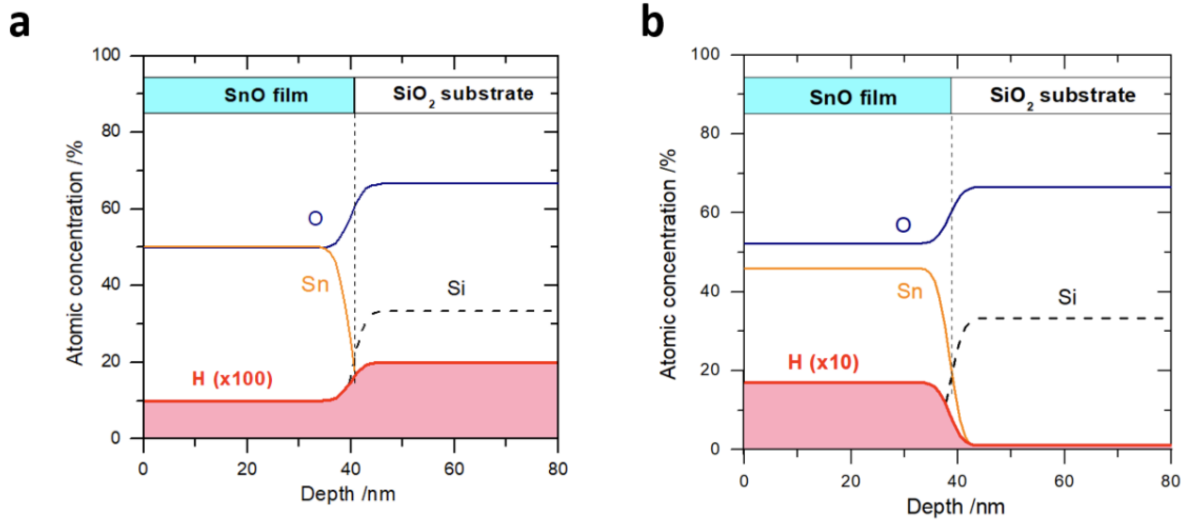

Figure 2. 7 (a) Hole density of SnO films measured by Hall-effect at room temperature. (b) Bulk SnO channel defect density extracted from the channel thickness dependency of s-values of SnO-TFTs.

Figure 2.7 shows the chemical composition and hydrogen depth profiles for unannealed, and hydrogen annealed films measured by Rutherford backscattering spectrometry (RBS) and Hydrogen forward scattering (HFS). The RBS/HFS analysis reveals a relatively high hydrogen concentration with ~5×10^{19} cm^{-3} exists even in the unannealed films. On the other hand, the hydrogen annealing apparently promotes the hydrogen concentration to ~9×10^{20} cm^{-3}, which corresponds to ~2% in SnO.

2.4 Electrical characterization of hydrogen defect terminated SnO-TFTs

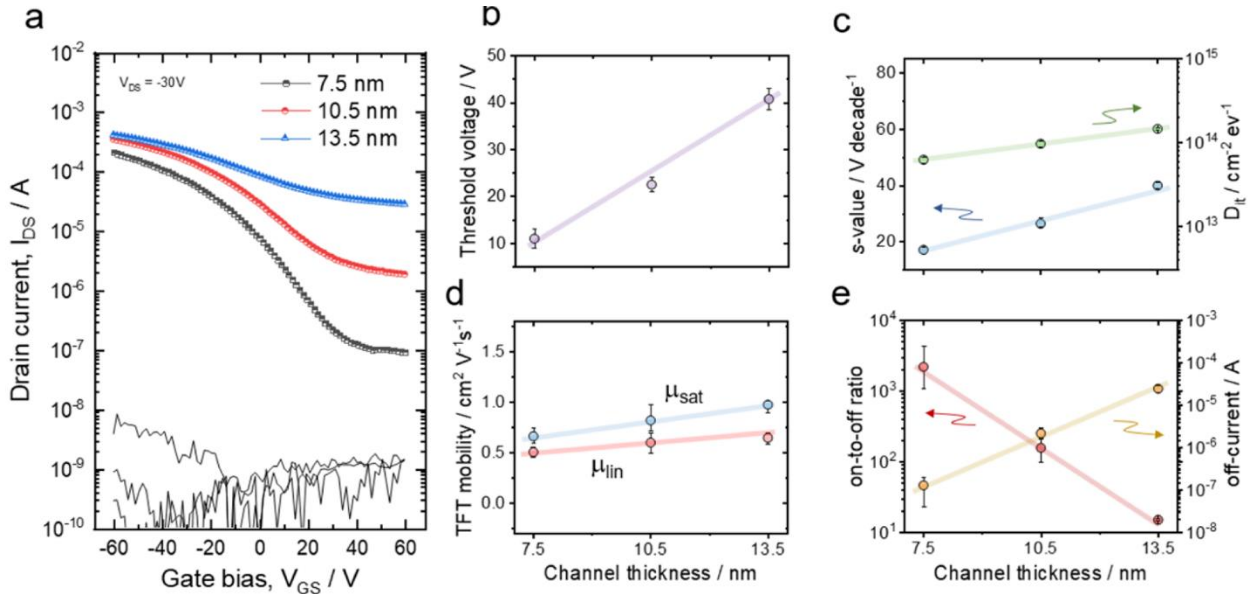

Figure 2. 8 (a) Variation of transfer characteristics for SnO TFTs with different channel thicknesses of 7.5, 10.5, and 13.5 nm after NH_3 annealing at 280 °C. TFT parameters are as following: (b) V_{TH}, (c) s-value and D_{it}, (d) saturation and linear mobility, and (e) on-to-off current ratio and off current at V_{GS} = 60 V.

Thin films of SnO were deposited on thermally oxidized SiO_2/ n+-c-Si substrates, which are used as a gate oxide/gate in the TFT device, with a deposition rate of ~3 Å/s by pulsed laser deposition (PLD) at room temperature (RT). The deposited films were subsequently annealed at 280 °C in a pure NH_3 atmosphere. An inverted staggered TFT structure with the channel length and width (W/L) of 300/50 μm (the W/L ratio is 6) was fabricated with 30 nm thick ITO source/drain electrodes. **Figure 2.8 (a)** shows the variation of the transfer characteristics, that is, source-to-drain (I_{DS}) versus gate-to-source (V_{GS}) curves, of SnO TFTs with the channel thickness of 7.5, 10.5, and 13.5 nm. The 10.5 nm thick SnO thin films are examined by glancing angle X-ray diffraction (GIXRD) and found as a polycrystalline with a nanocrystalline [the grain size of ~11−16 nm from atomic force microscopy (AFM) observation (see **Figure 2.1** and **2.4**)]. The

drain currents, marked as a source-to-drain voltage (V_{DS}), are increased at a negative V_{GS}, and all the devices are clearly operated in *p*-channel mode. The transfer characteristics are strongly dependent on the SnO channel thickness, and particularly, the off-current is largely altered. The TFT with a 13.5 nm thick SnO channel exhibits a very high off-current level of ~0.03 mA with an exceptionally small on-to-off current ratio with ~10. However, when the film thickness lowers down to 7.5 nm, the off-current is significantly suppressed as low as ~10^{-7} A. Meanwhile, the on-current is only slightly reduced by decreasing the channel thickness and is not significantly degraded even in the device with the thinnest channel thickness.

The important TFT parameters (i.e., threshold voltage (V_{TH}), saturation (μ_{sat}) and linear mobility (μ_{lin}), subthreshold voltage slope (*s*-values), on-to-off ratio, and off-current) are plotted as a function of the channel thickness in Figure 2.8 (b)−(e). The V_{TH}, which is determined by extrapolating a straight line in a (I_{DS})1/2−V_{GS} plot to the V_{GS} axis, decreased from +40 to +10 V as the channel thickness reduced from 13.5 to 7.5 nm, showing a strong correlation to the change of channel thickness (**Figure 2.8 (b)**). In general, the V_{TH} is altered by the acceptor density and the charged defects in the channel region and/or at the channel/interface. However, the observed monotonic variations of V_{th} are mainly because of the reduction of bulk defect originated from the decreases of the channel thickness because the acceptor density of SnO film is not affected by the film thickness.[86] The μ_{lin} and μ_{sat}, which were extracted from the following relation: I_{DS} = W·μ_{lin}·C_{OX}/L(V_{GS} – V_{TH})V_{DS} − 1/2V_{DS}^2 and I_{DS} = W·μ_{sat}·C_{OX}/L(1/2(V_{GS} – V_{TH})^2) (C_{OX} is the gate insulator capacitance per unit area), are 0.7−1.0 cm^2 V^{-1} s^{-1} for TFT with 13.5 nm thick SnO (**Figure 2.8 (c)**). The TFT mobilities are slightly degraded in TFTs with a thinner channel but still maintained 0.5−0.7 cm^2 V^{-1} s^{-1}. This trend is often observed in polycrystalline semiconductor films, which can be attributed to the changes in the microstructure of the film.[91] The obtained

TFT mobilities are nearly comparable to our measured hole mobility (μ_h) of 1.2 cm^2 V^{-1} s^{-1} at the hole density (N_h) of 6.7×10^{18} cm^{-3}.

On the other hand, the *s*-values are improved from 38 to 17 V/decade as the channel thickness decreases, indicating that the trap state density in channel is reduced in thinner channel TFTs (**Figure 2.8 (d)**). Trap state density is estimated from the *s*-values of the TFTs using the following relation: $S = \log_e 10 \cdot k_B T/e \cdot [1 + e(D_{it} + tN_{sg})/C_{ox}]$, where e is the elementary electric charge, k_B is the Boltzmann constant, and T is the temperature. The D_{it} and N_{sg} are the trap density around the Fermi level (EF) at the channel/gate insulator interface and in the channel bulk region, respectively. From the linear dependence of s-value on the channel thickness, the D_{it} and N_{sg} are estimated as $D_{it} = 6.2 \times 10^{13}$ cm^{-2} eV^{-1} and $N_{ss} = 1.4 \times 10^{20}$ cm^{-3} eV^{-1}, indicating that high-density hole trap defects are still involved in the SnO channel annealed at 280 °C.

Because the hole density of SnO channel is very high and above 10^{18} cm^{-3}, the strong channel thickness dependency of SnO TFTs can be understood by considering the channel depletion model in TFT operation, in which holes in the SnO channel are depleted by positive gate bias for the p-channel. The estimated width of the depletion layer for our SnO TFT device is ~15−20 nm, which corresponds to a maximum channel thickness that can control the carrier depletion. The estimated maximum channel thickness is well consistent with our observations where clear field-effect modulation is observed in the channel thickness less than ~20 nm. We also fabricated the TFT with very thick channel above ~40 nm and confirmed that the device showed very weak field-effect current modulation. Therefore, the channel thickness is a primary factor to improve the TFT characteristics in the current status of SnO TFTs because it is very challenging to control the hole density of SnO layer at the present condition. Although the channel layer with a thickness of less than 7.5 nm still maintains the continuous film structure, the

conductivity of film rapidly dropped, and the device exhibited a large degradation (more details can be seen in **Figure 2.10**). The understanding of the observed phenomena requires furthermore investigation, but we speculate that (1) increase of surface depletion effect because of the surface defects and (2) potential barrier effect induced by grain boundary are the plausible origins.

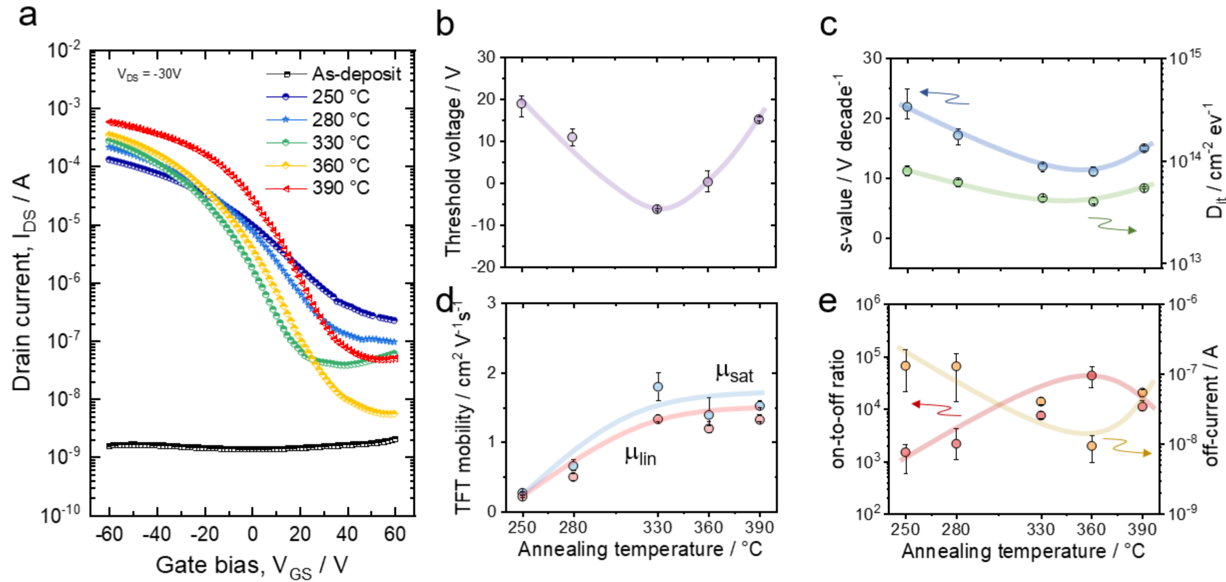

Figure 2. 9 (a) Variation of the transfer characteristics for unannealed and annealed SnO TFTs with a 7.5 nm thick channel. TFT parameters are as following: (b) V_{TH}, (c) *s*-value and D_{it}, (d) saturation and linear mobility, and (e) on-to-off current ratio and off-current at V_{GS} = 60 V.

Figure 2.9 (a) shows the variations of the transfer curves for the SnO TFTs with the 7.5 nm thick channel after thermal annealing at different temperatures. The unannealed device showed no clear field-effect current modulation, and the annealed temperature of at least 250 °C is required for the crystallization of SnO and demonstration of clear TFT operation. The film density of amorphous film is very low (d ≈ 5.42 g cm^{-3}), about ~15.3% lower than the film density of crystalline SnO (d ≈ 6.39 g cm^{-3}) (See **Figures 2.2**). Moreover, the X-ray photoemission spectroscopy (XPS) analysis shows that a large amount of Sn metal state is included in the unannealed films (**Figure 2.5**). The optical absorption analysis reveals that the unannealed film

had very broad and strong absorption over 10^5 cm^{-1} (**Figure 2.3**). These suggest that unannealed film includes a very high-density subgap defect over 10^{20} cm^{-3}, which causes no TFT operation because of the Fermi level pining and the reduction of effective electrical field induced by a gate bias. After post annealing treatment over 250 °C, single-phase SnO is formed, and all the devices show clear TFT action with p-channel mode. We also confirmed that NH_3 annealing maintains the SnO phase up to 390 °C, a higher temperature than the transition temperature of SnO to SnO_2 phase (~280− 300 °C) in thermal annealing in oxygen ambient.

The important TFT parameters are also summarized in **Figure 2.9 (b)−(e)**. The TFT performances are continuously improved up to 360 °C as the annealing temperature increases. The XPS analysis showed the reduction of V_o defect by annealing and confirmed a clear correlation between the V_o defect and TFT performances. Moreover, the V_{TH} variations can be also understood by the reduction of bulk defect density because the hole density is almost irrespective of the change in annealing temperatures (**Figure 2.6**). However, TFT begins to degrade as the annealing temperature goes beyond 390 °C because of the formation of tin metal (**Figure 2.1** and **2.5**).

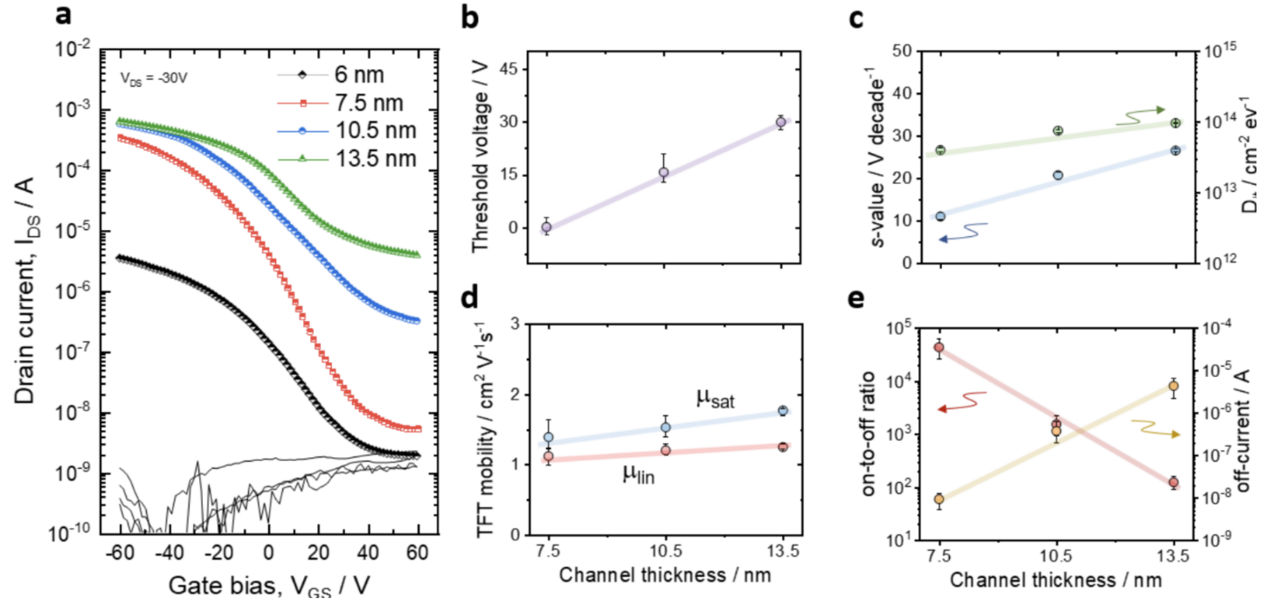

Figure 2. 10 (a) The variation of transfer characteristics of SnO-TFTs with different channel thickness of 6, 7.5, 10.5 and 15 nm after NH_3 annealing at 360 °C. The listed TFT parameters are (b) V_{TH}, (c) *s*-value and D_{it}, (d) saturation and linear mobility, and e) on-to-off current ratio and off- current level.

The best TFT performances of ~1.4−1.8 cm^2 V^{-1} s^{-1}, on-to-off ratio with 10^5, and *s*-value of ~10 V dec^{-1} were obtained from 360 °C-annealed SnO TFTs. From the dependency of *s*-value on the channel thickness of the 360 °C-annealed TFTs (**Figure 2.10**), the D_{it} and N_{ss} are found as 4.3 × 10^{13} and 8.50×10^{19} cm^{-3} eV^{-1}, respectively, which are the best of our knowledge in the reported SnO TFTs but still two or three orders of magnitude higher than those of *n*-type a-IGZO channels (D_{it} = 0.82 × 10^{11} cm^{-2} eV^{-1} and N_{ss} = 3.2 × 10^{16} cm^{-3} eV^{-1}).[100]

2.5 The device and material computation for identifying the origin of subgap defects

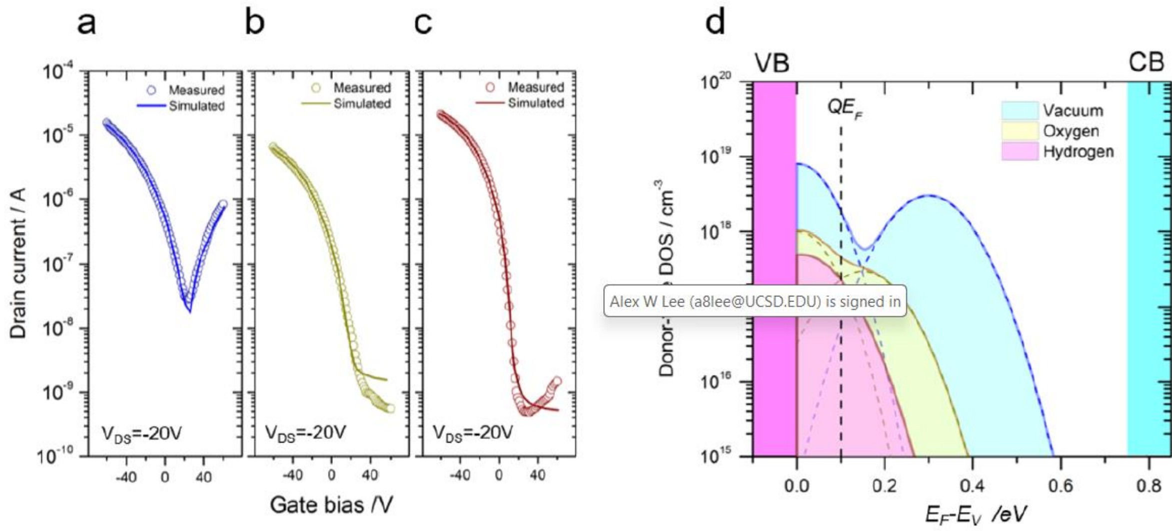

Figure 2. 11 Measured (symbols) and simulated (lines) transfer curves at V_{DS} = −20 V for (a) the vacuum-annealed, (b) oxygen-annealed, and (c) hydrogen-annealed TFTs. (d) Corresponding subgap DOSs were extracted from the device simulations for the vacuum-annealed (blue), oxygen annealed (yellow), and hydrogen-annealed TFTs (red). Quasi-Fermi level (Q_{EF}) lies at $E_F − E_V$ = 0.1 eV.

To investigate the origin of the TFT improvement in the hydrogenated SnO channel, the subgap trap state is extracted by TFT device simulation. **Figure 2.11 (a)−(c)** displays the measured and simulated transfer curves for the annealed SnO TFTs with the W/L ratio of 0.2. For comparison, the devices produced by vacuum annealing and oxygen atmosphere at 260 °C are also shown. TFT performances are strongly dependent on the annealing atmospheres. The vacuum-annealed TFT exhibits ambipolar characteristics while the *n*-channel mode is well suppressed in the oxygen-annealed device. We found that all the measured curves were reproduced by only optimizing the donor-type defect with Gaussian distribution-type, $g_G(E) = N_{GD} \cdot \exp\{-[(E - E_v)/W_{GD}]^2\}$ (where E_v is the valence band edge energy, E_0 is the central energy of $gG(E)$, W_{GD} is the characteristic decay energies, and N_{GD} is the state densities at E_0), which mainly works as a

hole trap for the *p*-channel device. The extracted corresponding subgap density of states (DOSs) are illustrated in **Figure 2.11 (d)**. (See **Table 2.1** for comparison of the measured and simulated TFT parameters).

Table 2. 1 Comparison of the measured and simulated TFT parameters of SnO-TFTs. Hole density was obtained by the Hall-effect measurement of thin film samples. Acceptor density is a setting value for T-CAD simulation.

	Vacuum-annealed		**Oxygen-annealed**		**Hydrogen-annealed**	
	(Meas.)	(Sim.)	(Meas.)	(Sim.)	(Meas.)	(Sim.).
V_{TH} (V)	6.0	5.8	4.0	4.6	4.5	4.3
***s*-value (V/dec.)**	14.3	13.5	12.5	11.7	5.2	5.0
Saturation mobility (cm^2/Vs)	0.9	0.83	0.6	0.72	1.6	1.7
On/off current ratio	$>6\times10^2$		$>2\times10^4$		$>5\times10^4$	
Acceptor density (cm^{-3})		1.2×10^{18}		5.0×10^{17}		9.5×10^{17}
Hole density (cm^{-3})	$\sim1.5\times10^{18}$		3.5×10^{17}		9.5×10^{17}	

In order to reproduce the ambipolar transfer characteristics for the vacuum-annealed TFTs, two donor-like Gaussian DOS are required with high-density DOS of $>10^{19}$ cm^{-3}. The high-density defect is distributed in the whole subgap region and exists even near the CBM (E_c - 0.2 eV). The near-CBM donor-like defect is likely to work as an electron donor, and consequently, the Fermi level (E_F) is shifted to the CB. Therefore, the vacuum-annealed TFT exhibits ambipolar characteristics comprising hole and electron transports in the present applied gate bias. Thermal annealing in oxygen ambient eliminates the subgap donor-like defect, and ambipolar behavior disappears in the oxygen-annealed devices. From these observations, oxygen vacancy seems to play an important role in the variation of TFT operation mode because it is reasonable that oxygen vacancy defect is easily generated by vacuum annealing and compensated by oxygen-containing annealing. Hydrogen-containing annealing clearly offers the better reduction of subgap trap state in the SnO channel with near VB-DOS of $\sim10^{18}$ to 10^{19} cm^{-3}.

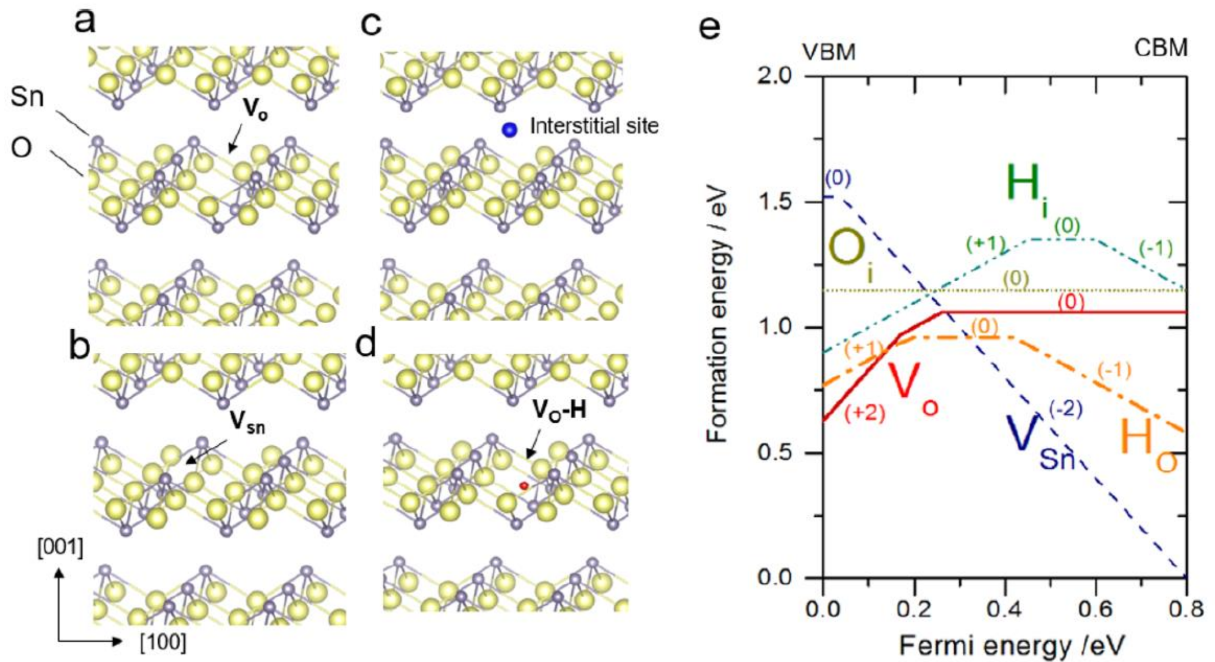

Figure 2. 12 (a) Oxygen vacancy (V_o), (b) tin vacancy (V_{sn}), (c) interstitial site for oxygen (O_i) and hydrogen (H_i), and (d) oxygen vacancy− hydrogen complex (H_o) in SnO. (e) Formation energies of these native defects as a function of Fermi level under Sn-rich limit condition.

We also investigated the origin of donor-like subgap defect and the role of hydrogen via native point defect analysis using DFT material calculation. A 108-atom supercell (3 × 3 × 3 unit cells) was used for the defect calculation for native defects such as oxygen vacancy (Vo), oxygen interstitial (O_i), and tin vacancy (V_{Sn}) in SnO (see the defect model in **Figure 2.12 (a)−(c)**. We also examined the formation energies of hydrogen impurity including hydrogen interstitials (H_i) and complex defects with V_o (H_o), in which the H atom sits at the center of the vacancy (**Figure 2.12 (d)**).

Figure 2.12 (e) shows the formation energies of native defects as a function of the E_F under the Sn-rich limit, which corresponds NH_3 annealing with the reduction conditions. The VBM sets to $E_F = 0$ eV. These defects are energetically favorable native defects. O_i has no defect transition level in the band gap region and thereby is electrically inactive. V_{Sn} forms shallow double acceptor

states with the defect transition levels for ε (−/2−) of ∼0.05 eV just above the VBM. The transition level is very close to the acceptor level estimated from the temperature dependence of electrical measurement (∼45 meV), and thereby V_{Sn} is a source of *p*-type conduction in SnO. On the other hand, V_o exhibits the defect transition levels of ∼0.2 eV for ε (0/2+) above the VBM and forms a deep double donor state from VB. These results are well agreed with the previous report.[101] The energy level of donor state is deep enough to work as an electron donor because it corresponds E_c - 0.6 eV, and it is not likely to work as an electron donor. This would mainly work as a hole trap state for *p*-channel oxide TFTs. The observation is well agreed with the above TFT simulation analysis. Therefore, we conclude that the origin of a hole trap is V_o, and the eliminating of V_o is a key to improve TFT characteristics of SnO TFTs. We also confirmed that hydrogen impurity is energetically stable in SnO. The formation energy of H−V_o complex defect is low enough, suggesting that hydrogen can terminate oxygen vacancy by forming the Sn−H bond in Sn-rich condition. Therefore, the hydrogen-containing thermal annealing reduces a hole trap by terminating V_o defects. Rutherford back-scattering spectrometry (RBS) and hydrogen forward-scattering analyses suggest that hydrogen can easily diffuse into the SnO film by hydrogen annealing and can produce the hydrogenated SnO channel with a high H concentration of $\sim 10^{21}$ cm^{-3} (see **Figure 2.7**).

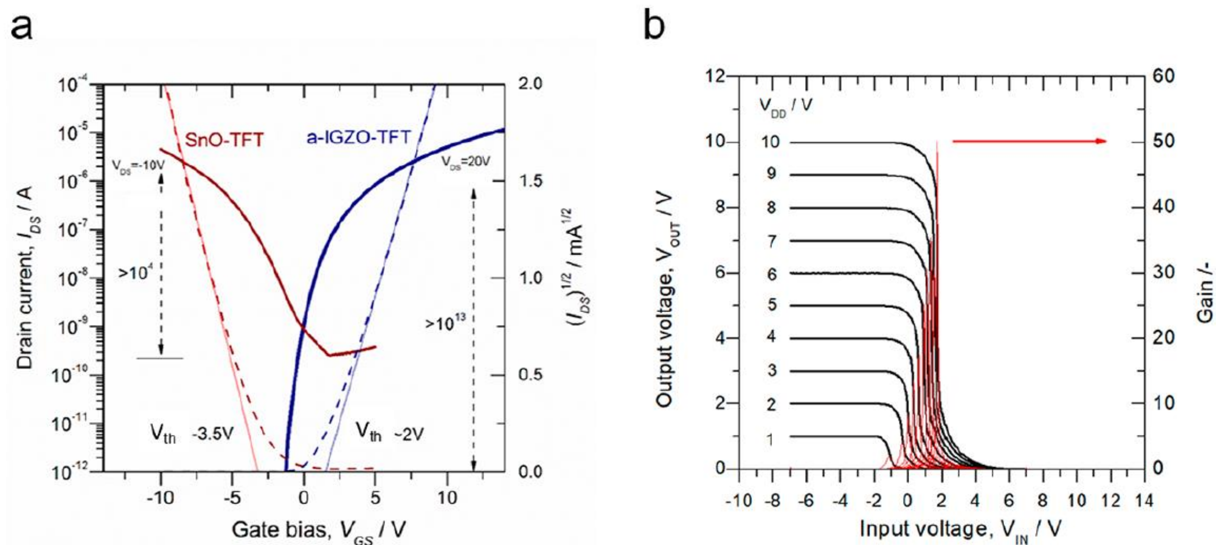

Figure 2. 13 (a) Transfer characteristics of a p-channel-SnO TFT (red line) with V_{DS} = 10 V and n-channel a-IGZO TFT (blue line) at VDS = 20 V. The dashed lines show $(I_{DS})^{1/2}$−V_{GS} plots. (b) VTCs of the complementary inverter. The input voltage (V_{IN}) was scanned from −6 to +6 V with supply voltages (V_{dd}) of 1−10 V. The red lines show the voltage gain characteristics.

Finally, we demonstrated a complementary inverter operation using hydrogenated p-channel SnO and *n*-channel IGZO-TFTs with a bottom gate structure. Because SnO TFTs have a low mobility and large *s*-values as compared to that of a- IGZO TFTs, the large channel W/L ratio with 6 and thin SiO_2 gate oxide layer with 50 nm were employed for SnO TFT to balance their TFT characteristics (the W/L with 0.5 was used for the a-IGZO TFTs). Typical transfer characteristics for *n*-a-IGZO and *p*-SnO TFTs are displayed in **Figure 2.13**. The μ_{sat} and the V_{th} were ~1.2 $cm^2\ V^{-1}\ s^{-1}$ and −3.5 V for SnO TFTs and 12.9 $cm^2\ V^{-1}\ s^{-1}$ and +2 V for a-IGZO TFTs, respectively, which are comparable to their reported high-performance oxide TFTs.

Figure 2.13 (b) shows the voltage transfer characteristic (VTC) consists of the *p*-SnO/*n*-a-IGZO-TFTs inverter. The supply voltage (V_{dd}) was varied from 1 to 10 V. Clear inverter action with the full swing close to the supply voltage was observed. The voltage gain is defined as dV_{OUT} / dV_{IN} of ~50 at maximum with V_{dd} = 10V. The inverter characteristic is highly symmetric with

respect to the switching threshold voltage (V_{inv}), and the V_{inv} values were ~ -0.4 V at V_{dd} = 2V, ~0.3 V at V_{dd} = 4V, ~0.9 V at V_{dd} = 6V, ~1.3V at V_{dd} = 8V, and ~1.7V at V_{dd} = 10V. The ideal V_{inv} is theoretically demeaned by $V_{inv} = (\beta_n / \beta_p)^{1/2} V_{th,n} + (V_{dd} – V_{th,p}) / [1+(\beta_n / \beta_p)^{1/2}]$, where $\beta_{n,p}$ are transconductances of *n*- and *p*-type TFTs, respectively, which provides ~3.8 V at V_{dd} = 2V, ~4.9 V at V_{dd} = 4V, ~5.9 V at V_{dd} = 6V, ~6.9V at V_{dd} = 8V, and ~7.9 V at V_{dd} = 10V. The large deviation is observed in the V_{inv}. The reason is not clear yet, but it would be related to the change of the β_n / β_p ratio by varying V_{dd} due to the V_{th} shift of *p*-channel SnO-TFTs.

2.6 Conclusion

In conclusion, we developed the hydrogen defect termination of *p*-type SnO for *p*-channel oxide TFTs. Thermal annealing in hydrogen ambient offers significant improvement of SnO channel and provides the improved TFT performance with the mobility of 1.4-1.8 $cm^2V^{-1}s^{-1}$ and the on-to-off ratio of 10^5. Computational device and material analysis concluded the near-VB donor-like defect controlled the TFT operation and is mainly originated from oxygen vacancy. Hydrogen can effectively terminate oxygen vacancy by forming Sn-H bonds. Although the device performance is still not satisfied and relatively behind the device performance of a-IGZO based *n*-channel TFT, good inverter operations with the voltage gain of ~50V were obtained by designing a proper TFT dimensions. Although we employed NH_3 gas as hydrogen source in thermal annealing in this study, several other processes such as the passivation formation process by ALD and CVD, in which hydrogen is involved, can also be adapted for hydrogen defect termination. There are still technological challenges need to be addressed on *p*-channel oxide technology such as TFT stability and reliability, but the present achievement provides a significant step towards the development of high-performance all-oxide based CMOS inverter technology.

2.7 Acknowledgement

Chapter 2, in full, is a reprint of the material as it appears in Lee, Alex, and Kenji Nomura. "Hydrogen Defect Termination in SnO for *p*-channel TFTs." *ACS Appl. Electron. Mater*. 2020, 2, 1162-1168. The dissertation author was the primary investigator and author of this paper.

Chapter 3. Switching Mechanism behind the Device Operation Mode in SnO-TFT

3.1 Introduction

Tin monoxide (SnO) is a promising oxide semiconductor to develop *p*-channel oxide TFTs because of its attractive properties such as relatively good high hole mobility (~2 cm^2/Vs) and low-temperature processability below 300 °C.[30,90] Very recently, we developed the hydrogen defect termination for SnO channel and improved device characteristics of *p*-channel SnO-TFT.[102] Although the defect density of SnO channel is reduced by the hydrogen termination, the absence of ambipolarity, which means both electrons and holes concurrently contributing to the field-effect conductions[103], in SnO-TFTs is still remained as a question. SnO is known as the only material in oxide semiconductors to operate in ambipolar TFT, owing to its narrow indirect bandgap of 0.7-0.9 eV.[38] So far, two types of operation modes, *p*-channel and ambipolar modes, are identified from SnO-TFTs.[104] However, most of the studies are focused on *p*-channel mode in SnO, while only a few studies are available for the ambipolar mode because of insufficient understanding of controlling device operation mode in SnO-TFT. Ambipolar TFT is particularly appealing for fabricating high-density CMOS circuits since using the same material for *n*- and *p*-channel TFTs will solve an issue with incompatibility in processing different active channel layer materials. Moreover, ambipolar-TFT based CMOS inverters can easily switch polarity by changing the input voltage (V_{IN}) and supply voltage (V_{DD}) of the inverter, which makes ambipolar oxides to fit in developing novel logic circuits.[103] Therefore, it is essential to clarify the origin behind the different operation modes in SnO-TFT to control its device operation modes and further improve the device performances for a broader application.

Here, we investigated the operation modes in SnO-TFTs and revealed that there is a significant correlation between back-channel surface defects and transistor operation modes. We fabricated inverter-staggered SnO-TFTs and controlled the back-channel surface defects by chemical wet-etching, thermal annealing, and passivation layer formation. It was found that excessive back-channel defects introduced by surface-etching removed the ambipolarity in SnO and made the device to only operate in *p*-channel mode, while the elimination of these defects recovered the ambipolarity in the device. The TFT device analysis and photoconductance decay measurement were used for the back-channel surface defect evaluation. We also fabricated CMOS-like inverters using two identical ambipolar SnO-TFTs and analyzed the inverter characteristics.

In this chapter, the switching mechanism behind the device operation mode in SnO is introduced for developing high performance *p*-channel and ambipolar TFT and high gain CMOS like inverter circuit based on ambipolar SnO-TFTs. Ch. 3.2 will introduce the experimental methods used to 1) deposit and anneal SnO film, and back-channel deposition process for Al_2O_3 layer 2) characterize SnO thin film. Ch. 3.3 shows the detailed material characterization used to identify the SnO thin film properties. Ch. 3.4 demonstrate the electrical characteristic of the back-channel engineered SnO-TFT devices with extracted device parameters. Ch. 3.5. discusses the subgap defect density of state (DOS) of back-channel engineered SnO-TFT. Ch 3.6. shows the CMOS-like inverter performance of the ambipolar SnO-TFTs.

3.2 Experimental Methods

3.2.1 Thin-film and device fabrication

Inverter-staggered TFT structure with ~7.5 nm of SnO channel was fabricated on thermally oxidized SiO_2 (thickness is ~150nm) / n^+-Si substrate. SnO thin films were deposited by pulse laser deposition (PLD) with KrF excimer laser at room temperature (RT). The oxygen partial pressure during the deposition was fixed at 2×10^{-4} Pa. Hydrogenated SnO was fabricated by thermal annealing at 260 ^oC for 30 minutes with $N_2 + H_2$ (5% hydrogen). Indium tin oxide (ITO) film was used for source and drain contact. The channel width (W) and length (L) were 300 μm and 50 μm, respectively. Extra defects were intentionally introduced by chemical wet-etching with Tetramethylammonium hydroxide (TMAH, weight percent < 3% in water) for 30 seconds at RT. For the removal of the back-channel surface defects, 5 nm of aluminum oxide (Al_2O_3) passivation layer was deposited on pristine SnO by atomic layer deposition (ALD) with Trimethylaluminum and H_2O precursor at the deposition temperature of 80, 200, 250 and 300 ^oC. CMOS-like inverters were fabricated by using two identical ambipolar SnO-TFTs with 5 nm of back-channel passivation layer deposited at ALD temperature of 300 ^oC.

3.2.2 Thin-film and device characterization method

Film structures were examined by grazing incidence X-ray diffraction (GIXRD) with an incident angle of 0.5° and confirmed all condition of thin films were polycrystalline SnO with no preferred crystal orientations. (**Figure 3.1**) UV-vis spectrophotometer was used to measure the optical transmittance, reflectance spectra and extract net absorption of the film. The indirect bandgap is estimated as ~0.8 eV for all films. (**Figure 3.2**) Hall-effect mobility and carrier concentration were determined from Hall-effect measurement using the van der Pauw

configurations. The photoconductance decay curve was measured by microwave photoconductance decay (μ-PCD) with yttrium lithium fluoride (YLF) pulsed laser (λ = 349 nm) at RT. TFT characteristics were measured by a semiconductor parameter analyzer at RT in air.

3.3 Material Characterization of back-channel engineered SnO film

3.3.1 The film structure of the pristine and surface modified SnO-films

The thin film structure of the pristine and surface modified SnO was analyzed by grazing incidence X-ray diffraction (GIXRD) with an incident angle of 0.5°. The film thickness is ~10.5 nm. **Figure 3.1** shows the GIXRD patterns for the pristine and back-channel surface modified SnO films. The back-channel surface is modified by 1) surface wet-etching and 2) ALD-Al_2O_3 passivation. A series of diffraction peaks appeared at 29.8^o, 51.6^o, 57.3^o, and 62.0^o are assigned to (101), (201), (211), and (202) planes, indicating non-preferred oriented polycrystalline nature of SnO films. The peak intensity is highest for ALD-Al_2O_3 passivated SnO film, suggesting that the crystallinity is improved by ALD process.

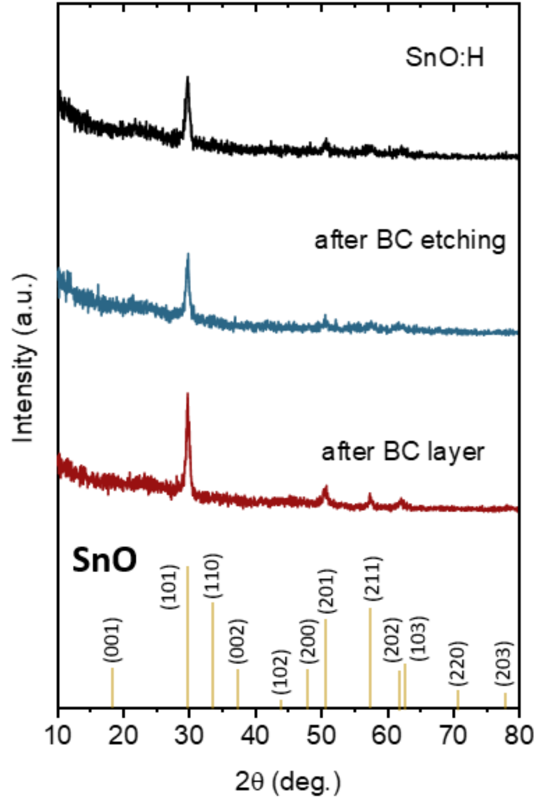

Figure 3. 1 The GIXRD of SnO films before and after surface wet-etching and ALD-Al_2O_3 passivation at 300 ^oC. The powder diffraction data (PDF #04-005-4540) was used to identify the measured pattern. A halo peak around ~24° is due to the glass substrate.

3.3.2 The optical absorption spectra of the pristine and surface modified SnO-film

Figure 3.2 (a) shows the optical absorption spectra of SnO films shown in **Figure 3.1**. No significant difference is observed from all measured films. The direct and indirect bandgap were determined from the $(\alpha hv)^2$ vs. hv and $(\alpha hv)^{1/2}$ vs. hv plots (**Figure 3.2 (b)-(d)**). The direct bandgap of ~2.6 eV and indirect bandgap of ~0.8 eV is obtained, which are in good agreement with the reported data.[105]

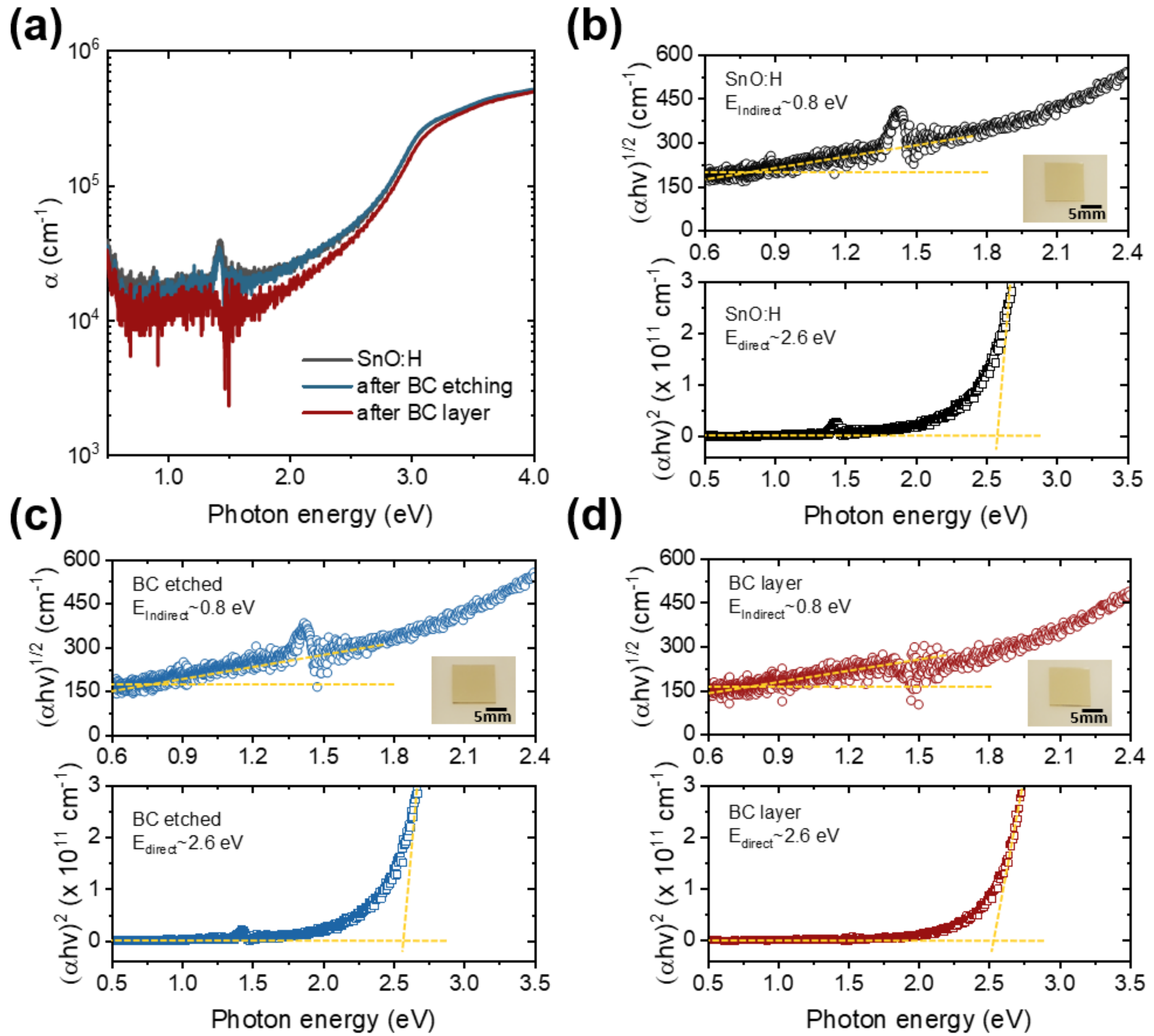

Figure 3. 2 (a) The optical absorption spectra of SnO film before and after surface wet-etching and ALD-Al_2O_3 passivation at 300 °C. The $(\alpha h\nu)^2$ vs. hν and $(\alpha h\nu)^{1/2}$ vs. hν plots for (b) pristine, (c) surface-etched, and (d) ALD-Al_2O_3 passivated SnO films.

3.4 TFT Characterization of back-channel engineered SnO-TFT

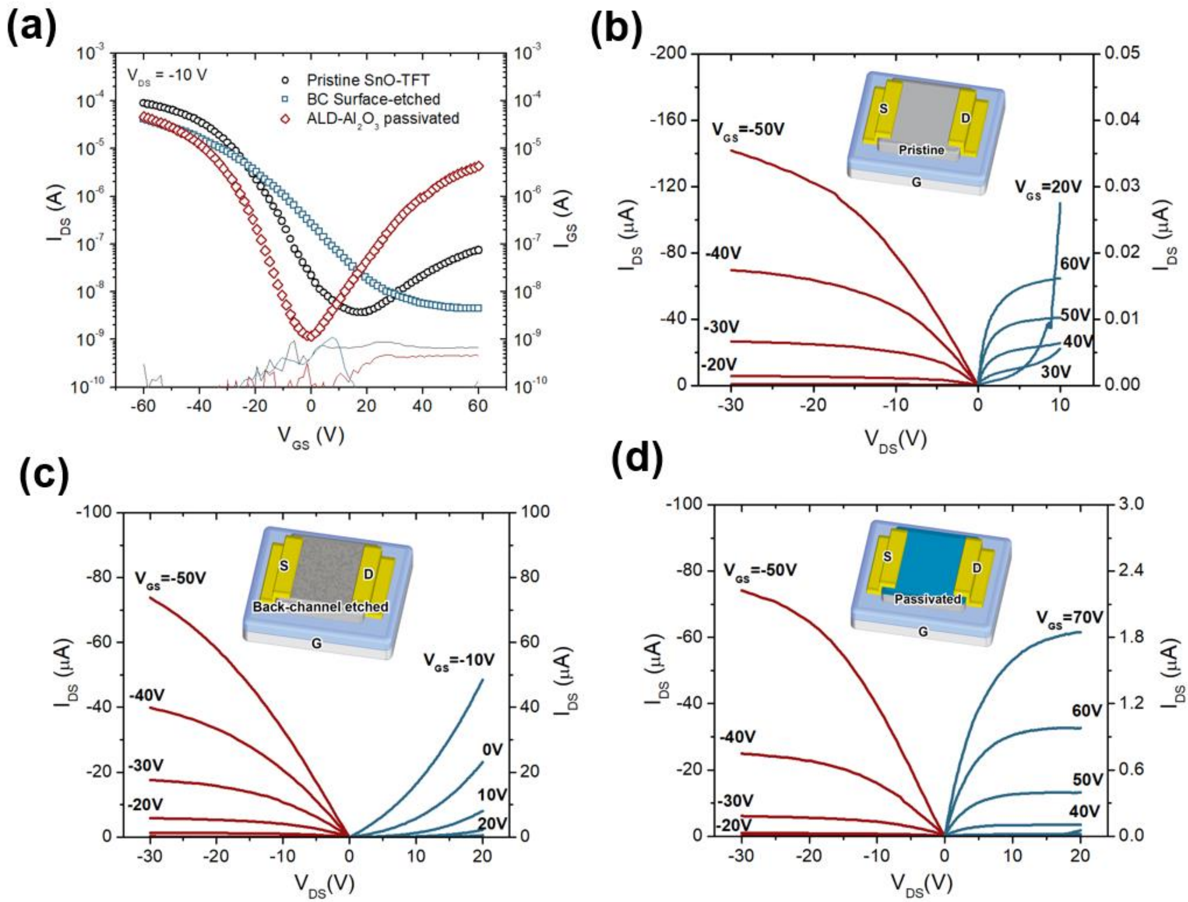

Figure 3. 3 (a) The variation of transfer characteristics for SnO-TFTs before and after back-channel surface defect modification. Output characteristics for (b) pristine, (c) back-channel surface etched, and (d) ALD-Al_2O_3 passivated TFT. The deposition temperature for ALD-Al_2O_3 passivation layer is at 300°C.

Figure 3.3 (a) shows a typical variation of the transfer characteristics, *i.e.* drain current (I_{DS}) versus gate bias (V_{GS}), of SnO-TFTs before and after the back-channel surface defect modification by a surface wet-etching and ALD-Al_2O_3 layer passivation. The corresponding output characteristics, *i.e.* drain current (I_{DS}) versus drain bias (V_{DS}), are also shown in **Figure 3.3 (b)-(d)**. The pristine SnO-TFTs exhibit an asymmetrical ambipolar behavior with strong *p*-channel and very weak *n*-channel modes, exhibiting the large on-to-off current ratio of ~3×10^4 for *p*-channel mode as compared to ~10^1 for *n*-channel mode. The weak *n*-channel mode is also confirmed from the output characteristics shown in **Figure 3.3 (b)**. The important TFT parameters (threshold voltage (V_{TH}), turn-on voltage (V_{on}), subthreshold swing value (*s*-value), and saturation mobility (μ_{sat})) are summarized in **Table 3.1**. The V_{TH} is determined from a straight line in a $(I_{DS})^{1/2}$ - V_{GS} plot to the V_{GS} axis, while μ_{sat} is calculated using $I_{DS} = W \cdot \mu_{sat} \cdot C_{\mathrm{ox}}/L \cdot (1/2 \cdot (V_{GS} - V_{TH})^2)$, where C_{ox} is a gate insulator capacitance per unit area. The pristine device turns at V_{on} of ~ 15.6V ± 1.0 and operates in depletion mode with a high hole density (N_h ~2.4×10^{18} cm^{-3}, determined by Hall-effect measurement). The estimated μ_{sat} is ~1.7 ± 0.2 for *p*-channel mode, which is reasonably high, and <10^{-3} cm^2/Vs for *n*-channel mode, respectively.

Table 3. 1 The TFT parameters of pristine and back-channel surface modified SnO-TFTs for *p*-channel mode shown in **Figure 3.3**.

	Pristine SnO TFT	Back-channel surface etched	ALD-Al_2O_3 passivated
V_{TH} (V)	-12.9 ± 3.2	-8 ± 4.6	-18.3 ± 2.5
V_{on} (V)	15.6 ± 1.0	55 ± 9.6	-0.5 ± 2.2
s-value (V/decade)	7.2 ± 1.5	14.3 ± 3.4	5.5 ± 0.8
μ_{sat} (cm^2/Vs)	1.7 ± 0.2	1.0 ± 0.3	1.2 ± 0.3
Hall mobility (μ_h, cm^2/Vs)	~1.5	~1.4	~0.4
Hole density (N_h, cm^{-3})	~2.4 × 10^{18}	~1.9 × 10^{18}	~2.3 × 10^{17}

After the excessive back-channel defects are introduced to SnO by wet-etching with diluted Tetramethylammonium hydroxide (TMAH, weight percent < 3% in water), the *n*-channel mode is completely disappeared, and TFT is operated only in *p*-channel mode. The *p*-channel TFT performance is also slightly degraded with the on-to-off current of ~10^4 and μ_{sat} of 1.0 ± 0.3 cm^2/Vs, but the observed TFT characteristics are nearly comparable to the most of reported *p*-channel SnO-TFTs.[102,106,107] Since the hole mobility and hole density are almost unchanged after the weak etching (*See* **Table 3.1**), the dramatic variation of TFT characteristics can be mainly attributed to the change of back-channel defects. Therefore, the absence of ambipolarity in the most reported *p*-channel SnO-TFTs is due to the high-density back-channel defects. Trap density (D_{it}) around the Fermi level (E_F) is estimated from the *s*-value with the following relation: $S = \log_e 10 \cdot k_B T/e \cdot [1+eD_{it}/C_{ox}]$, where k_B is a Boltzmann constant, T is the temperature, and e is an elementary charge. The D_{it} is increased by more than two times from ~1.7 × 10^{13} cm^{-2} eV^{-1} to > 3.5 × 10^{13} cm^{-2} eV^{-1} after the back-channel surface-etching.

In contrast, the ALD-Al_2O_3 back-channel passivated SnO-TFTs show the improved *n*-channel behavior and exhibit a clear symmetric ambipolar operation mode with the V_{on} very close to ~0 V. The μ_{sat} is still high for *p*-channel mode (~1.2 ± 0.3 cm^2/Vs), while it significantly is improved by more than one order of magnitude (~3 × 10^{-2} cm^2/Vs) for *n*-channel mode. It is notable that the *s*-value for *p*-channel mode is also improved to ~5.5V/decade, reflecting the reduction of D_{it} to ~1.3 × 10^{13} cm^{-2} eV^{-1}. We also deposited ALD-Al_2O_3 passivation layer to the back-channel surface etched devices to further verify the effect of the passivation on the appearance of ambipolarity. The recovery of ambipolarity after the passivation is clearly observed even in the back-channel etched devices. (**Figure. 3.4** and **Table 3.2**). These observations confirm the TFT operation modes are controlled by the back-channel defect states.

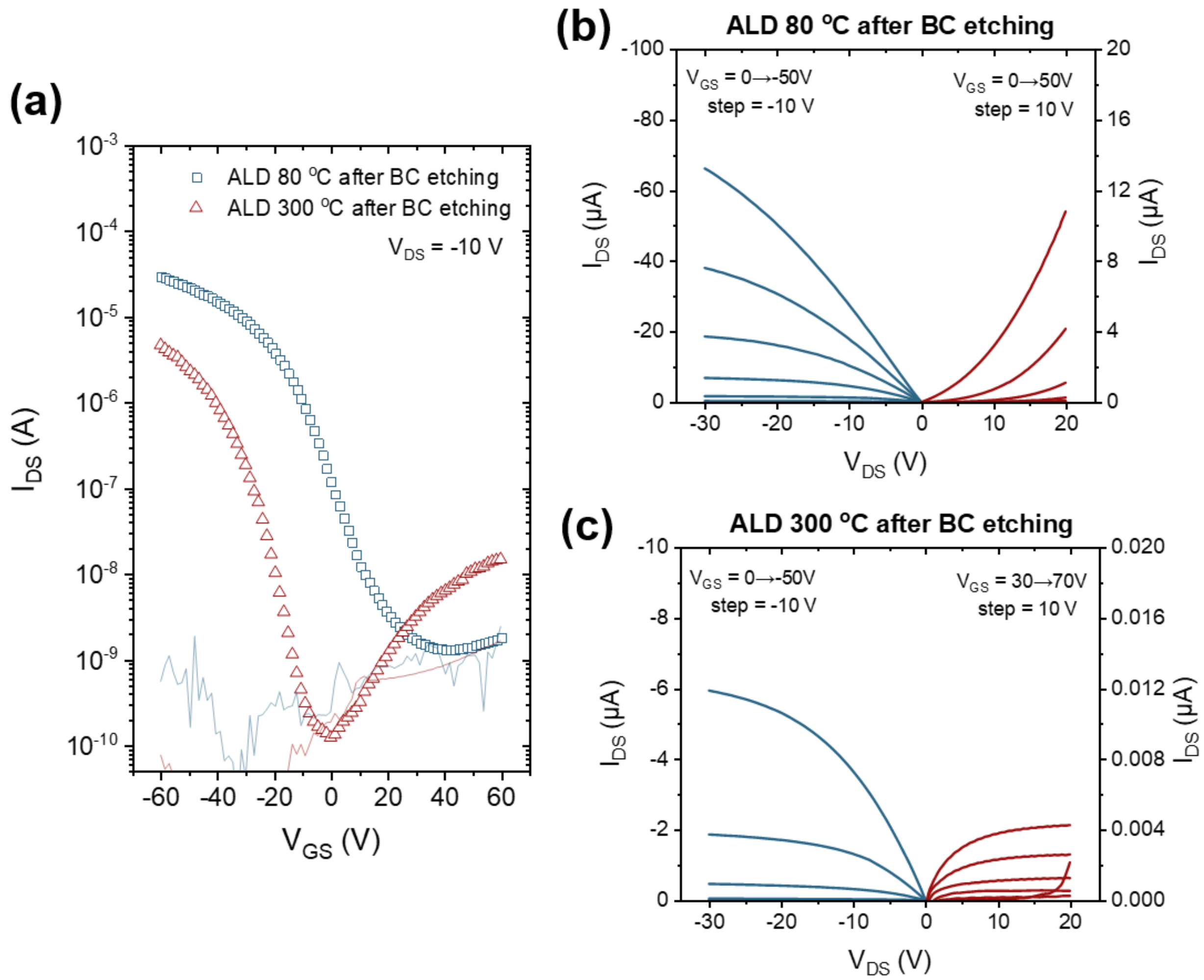

Figure 3. 4 The (a) transfer and (b-c) output characteristics of back-channel (BC) etched SnO:H TFTs after ALD-Al_2O_3 BC layer formation at 80 °C and 300 °C.

Table 3. 2 The device parameter extracted from ALD passivated back-channel etched device shown in **Figure 3.4**.

Condition	*Operation mode*	V_{on} (V)	V_{TH} (V)	*s-value* (V/decade)	μ_{sat} (cm^2/Vs)
ALD 80 °C after BC etched	*P-channel*	46.0	-3.2	10.5	0.8
	N-channel		–	–	–
ALD 300 °C after BC etched	*P-channel*	1.0	-21.0	5.6	0.1
	N-channel		9.3	15.4	~10^{-4}

However, the small reduction of D_{it} after the passivation makes it difficult to fully understand the improvement of ambipolarity. To verify the reduction of defect state, we analyzed the intrinsic back-channel surface and interface defect density at the Al_2O_3/SnO based on induced gap state (IGS) theory.[108] The intrinsic surface state density (D_{SS}) can be estimated by $D_{SS} = C_i/q \cdot (1/S_S - 1)$, where S_S is an interface parameter $[1 + 0.1\,(\varepsilon_{\infty SR} - 1)^2]^{-1}$, C_i is the capacitance density of the surface dipole $C_i = \varepsilon_{\infty S}/\delta$, in which $\varepsilon_{\infty SR}$ is a semiconductor optical relative dielectric constant, $\varepsilon_{\infty S}$ is a corresponding dielectric constant, δ is the microscopic dipole thickness. The interface state density (D_{IS}) is expressed by $D_{IS} = C_i/q \cdot (1/S_{IS} - 1)$, where $S_{IS} = \{1 + 0.1[(\varepsilon_{\infty IR} - 1)^2\,(\varepsilon_{\infty SR} - 1)^2/[(\varepsilon_{\infty IR} - 1)^2\,C_{iI}/(C_{iI} + C_{iS}) + (\varepsilon_{\infty SR} - 1)^2 C_{iS}/(C_{iI} + C_{iS})]]\}^{-1}$, C_i is the capacitance density of the interface dipole $C_i = C_{iI}C_{iS}/(C_{iI} + C_{iS})$, $C_{iI} = \varepsilon_{\infty I}/\delta_I$, $C_{iS} = \varepsilon_{\infty S}/\delta_S$, in which $\varepsilon_{\infty IR}$ and $\varepsilon_{\infty SR}$ are insulator and semiconductor optical relative dielectric constant, respectively; $\varepsilon_{\infty I}$ and $\varepsilon_{\infty S}$ are insulator and semiconductor dielectric constant, respectively. The D_{SS} was estimated as ~7.6×10^{13} cm^{-2} eV^{-1} for the pristine SnO surface, indicating the existence of high-density back-channel surface defects. D_{IS} was found to be only ~1.3×10^{13}

cm^{-2} eV^{-1}, nearly comparable to the observed D_{it} for ALD-Al_2O_3 passivated SnO-TFT at 300 °C. The analysis confirmed that ALD-Al_2O_3 passivation significantly reduced the back-channel surface defects.

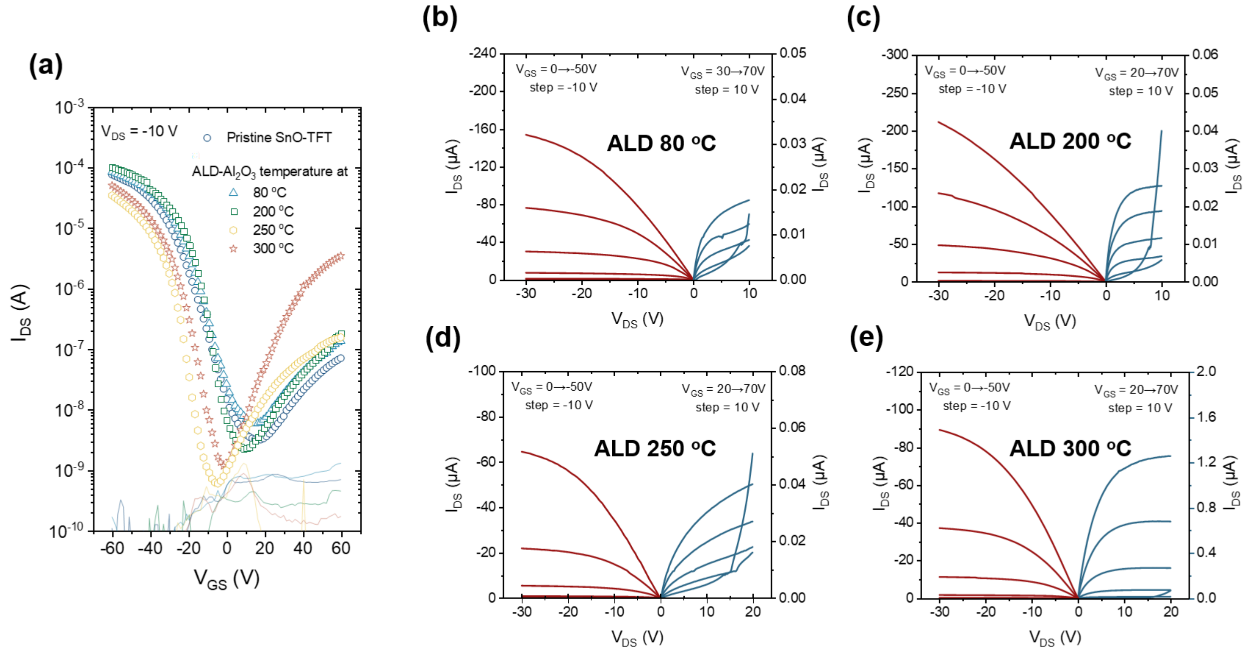

Figure 3. 5 (a) The transfer characteristics of SnO-TFTs with ALD-Al_2O_3 passivated layer deposited at different temperatures. The output characteristics of SnO-TFTs with ALD-Al_2O_3 temperature at (b) 80 °C (c) 200 °C (d) 250 °C, and (e) 300 °C.

Figure 3.5 shows the variation of transfer and output characteristics of SnO-TFTs with ALD-Al_2O_3 passivation layer deposited at different temperatures. For the comparison, the pristine device without the passivation layer is also shown. No noticeable change in the TFT characteristics was observed when the passivation layer was deposited at 80 °C. It is generally well-known that oxide-TFT characteristics are very sensitive to the environmental oxygen and moisture due to the surface bending effect by adsorption/desorption on the back-channel.[109] The observation indicates that

the improved ambipolarity is not solely coming from the shielding effect of ALD-Al_2O_3 layer to environmental exposures.

Table 3. 3 *P*- and *n*-channel device parameters corresponding to transfer and output characteristics shown in **Figure 3.5**

p-channel	V_{TH} (V)	V_{on} (V)	*s*-value (V/decade)	μ_{sat} (cm^2/Vs)
Pristine SnO TFT	-12.9 ± 3.2	15.6 ± 1.0	7.2 ± 1.5	1.7 ± 0.2
ALD 80 °C	-12.4 ± 2.7	15.2 ± 1.2	6.7 ± 1.7	1.8 ± 0.2
200 °C	-9.1 ± 3.1	4.8 ± 4.5	4.4 ± 1.3	2.6 ± 0.4
250 °C	-19.0 ± 2.8	-3.0 ± 3.1	4.7 ± 1.4	1.0 ± 0.3
300 °C	-18.3 ± 2.2	-0.5 ± 2.5	5.5 ± 0.8	1.2 ± 0.3

n-channel	V_{TH} (V)	*s*-value (V/decade)	μ_{sat} (cm^2/Vs)
Pristine SnO TFT	13.1 ± 3.6	24.8 ± 4.1	$<10^{-3}$
ALD 80 °C	11.2 ± 3.4	22.2 ± 3.9	$\sim10^{-3}$
200 °C	4.0 ± 4.2	16.1 ± 3.7	$\sim10^{-3}$
250 °C	8.3 ± 3.2	13.2 ±2.5	$\sim10^{-3}$
300 °C	17.9 ± 3.0	9.9 ± 1.3	$\sim3 \times 10^{-2}$

As listed in **Table 3.3**, the TFT characteristics including *s*-value and V_{on} are gradually improved by raising the passivation temperatures. However, there is no noticeable improvement in ambipolarity until the Al_2O_3 deposition temperature reaches 300 °C. Moreover, the apparent improvement in *s*-value with respect to the increase in the deposition temperature clearly suggests that the channel defect density is reduced by ALD process. SnO is thermodynamically unstable due to the disproportionation reaction and easily converts to *n*-type SnO_2 with high temperature thermal annealing.[110,111] We investigated the impact of the formation of SnO_2 to the TFT characteristics by using different annealing atmospheres. (**Figure 3.6**)

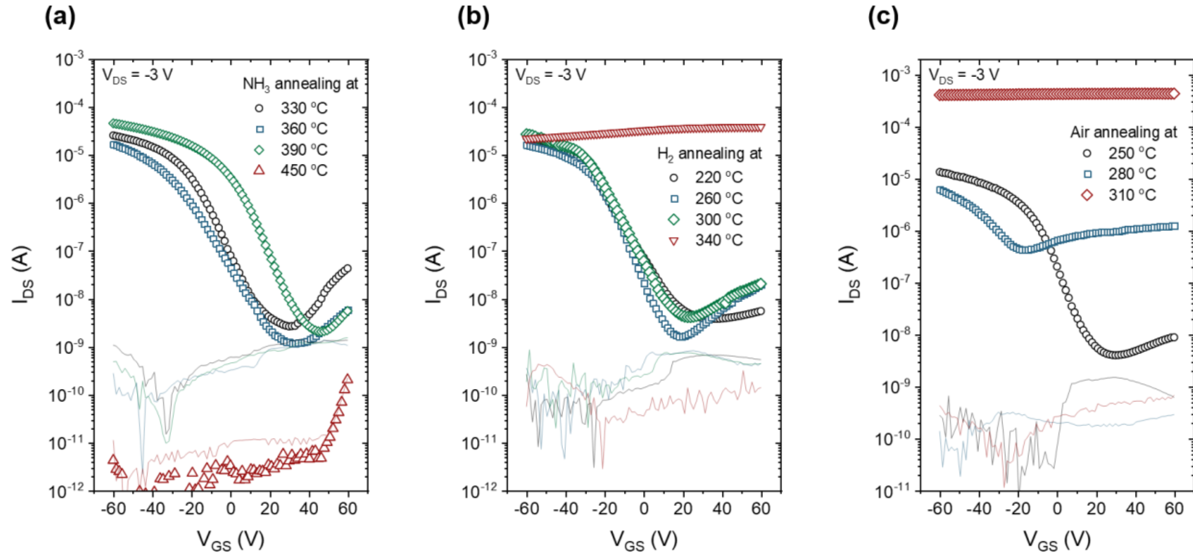

Figure 3. 6 (a)-(c) shows the variation of transfer characteristics of annealed SnO-TFTs in ammonia (NH_3), forming gas (H_2), and air-annealing conditions. The corresponding device parameters are listed in **Table 3.4.** The annealed devices showed the degradation of TFT characteristics at temperatures over ~390, ~300, and ~280 °C for NH_3, H_2, and air-annealing, respectively.

Table 3. 4 The TFT parameters extracted from the devices shown in Figure 3.6

	V_{TH} (V)	*s*-value (V/decade)	μ_{sat} (cm^2/Vs)	On/off ratio
NH_3 annealing at				
330 ^oC	-4.3	10.6	1.6	~1.0×10^4
360 ^oC	-8.1	13.4	1.4	~1.4×10^4
390 ^oC	13.2	11.8	1.8	~2.0×10^4
H_2 annealing at				
220 ^oC	-7.5	14.1	1.6	~6.1×10^3
260 ^oC	-8.6	9.2	1.4	~1.0×10^4
300 ^oC	-9.3	11.9	1.7	~6.5×10^3
Air-annealing at				
250 ^oC	6.2	9.8	0.6	~3.3×10^3
280 ^oC	-10.5	23.8	0.01	~1.5×10^3

The high-temperature annealing apparently causes the severe degradation of TFT characteristics for all annealing conditions. Therefore, the observed improvement of *n*-channel mode is not induced by the formation of SnO_2. We also performed the post-annealing for the device deposited with ALD-Al_2O_3 layer at 80 ^oC to activate the passivation effect (**Figure 3.7**). After air-annealing at 200 and 250 ^oC for an hour, V_{on} is shifted to near 0V, and the on-to-off current is improved to ~10^2 and ~10^3, respectively. The *p*-channel *s*-values are 6.1 and 5.3 v/decade for 200 and 250 ^oC air-annealed devices, respectively. Weak enhancement *n*-channel mode continued to 250 ^oC, following a similar trend we observed from ALD devices from **Figure 3.5**. μ_{sat} for *p*-channel and *n*-channel is 0.9 and ~10^{-3} for air-annealed device at 250 ^oC, respectively. At air-annealing temperature at 300 ^oC, the device turns into SnO_x, exhibit *n*-channel mode operation. Overall, we found a similar improvement on ambipolar characteristics as shown from device with ALD-Al_2O_3 passivated at 300 ^oC was observed after post-annealing in air at 250 ^oC.

From these observations, we speculate the improvement in ambipolarity is related to the termination of the defects by oxygen/hydrogen diffusion.

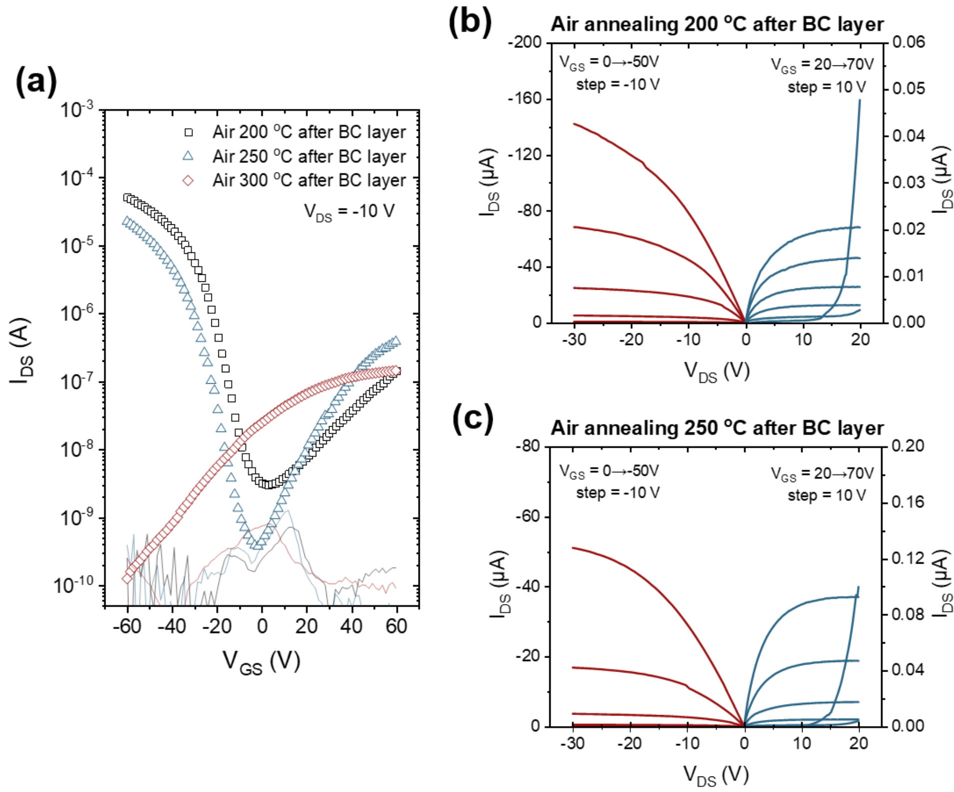

Figure 3. 7 The (a) transfer and (b-c) output characteristics of air-annealed SnO:H TFTs with different annealing temperature after ALD-Al_2O_3 BC layer formation at 80 °C.

3.5 Understanding subgap defect density of states (DOS) for back-channel engineered SnO

We next examined the DOS for the presented SnO-TFTs. The effective subgap DOS for the *p*-channel and ambipolar SnO-TFTs were extracted from field-effect conductance (FEC) method by using the following equation:[112,113]

$$DOS(E_F + \psi_{s,i}) = \frac{\varepsilon_s}{2e}\frac{\partial^2}{\partial\psi_{s,i}^2}\left(\frac{d\psi_{s,i}}{dx}\bigg|_S\right)^2 \ (i = 0,1,2,3 \dots)$$

where E_F is a Fermi level, $\psi_{s,i}$ is a surface potential, $\frac{d\psi_{s,i}}{dx}$ is a surface potential gradient, ε_s is a semiconductor permittivity, and i is a sequence beginning from flat-band to accumulation mode.

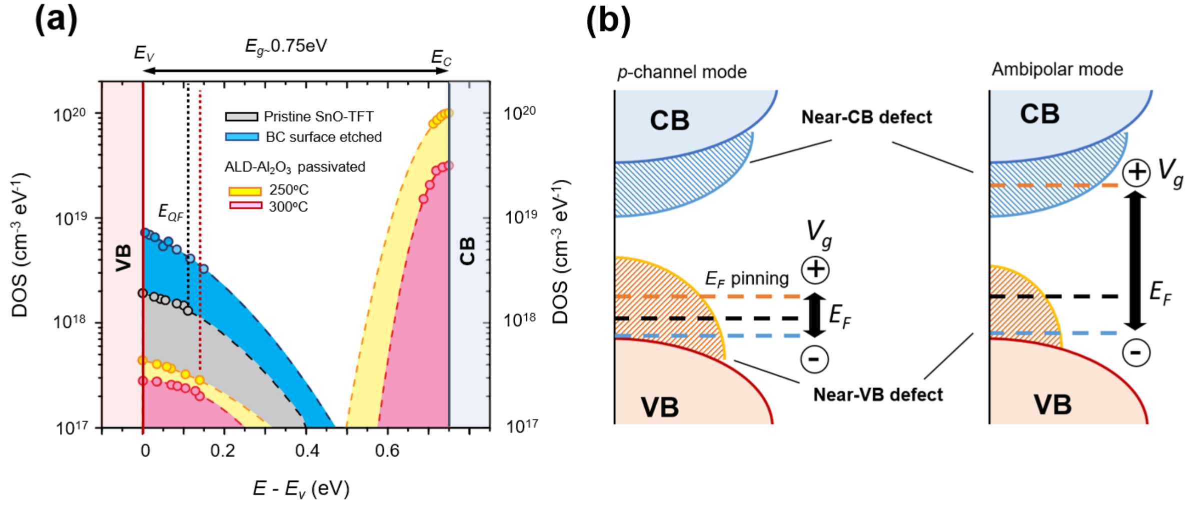

Figure 3. 8 (a) Effective subgap DOSs extracted from the field-effect conductance analysis for *p*-channel pristine, back-channel surface etched, and ambipolar SnO-TFTs with ALD-Al_2O_3 passivation layer deposited at 250 and 300 °C. E_{QF} denotes a quasi-static Fermi level. (b) Schematic energy diagrams to explain the variation of TFT operation modes: *p*-channel (left) and ambipolar modes(right). The black dashed line denotes the Fermi level at V_g=0V, while the orange and bule dashed line indicate the Fermi level swept by V_g=60V and V_g=-60V, respectively.

Figure 3.8 (a) shows the extracted subgap defect DOSs before and after the ALD-Al_2O_3 passivation. It is found that deep donor-type defects (near-valence band (VB) defects) and deep acceptor-type defects (near-conduction band (CB) defects) are involved in SnO channel. The surface defect structure can be comprehended from IGS perspective because the peculiar collective behavior of surface/interface states, which always seen as acceptor-like (donor-like) when the defect state located above (or below) the charge neutrality level. The pristine devices that operate in very weak ambipolar mode have somewhat high-density near-VB defects, which is estimated as $> 2\times10^{18}$ $cm^{-3}eV^{-1}$. Since the SnO channel is poly-crystalline, the observed near VB-defect DOS

is not exponential band-tail state and subgap state. This analysis is in a good agreement with the previous report of the near-VB-DOS by TFT simulations.[89,102] The existence of high-density near-VB defects limits the operation of *n*-channel mode due to the Fermi level pinning since near-VB defects are comparable or greater than a charge density induced by a gate bias in the presented TFT structure (~10^{18} cm^{-3}). (*See* the left in **Figure 3.8 (b)**) The near-VB defect is significantly reduced by the passivation and lower down to below ~3×10^{17} cm^{-3} eV^{-1}. In this case, Fermi level can smoothly swept toward the conduction band with the applied gate bias because the subgap DOS is more than one orders of magnitude smaller than the gate induced charge. (the right side in **Figure 3.8 (b)**). Therefore, the ALD-Al_2O_3 passivated device can exhibit a clear ambipolarity. The near-CB defects are also determined in the same manner and confirmed the reduction by increasing the ALD-Al_2O_3 passivation temperature. However, the near-CB defects are as high as ~2×10^{19} cm^{-3} eV^{-1}, about two-order of magnitude higher than the near-VB defects, even in our best device. Such high-density near-CB defects hinder the Fermi level from sweeping into the extended states in the conduction band. Therefore, the performance for *n*-channel mode is inferior to that of *p*-channel mode, causing the unbalanced electrical property in presented devices.

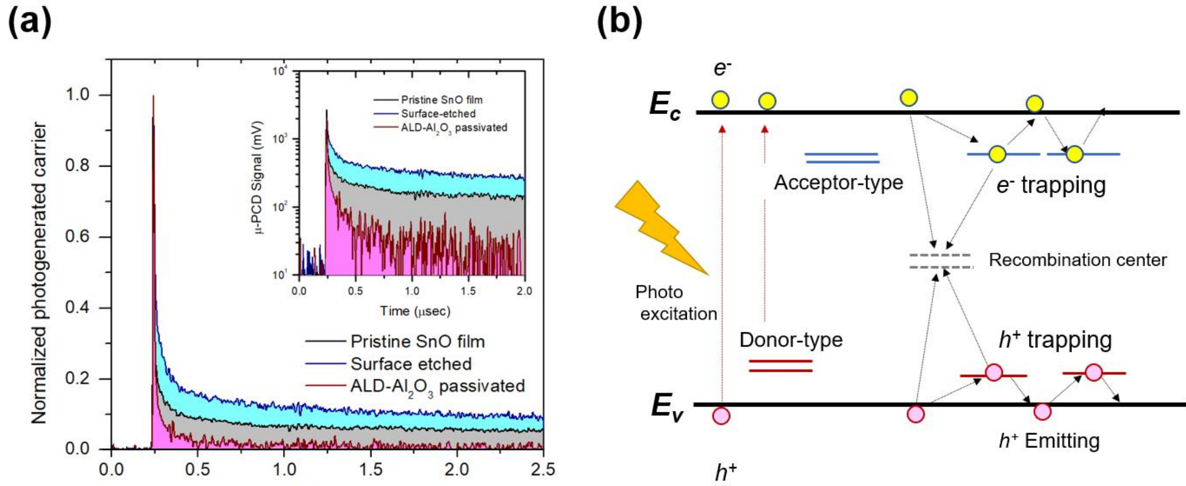

Figure 3. 9 (a) Normalized photoconductance decay spectra for the pristine SnO film (black), back-channel surface etched SnO film (blue), and ALD-Al_2O_3 passivated (red) SnO films at 300 ºC. The inset shows the μ-PCD reflectivity signal spectra. (b) The illustration of proposed hole trapping/emitting process at shallow state for the slow decay.

We also examined the photoconductance decay by μ-PCD technique to verify the reduction of the surface defect state after ALD-Al_2O_3 passivation. **Figure 3.9** shows the normalized photoconductance decay curves before and after the surface-etching, and ALD-Al_2O_3 deposition at 300ºC. The inset shows the observed μ-PCD reflectivity signal spectra. All of the measured films exhibit a typical photo-response behavior of semiconductor, which consist of strong distinct peaks of reflectivity signals generated just after the carrier photoexcitation and exponential decay. The exponential decay is expressed by $n_{ph}(t) = n_1 \exp\left(\frac{-t}{\tau_1}\right)^{\beta} + n_2 \exp\left(\frac{-t}{\tau_2}\right)$, where n_{ph} is the number of the photo-generated carrier, τ_1 and τ_2 are the time constant for fast and slow decay, respectively, and β is the stretching exponent part.[114] (*S*ee **Figure 3.10** and **Table 3.5** for the fitting)

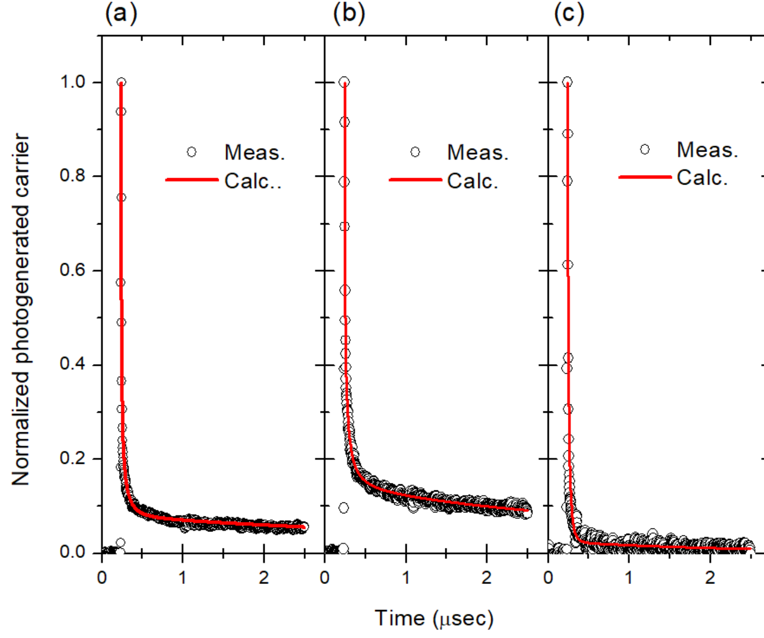

Figure 3. 10 The observed and calculated photoconductance decay curves for (a) pristine, (b) surface-etched, and (c) ALD-Al_2O_3 passivated SnO films at 300°C. The photoconductance decay curves were fitted with following equation:$n_{ph}(t) = n_1 \exp\left(\frac{-t}{\tau_1}\right)^{\beta} + n_2 \exp\left(\frac{-t}{\tau_2}\right)$, where n_{ph} is the number of the photo-generated carrier, and β is the stretching exponent part. All calculated curves are precisely replicated the observed curves. The photoconductance decay parameters were summarized in **Table 3.5**.

Table 3. 5 The photoconductance decay parameters extracted from Figure 3.10

	Pristine SnO	Surface-etched	ALD-Al_2O_3 passivated
n_1 (cm^{-3})	~1.7×10^{20}	~1.6×10^{20}	~1.9×10^{20}
$\boldsymbol{\tau_1}$ (nsec)	9.1	10.2	9.6
n_2 (cm^{-3})	~2.2×10^{20}	~3.0×10^{20}	-
$\boldsymbol{\tau_2}$ (μsec)	4.2	5.3	-

The fast decay, which is attributed to Shockley-Read-Hall (SRH) process, shows no significant difference in all films and the τ_1 is determined as ~9-10 nsec. In contrast, slow decay, which is often observed in oxides [115,116], is found to be strongly depended on the film surface quality. The slow decay process is almost completely removed from the ALD-Al_2O_3 passivated

SnO film as compared to the pristine film. Although the origin of slow decay is not clarified yet, we consider the near-VB defect (*i.e.,* hole traps) could play an important role because the E_F locates around the near-VB defect. Therefore, the observed slow decay process can be explained by hole trapping/emission mechanism. Photogenerated carriers are generated via direct valence-conduction band, and defect-band transitions by the light irradiation. Most photogenerated carriers are recombined within ~9-10 nsec by SRH process, but some carriers captured in hole traps are re-emitted into the valence band by thermal effect. This process repeatedly occurs and slows down the conductance decay.[117]

DFT calculation predicts the origin of near-VB defect in SnO is associated with the oxygen vacancy defects, which can be terminated with hydrogen by forming Sn-H bonds.[102,108] This suggests that oxygen vacancy defect, especially near surface region, is effectively compensated by ALD-Al_2O_3 passivation. Although Al_2O_3 is one of the most extensively researched passivation materials [119,120], it is currently difficult to judge Al_2O_3 is the best passivation material for SnO-TFT. During the ALD growth process, the considerable amount of hydrogen is generated from metalorganic precursors and reactants.[119,121,122] Considering our previous observation on role of hydrogen in termination of subgap defects, the massive hydrogen involved in ALD growth process can effectively reduce the subgap defects. Therefore, we believe any oxide materials can be used for passivation material (e.g. HfO_2[123]) as long as the growth process favors the reduction of subgap defects in SnO film. On the other hand, the origin of electron trap needs more investigation, but the ionized oxygen vacancy is considered as a one of the plausible sources.[124]

3.6 Ambipolar SnO-TFT based CMOS-like inverter

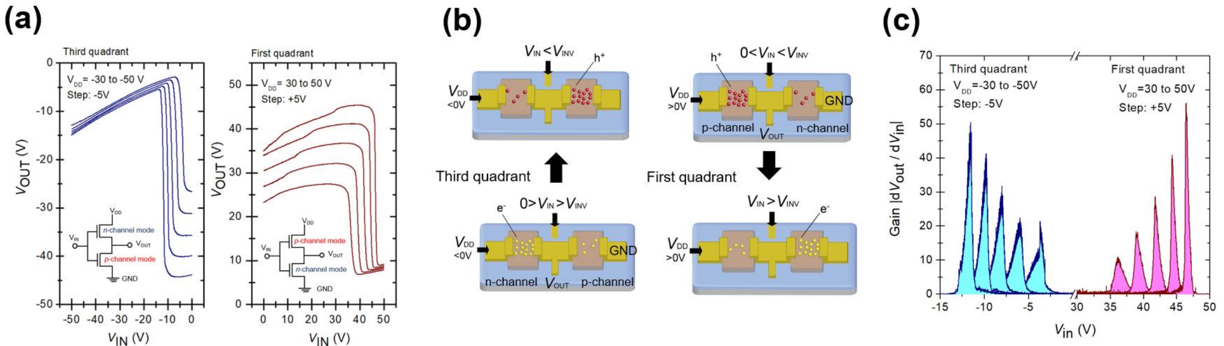

Figure 3. 11 (a) Voltage transfer characteristic (VTC) of ambipolar SnO-TFT based CMOS-like inverters at the first (positive V_{DD} and positive V_{IN}) (right) and third quadrant (negative V_{DD} and negative V_{IN}) (left). The insets indicate the schematic of CMOS-like inverter circuits. (b) The schematic illustration of carrier flow before and after the inversion for the first (right) and third quadrants (left). (c) The variation of inverter voltage gains at different V_{DD}.

Finally, CMOS-like inverters are fabricated by connecting two identical ambipolar SnO-TFTs with ALD-Al_2O_3 passivation layer deposited at 300 °C. **Figure 3.11 (a)** illustrates the voltage transfer characteristic (VTC) of CMOS-like inverters in first (*i.e.* positive V_{DD} and positive V_{IN}) and third quadrants (*i.e.* negative V_{DD} and negative V_{IN}). Inverter actions are clearly observed in both first and third quadrant regions, indicating each SnO-TFTs are switching by transiting *p*- and *n*-channel modes. This is a unique characteristic of inverter consist of ambipolar transistors.[125] Moreover, the output voltage (V_{OUT}) is not fully swing and altered by the V_{IN}. For the VTC in first quadrant (the right **in Figure 3.11 (a)**), for example, the V_{OUT} does not completely pull-up but instead gradually going up by increasing the applied V_{IN} before the inversion (*i.e.,* $0 < V_{IN} <$ inverter switching threshold voltage (V_{INV})). (the top right **in Figure 3.11 (b)**) The incomplete pull-up characteristics is originated from the fact that the minority hole flows through the *n*-channel mode TFT even at $V_{IN} > 0V$. Meanwhile, the V_{OUT} also shows the incomplete pull-down at $V_{IN} > V_{INV}$ due to the current induced by minority electron in the *p*-channel mode TFT (the bottom right in

Figure 3.11 (b)). (*S*ee **Figure 3.12** for detailed quantitative analysis for incomplete pull-up/down) Same ambipolar-inverter characteristics are seen in the VTC for third quadrant.

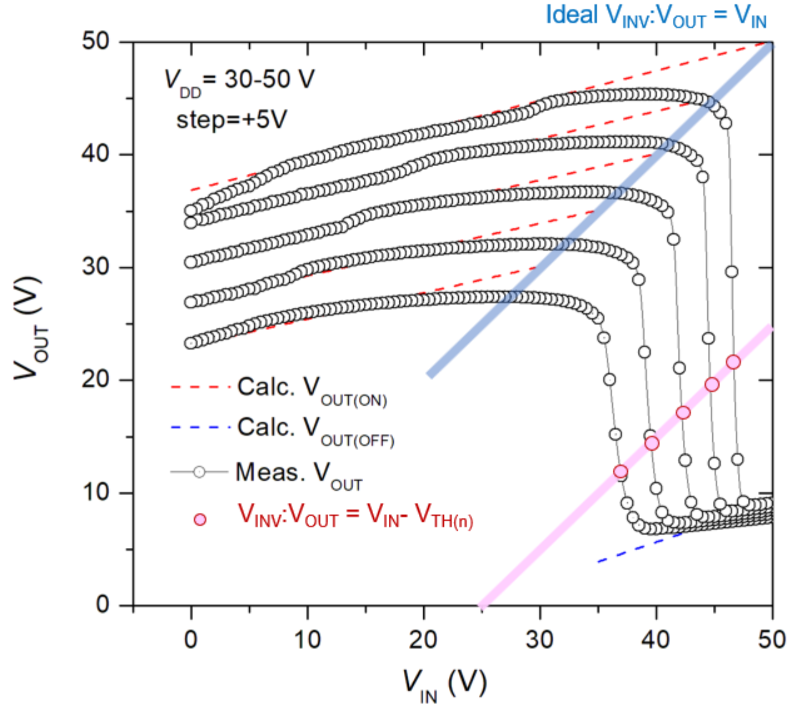

Figure 3. 12 The voltage transfer characteristics (VTC) of the ambipolar SnO-TFT based CMOS-like inverters in the first quadrant. Blue solid line: ideal V_{INV} condition. Red solid line: *n*-channel operation V_{INV} (V_{OUT}=V_{IN}–$V_{TH,n}$). The V_{INV} are switching threshold voltage corresponding to V_{DD} from 30V to 50V (step +5V), respectively. Red and blue dashed lines: calculated V_{OUT} for the on and off states.

Figure 3.12 shows the inverter voltage transfer characteristics (VTC) for the ambipolar SnO-TFT-based CMOS-like inverters in the first quadrant. The blue solid line indicates the ideal switching threshold voltage (V_{INV}), which can be defined as a point where V_{OUT}=V_{IN}. The red solid line indicates the calculated V_{INV} (V_{OUT}=V_{IN}–$V_{TH,n}$), considering the unbalanced electrical characteristics of *p*-and *n*-channel mode, *i.e.,* poor performances of *n*-channel mode. The calculated V_{INV} are ~36.9 V at V_{DD} = 30V, ~39.5 V at V_{DD} = 35V, ~42.2 V at V_{DD} = 40V, ~44.6 V

at V_{DD} = 40V, and ~46.6 V at V_{DD} = 50V, respectively, which are in good agreement with the observed V_{INV}.

Here, the V_{OUT} for ambipolar transistor-based inverter is expressed by the followings:[125]

For 0 < V_{IN} < V_{INV},

$$V_{OUT} = \left(V_{IN} - V_{TH,N} + |V_{TH,P}|\right) + \sqrt{\left(V_{DD} - \left(V_{IN} - V_{TH,n} + |V_{TH,p}|\right)\right)^2 \cdot \frac{\mu_p^p}{\mu_p^p + \mu_n^p}}$$

where $V_{TH,n}$, and $V_{TH,p}$ are the threshold voltage of *n*- and *p*-channel modes, respectively, V_{DD} is the supply voltage, and μ_p^p and μ_n^p are the hole mobility in *p*- and *n*-channel modes, respectively. Since identical ambipolar SnO-TFTs are used for inverter, $\frac{\mu_p^p}{\mu_n^p} \approx 1$.

For V_{IN} > V_{INV},

$$V_{OUT} = \left(V_{IN} - V_{TH,n}\right) - \sqrt{\left(V_{IN} - V_{TH,n}\right)^2 \cdot \frac{\mu_n^n}{\mu_n^n + \mu_p^n}}$$

where μ_p^n, μ_n^n are electron mobility in *p*-channel and *n*-channel modes, respectively. Since identical ambipolar SnO-TFTs are used for inverter, $\frac{\mu_n^n}{\mu_p^n} \approx 1$. The calculated V_{OUT}, as shown in the red and blue dashed lines, closely replicated the measured VTC.

The V_{INV} are determined as ~36.2 V at V_{DD} = 30V, ~38.9 V at V_{DD} = 35V, ~41.8 V at V_{DD} = 40V, ~44.3 V at V_{DD} = 45V, and ~46.4 V at V_{DD} = 50V, respectively. The ideal V_{INV} is defined as the point where V_{OUT} equals to V_{IN} but it cannot be applied to the presented device due to the unbalanced electrical characteristics of *n*- and *p*-channel mode in ambipolar SnO-TFT. Since the performance of *n*-channel mode is largely behind from that for *p*-channel mode, the inversion occurs when $V_{OUT}=V_{IN}-V_{TH,n}$, where $V_{TH,n}$ is threshold voltage of *n*-channel mode, is satisfied.[126]

The calculated V_{INV} are ~36.9 V at V_{DD} = 30V, ~39.5 V at V_{DD} = 35V, ~42.2 V at V_{DD} = 40V, ~44.6 V at V_{DD} = 45V, and ~46.6 V at V_{DD} = 50V, respectively, which are in a good agreement with the observed V_{INV}. For third quadrant, we also confirmed the observed V_{INV} is consistent with the calculated V_{INV}, The observed V_{INV} are ~ -3.6 V at V_{DD} = -30V, ~ -5.9 V at V_{DD} = -35V, ~ -7.9 V at V_{DD} = -40V, ~ -9.8 V at V_{DD} = -45V, and ~ -11.5 V at V_{DD} = -50V, respectively. (The calculated V_{INV} are -3.3, -5.8, -8.0, -9.8, and -11.6V for V_{DD} = -30, -35, -40, -45, and -50V, respectively.)

The voltage gain, defined as dV_{OUT}/dV_{IN}, is shown in **Fig. 3.11 (c)** with the peak gain over 50 for both first and third quadrants at V_{DD} = ±50V. The maximum peak gain reaches to ~82, and the average gain from 10 devices are 64.1±12.0 and 48.8±6.8 for the first and third quadrants, respectively (*S*ee **Figure 3.13**). The obtained voltage gain is higher than non-doped CNT-based CMOS-like inverter (gain ~5)[127] but slightly lower than voltage gain reported in other ambipolar transistor-based inverters such as SnO (~100)[89], 4Cl-Azapen (~180)[128], and Cu_3N (~100) [129]. These observations can be attribute to the unbalanced performances of *p*- and *n*-channel modes, where *n*-channel mode has a lower mobility and poor *s*-value in comparison to *p*-channel mode.

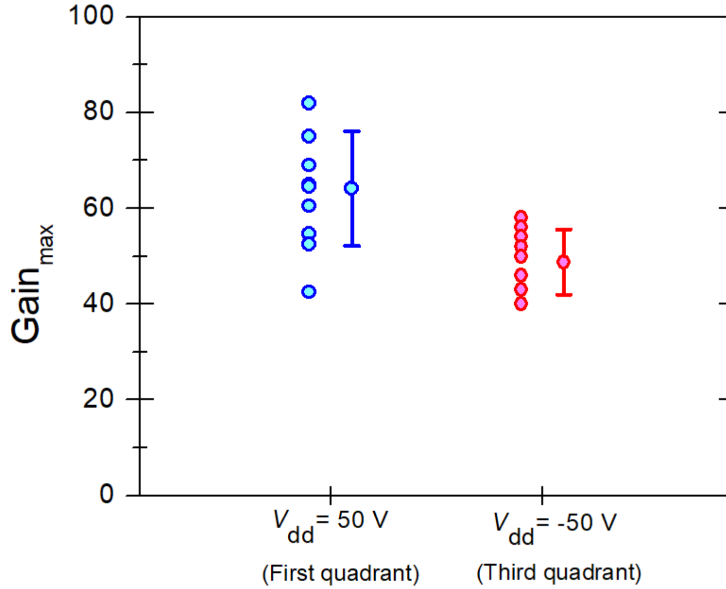

Figure 3. 13 The voltage gains for ambipolar SnO-TFT-based inverters for first and third quadrants (10 devices). The average voltage gains are 64.1±12.0 and 48.8±6.8 for the first and third quadrants, respectively.

3.6 Conclusion

We investigated the origin of switching mechanism behind the different operation modes, *p*-channel and ambipolar mode, in SnO-TFT by performing back-channel defect engineering and clarified the back-channel defect controlled the operation modes. The pristine SnO channel has high-density back-channel defects (near VB defect) over 10^{18} cm^{-3}, leading to strong *p*-channel and asymmetrical ambipolar operation modes. By introducing the back-channel surface defects through chemical wet-etching, the ambipolar mode was almost completely disappeared because of the Fermi-level pinning at near-VB defect. ALD-Al_2O_3 passivation can effectively reduce the back-channel defects and produces a good ambipolarity in SnO-TFTs. Ambipolar SnO-TFT based CMOS-like inverters demonstrated a reasonable high voltage gain > 60, but the unbalanced ambipolarity originated from the poor performances of *n*-channel mode limits the inverter performance. The future investigation needs to focus on the understanding of the origin of the

electron trap and advanced defect termination method to improve the performance of ambipolarity SnO-TFT and the CMOS-like inverter circuits.

3.7 Acknowledgement

Chapter 3, in full, is a reprint of the material as it appears in Lee, Alex, and Kenji Nomura. "Switching mechanism behind the device operation mode in SnO-TFT." *Adv. Electron. Mater.* (2022): 6, 2000742. The dissertation author was the primary investigator and author of this paper.

Chapter 4. Towards the ultimate limit of analyte detection in graphene based field-effect transistors

4.1 Introduction

Field-Effect Transistor (FETs) based sensors are attractive platforms for biochemical diagnostics in point-of-care applications due to their high sensitivity, rapid detection and relative ease of large-scale manufacture through harnessing available semiconductor fabrication infrastructure.[53-55] Recent developments in FET based sensors have received an exciting boost through the utilization of one- or two-dimensional materials with intrinsically high surface area to volume ratio as well as high charge carrier mobility[56-58], facilitating superior sensitivity as exemplified through the single atom sheet constituted graphene FET (GFET).[59-61] For specificity of analyte detection, the related surfaces typically have attached linker molecules, *e.g.,* 1-pyrenebutanoic acid *N*-hydroxysuccinimidyl ester (PBASE), followed by bioreceptors, such as aptamers (*Ap*), antibodies, and enzymes for specific binding to the target analyte.[63-65] The utilization of *Ap*, *i.e.,* single-stranded DNA or RNA oligonucleotides, is particularly attractive due to their enhanced stability, high selectivity, and ease of further modification (/adaptation) from (/to) various biologic as well as chemical functional groups.[66-68]

Indeed, many studies and approaches on improved sensitivity and selectivity of *Ap*-based biosensors have been conducted and reviewed in extant literature.[130-137] For instance, one approach includes the modification of the nucleobase of an *Ap* to improve the specificity of receptor probe.[132] These *Ap* are then connected to the sensing material surface through a linker[138], such as the PBASE. However, it has not yet been elucidated as to how the *Ap* – linker – material interaction affects the sensor performance. It was previously suggested, *e.g.,* through electrochemical and surface plasmon resonance studies, that the analyte binding affinity would be

inversely proportional to *Ap* surface coverage.[139,140] However, these studies are not directly applicable to two-dimensional material surfaces, relevant to FET sensing, given the substantial *Ap* modification, *e.g.,* use of redox tags such as methylene blue, electrode-free surfaces, *etc.* It would then be crucial to develop evaluation techniques that are both label-free and compatible with electronic devices. In this context, we have previously demonstrated how the limit of detection (LoD) of 2D material based sensors may be optimized through electrically monitoring the influence of the *Ap* incubation time on a graphene based FET, say for Pb^{2+} detection.[141] However, a clear rationale for the existence of such an *optimal* incubation time was not well understood, and it is one of the aims here to clearly elucidate the involved physical modalities for improved performance. Further, we aim to investigate the question of the *ultimate limit* of detection using the FET based principle. Would it be feasible to expect specificity and sensitivity at the single molecule or ion level, using *Ap* based methods?

In this chapter, Towards the ultimate limit of analyte detection in graphene based filed-effect transistor is introduced for developing highly sensitive and specific Pb^{2+} detecting senser and discussing the theoretical basis for reaching the single molecule detection in perspective of thermodynamics. Ch. 4.2 will introduce the thermodynamic approach we considered in developing GFET aptasensor. Ch 4.3 discusses the graphene characterization and device preparation process. Ch 4.4 shows the analysis of *Ap* distribution on graphene through Electrochemical Impedance Spectroscopy (EIS) and Atomic Force Microscopy (AFM). Ch 4.5 illustrates the LoD dependency of GFET aptasensor with varying *Ap* incubation condition that is determined from the results from Ch 4.4.

4.2 Thermodynamics approach in GFET aptasensor

For instance, in the case of lead ion (Pb^{2+}) detection, a Guanine (G)-rich sequence in the *Ap* was posited for specifically enhancing the binding affinity of such a *designed Ap* to Pb^{2+}. Here, the strong Pb^{2+} affinity to N7[(C6)O] sites of the guanine in comparison to N3/(C2)O, N3/(C2)O, and N7/(N1) sites of cytosine, adenine, and thymine[142,143] is of particular relevance. Based on such a principle, much effort has been consequently expended on the development of guanine-rich sequence constituted *Ap*, *e.g.,* AGRO100 (GGT GGT GGT GGT TGT GGT GGT GGT GG), PS2.M (GTG GGT AGG GCG GGT TGG), TBAA (GGA AGG TGT GGA AGG), TBA (GGT TGG TGT GGT TGG), and T30695 (GGGT GGGT GGGT GGGT) based biosensors. We chose the *Ap* designed T30695 *Ap* (5’-GGGTGGGTGGGTGGGT/−NH2−3′) in comparison to the other indicated *Ap* alternatives, on the basis that the estimated binding free energy ($\Delta G_{bind,\ Ap}$) – from molecular mechanics based Poisson-Boltzmann surface area methods (MM-PBSA), due to T30695 toward Pb^{2+} (at ~1320 kJ/mol) is *the highest*, significantly more than the other alternatives[144], implying the largest Pb^{2+} binding specificity. **Figure 4.1 (a)** indicates the variation in the $\Delta G_{bind,\ Ap}$ for the studied *Ap*, as a function of the estimated limit of detection (LoD). Essentially, a LoD of Pb^{2+} of ~ 0.42 nM would be expected per such a calculation, where both the *Ap* and the analyte ions are free in solution.

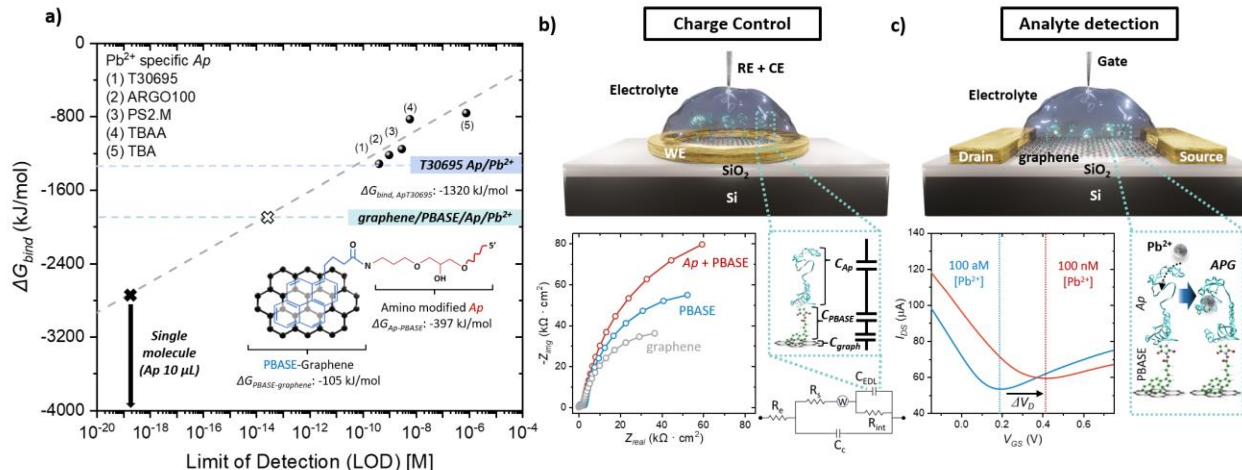

Figure 4. 1 (a) The binding free energy of Guanine-rich *Ap* ($\Delta G_{bind,\,Ap}$), labeled (1), (2), (3), (4) and (5) – see *text,* may be correlated to the limit of detection (LoD), as indicated through the dashed line. We have obtained, through experiment, the *limit* indicated by the white cross, using the T30695 *Ap* optimally linked to the PBASE bound to the graphene surface. A ΔG_{bind} (~ -2740 kJ/mol) is required to reach an LoD of 1 ion/molecule, corresponding to the indicated zeptomolar (zM) concentration. (b) Schematic of the setup of the electrochemical impedance spectroscopy (EIS) measurement – *top,* for monitoring capacitance modulations related to the substrate preparation and analyte detection, configured with reference, counter, and working electrodes (RE, CE, and WE, respectively). A sample Nyquist plot as a function of the sensing graphene surface preparation, PBASE linker addition, and *Ap* functionalization is shown at the *bottom* as well as corresponding EIS circuit model. (c) The measurement of the electrical current (*I*) – voltage (*V*) characteristics for Pb^{2+} detection in a FET, with drain (D), source (S), and gate (G) electrodes - *top*. The shift in the Dirac voltage (ΔV_D) could be used to sensitively detect the *APG* (Ap-Pb^{2+}-G-quadruplex) formed upon binding with Pb^{2+}.

However, in the GFET sensing modality the *Ap* would be connected to the sensing surface, *i.e.,* the graphene, through the PBASE linker. Consequently, the *Ap* – linker – channel surface binding energies must be considered in toto, *i.e.,*

$$\Delta G_{net} = \Delta G_{bind,\,Ap} + \Delta G_{Ap\text{-}PBASE} + \Delta G_{PBASE\text{-}graphene} \tag{1}$$

Here, the $\Delta G_{Ap\,-\,PBASE}$ and $\Delta G_{PBASE\text{-}graphene}$ are the related binding energy values between *Ap* and PBASE – as manifested through the amide bond, and between PBASE and graphene – reckoned through π orbital stacking interactions.[145,146] In the former case, the amide bond is formed when the N-hydroxy succinimide (NHS) ester group of PBASE interacts with the primary

amine group (-NH_2) of the *Ap,* with an estimated bond energy of ~ 400 kJ/mol, as obtained through *ab initio* density functional theory (DFT).[147] For the $\Delta G_{PBASE\text{-}graphene}$, the binding energy of the non-covalent highly ordered π-π stacking interaction of pyrene aromatic ligands with graphene[148] must be considered; associated *ab initio* DFT indicated an estimate of ~ 105 kJ/mol.[149] From Eqn. (1), the ΔG_{net} would be ~ 1825 kJ/mol with projected LoD in the sub-femtomolar (fM) level. The corresponding additions to the $\Delta G_{bind,\ Ap}$ from the $\Delta G_{Ap\text{-}\ PBASE}$ followed by the $\Delta G_{PBASE\text{-}graphene}$ are inserted into **Figure 4.1 (a)** and imply an improved LoD to the level of 10 fM. Hence, it should be possible to achieve such an LoD with properly optimized experimental protocols and procedure.

Such optimization can be achieved in practice by monitoring the successive adhesion of (i) PBASE to the graphene, followed by (ii) *Ap* to the PBASE, and finally the (iii) analyte, say the Pb^{2+} to the *Ap.* We adopted an implementation related to the monitoring of the related change in the charge states due to the adhesion, *e.g.,* through the perspective of electrical capacitance, as may be obtained through electrochemical impedance spectroscopy (EIS): **Figure 4.1(b)**. For instance, it may be expected that the electrical double layer capacitance (C_{EDL}) would differ when measured on a pristine graphene surface as opposed to a surface modified with linkers and *Ap*.[150-152] It is noted that the formation of an EDL would be predicated on the charge difference between the graphene and added moieties *and* the surrounding environment, and incorporates capacitance contributions from the *bare* graphene (C_{graph}), PBASE (C_{PBASE}), and the *Ap* (C_{Ap}) : **Figure 4.1(b).** Given that capacitance changes could, in principle, be monitored at the single electron level[153,154], it may be possible to achieve unprecedented level of sensitivity through monitoring the change in the C_{EDL}. The modulation of the C_{EDL} may then be used to interpret the characteristics of the *Ap* – linker – sensing channel. It was determined for instance, as indicated later, that the C_{EDL} was indeed correlated to the surface coverage of attached PBASE and *Ap* and could be used for monitoring

the charge distribution on the surface leading towards enhanced sensor performance. A measure of the sensitivity could be related to the ratio of the *relative* change in the capacitance, *i.e.,* in terms of $\Delta C_{EDL}/C_{EDL}$, implying that if the sensor synthesis processes were optimized to yield the lowest C_{EDL} following a given protocol, then record sensitivity could indeed be obtained.

Based on the above principles of free energy minimization from a *theoretical* point of view and monitoring capacitance minimization – from an *experimental* point of view, we demonstrate a *new record* and the *lowest possible* LoD of Pb^{2+} detection. The obtained LoD of ~ 7 fM is an order of magnitude better in comparison to a previous report[141] and corresponds to the detection of ~ 40,000 Pb^{2+} ions. Our work lays a basis towards more sensitive as well as specific detection of species and paves a way towards the ultimate detection of a single analyte species.

4.3 Graphene characterization and device preparation

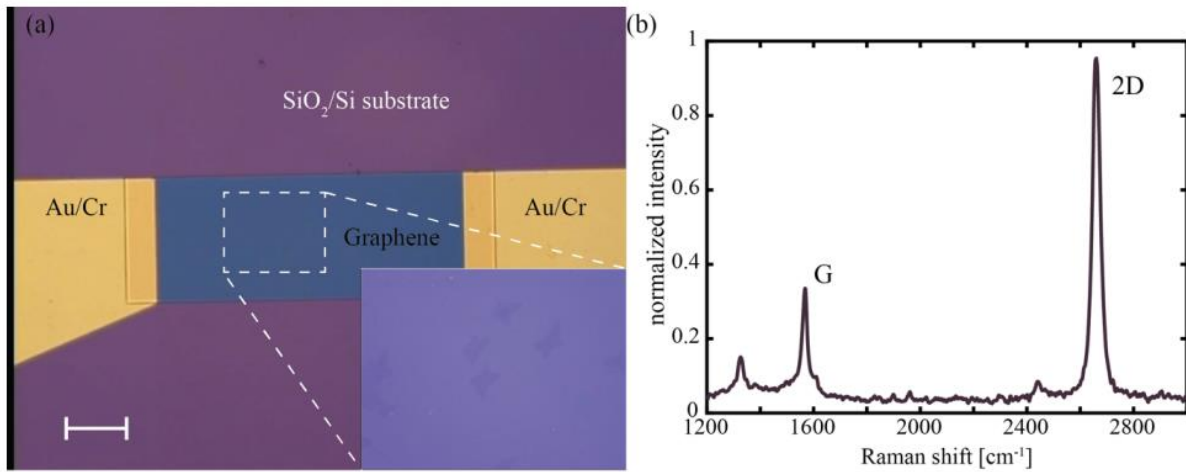

Figure 4. 2 (a) Optical microscopy image of the GFET (scale bar: 100 μm) and the graphene channel on SiO2 substrate (inset). (b) The Raman spectroscopy of graphene/SiO2, the Raman peak intensity is normalized to that of the 2D peak intensity

As indicated previously, the use of the T30695 *Ap* tethered to the PBASE interacting with the graphene provides the *most sensitive* receptor for detecting Pb^{2+}. In accord with previous

procedures from our group[141], the steps for the preparation of the graphene surface will be outlined briefly. Single-layer graphene (SLG) was synthesized through low pressure (300 mTorr) chemical vapor deposition (LPCVD) on Cu foil (25 μm thickness, MTI Corp), through using a mixture of hydrogen (H_2, 15 sccm) and methane (CH_4, 2 sccm) for 2 h. The foil was pre-cleaned by trichloroethylene followed by acetone and isopropyl alcohol (IPA) rinsing and N_2 blow dry. The pre-cleaned Cu foil was folded to ensure stable precursor flow[155], resulting in high-quality large area SLG growth. The Cu foil was annealed for 1 h at 1000 °C, under 85 mTorr, to reduce residual contamination. The LPCVD-grown SLG on Cu was spin-coated (at 3000 rpm for 45 s) by 120 K MW poly (methyl methacrylate) (PMMA) for subsequent wet transfer[156] onto an electrode-patterned SiO_2/Si substrate. Oxygen (O_2) plasma etching was used to remove the SLG on the backside of the Cu foil. Ammonium persulfate (0.1 M) solution was used to etch Cu foil and subsequently rinsed with DI water. The PMMA was dissolved using acetone for 1 h followed by IPA rinse and N2 blow dry. The single layer graphene (SLG) on SiO2/Si substrate was further characterized by optical microscopy and Raman spectroscopy at 532 nm by the Renishaw spectrometer, where $I_{2D}/I_G>2$ (**Figure 4.2**).

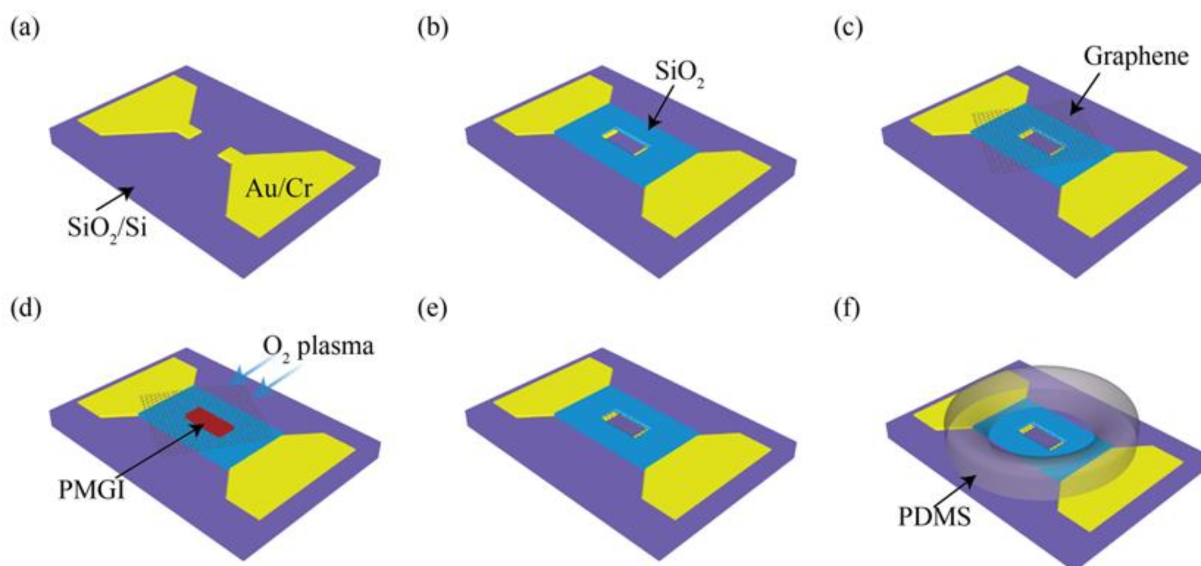

Figure 4. 3 The graphene field effect transistor (GFET) fabrication processes[], include (a) electrode patterning and definition, by photolithography, (b) oxide (SiO2) deposition, (c) Transfer of graphene onto the oxide, (d) definition of the graphene channel through photoresist (PMGI) S-3 masking layers and use of oxygen (O2) plasma to remove graphene outside the channel, (e) FET definition, followed by (f) PDMS mold around the channel to hold the liquid analyte.

The graphene field effect transistor (GFET) was fabricated through photolithographic processes on graphene transferred onto thermal oxide SiO2(300nm)/Si wafers, as schematically shown in **Figure 4.3**. A typical device was configured with a 500 µm × 200 µm channel and contacted through source/drain pads constituted from Au (90 nm)/Cr (10 nm) deposited by sputtering deposition: (a). Subsequently, a 100 nm SiO2 layer was deposited around the channel area to isolate the source/drain pads from the electrolyte, i.e., only 20 µm × 200 µm of the source/drain electrodes were exposed to the analyte solution: (b). The graphene was transferred using PMMA: (c). To define the graphene channel, photolithography using PMGI[157] photoresist was applied to protect the graphene channel, with extraneous graphene removed by Oxygen plasma dry etching: (d). The GFET was further annealed at 200 °C for 2 h under a H_2/N_2 ambient: (e). An analyte reservoir was made using Polydimethylsiloxane (PDMS) to hold the sample liquid

on the graphene channel: (f). The graphene was prepared for *Ap* attachment through first placing 10 μL of PBASE (prepared by mixing 1-Pyrenebutanoic acid: from Anaspec, Inc. with dimethylformamide in the range of 10 nM to 100 mM for 30 minutes at room temperature) *anchoring* molecule/s onto the surface. Subsequently, 10 μL of the T30695 *Ap* (from IDT Technologies, Inc., and prepared in a range of concentration from 10 nM to 100 μM, in deionized water) was incubated onto the PBASE grafted graphene surface. Here, the *Ap* was heated to 90 ^oC for 5 minutes and slowly cooled down to room temperature to induce the biomolecules into an extended conformation.[158] A range of incubation times, *i.e.,* from 8 minutes – 2 hours, at room temperature, was used for experimentation. The amine group of the *Ap* is linked to the ester group of PBASE, through the amide bond. After placing the *Ap* on the GFET surface, ethanolamine (EA) was used to passivate the unlinked left over PBASE. Subsequently, the Pb^{2+} analyte was added to the GFET through use of $Pb(NO_3)_2$ dissolved in DI water, at various concentration levels. Imaging of the graphene surface at all stages was done through atomic force microscopy (AFM, Park Systems, Inc.) in the contact mode.

The schematic of the setup for EIS as well as the sensing FET are indicated in **Figure 4.1 (b)** and **(c),** respectively. The estimation of the C_{EDL}, related to monitoring the charge state at/around the graphene surface, was done through the VersaSTAT 3 (AMETEK, Inc.). Here, the reference/counter electrodes (RE/CE) were connected together and placed in the analyte electrolyte, with the working electrode (WE) placed on one of the adjacent Au electrodes. The EIS measurements were performed with 150 mV bias AC, for non-faradaic probing, over a frequency range of 0.4 Hz to 100 kHz. With respect to the FET in **Figure 4.1(c)**, the modulation of the current between the source and drain (I_{ds}) driven under a small bias voltage (V_{ds}) of 0.2 V, was monitored as a function of the gate voltage (V_g) – voltages from the Keithley 2400 source meter/s. The gate

electrode was placed in the Pb^{2+} incorporated analyte solution, and the gate leakage (I_{gs}) was typically less than ~ 10 nA. A minimum value of I_{ds} was observed during the positive and negative sweep of the V_{gs} (at a typical rate of ~ 30 mV/s) at a particular V_{gs} designated as the Dirac voltage (V_D). The shift in the V_D, *i.e.,* the ΔV_D ($= V_D - V_D^{Initial}$), was used as a metric for the charge state of the surface, as may arise from the functionalization of the graphene surface through PBASE and subsequent *Ap* addition. The *Ap* upon binding Pb^{2+} has been posited to form an *APG*: **Figure 4.1 (c),** the charge modulations from which would be manifested through the I_{ds} changes. Both EIS and *I-V* measurements were carried out at least three times to verify reproducibility of obtained results and for noting the systematic and random errors.

4.4 Analyzing Ap distribution on graphene surface via EIS and AFM

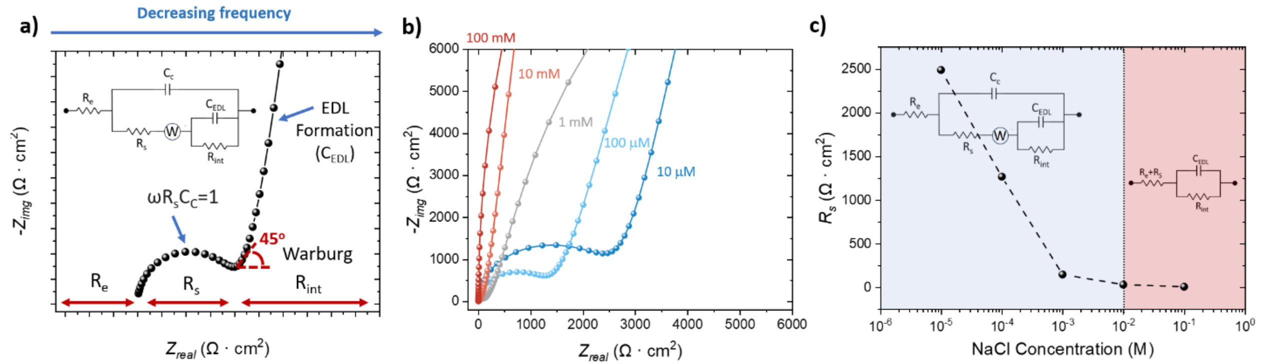

Figure 4. 4 (a) The physical interpretation of the non-faradic EIS circuit model. electrode resistance (R_e), electrolyte resistance (R_s), cable capacitance (C_c), Warburg diffusion impedance (W), interfacial resistance (R_{int}) and electrical double layer capacitance (C_{EDL}) may be obtained, from the plot, as represented in the *inset* equivalent baseline circuit model. (b) The measurements on the GFET aptasensor in NaCl solutions with concentration of 10 µM, 100 µM, 1 mM, 10 mM, and 100 mM. (c) The change of R_s as a function of different NaCl concentration. The inset represents the corresponding EIS circuit model at different NaCl concentrations.

The EIS spectra with (i) graphene, and subsequent (ii) added PBASE, followed by (iii) *Ap* were recorded and the corresponding circuit model, in terms of the constituent electrical capacitances (*C*) and resistances (*R*), is outlined in **Figure 4.4 (a).** It is feasible in practice, to assign several types of *R*-*C* models, and we suggest a comprehensive schema. Here, the background electrode and solution resistance (R_e and R_s, respectively), capacitance from the electrical wires and connections (C_C), and the C_{EDL} along with the interfacial resistance (R_{int}) are indicated. Further, ion diffusion in the electrolyte could contribute to a variable charge storage and a consequent capacitance-like term, denoted as a Warburg element (*W*).[159] An internal resistance (R_{int}) was also introduced to represent dissipative processes across the EDL. We suggest that the introduced model incorporates the possible elements necessary to obtaining a clear understanding of the involved sensor processes and could be extracted from the experimental spectra. The detail physical interpretation of baseline EIS circuit model is shown in **Figure 4.4 (a)** and can be also identified by changing the concentration of the NaCl electrolyte. The diameter of the semicircle appeared at the higher frequencies is particularly the point of interest because it has been the subject of various conflicting interpretation.[160-163] As shown in **Figure 4.4 (b)**, it is evident that the size of the semicircle decreases with an increase in the concentration of NaCl and eventually vanishes when the concentration reaches 10mM. This observation suggests there is a strong correlation between the appearance of semicircle and the conductivity of the electrolyte. Further simplification of the suggested *R*-*C* model is possible in specific situations, *e.g.,* at higher electrolyte concentrations, where a simpler circuit with *only* two resistors (R_e + R_s and R_{int}) along with the C_{EDL} is relevant, *etc.* The R_s extracted from **Figure 4.4 (b)** is illustrated in **Figure 4.4 (c)**. The increase in conductivity of NaCl leads to decrease in size of R_s, shrinking the diameter of semicircle and thereby removing the C_c and Warburg element from model at [NaCl] of ~10^{-2} M.

R_e and R_s can be represented single resistor as $R_s \sim R_e$. The similar circuit model and interpretation have previously reported in recent EIS EDL studies.[160,163]

Based on the hypothesis that the optimal packing would correspond to the minimal value of the C_{EDL} and maximal sensitivity, we conducted two sets of experiments across (i) a range of PBASE concentrations added to the graphene, from 0.1 nM to 100 mM: **Figure 4.5 (a)**, followed by (ii) a range of *Ap* concentrations, from 10 nM to 100 µM, added to the graphene - PBASE moiety: **Figure 4.5 (b)**. Several incubation times for both PBASE and *Ap* were attempted, and an optimized time of 30 minutes was chosen based on AFM-based structural studies, as will be explained later, *i.e.,* in the context of **Figure 4.7.**

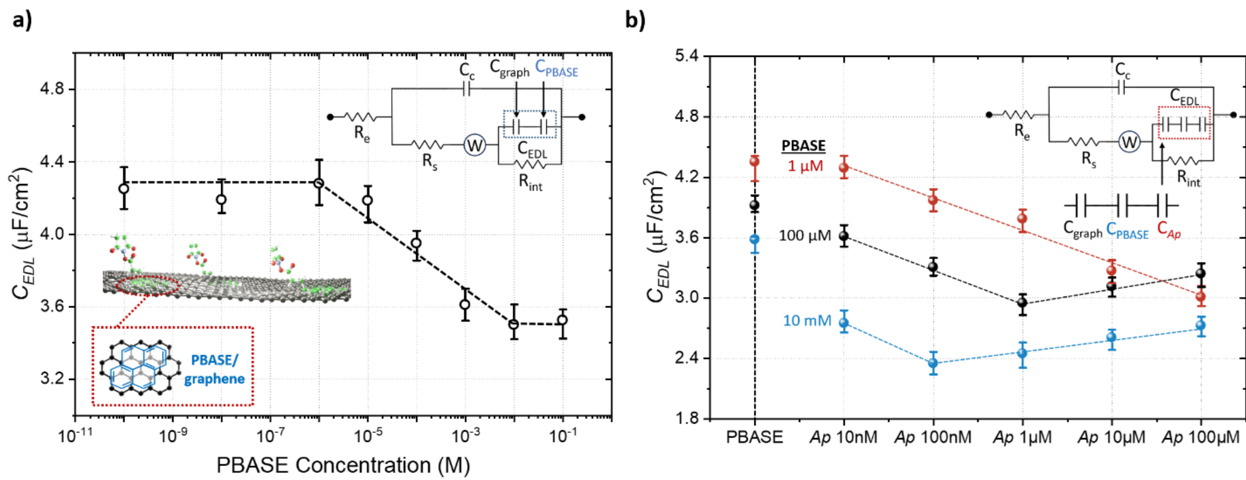

Figure 4. 5 **(a)** The estimated C_{EDL} as a function of the PBASE concentration placed on the graphene surface of the FET. The top *inset* represents the corresponding EIS circuit model and the bottom *inset* indicates a schematic of the pyrene group of the PBASE attachment to the graphene. **(b)** The extracted C_{EDL}, after *Ap* (in the range of 10 nM to 100 µM) was incubated for 30 minutes to cross-link with the PBASE - at specific concentration levels. The *inset* is the relevant equivalent circuit model representing the series addition of the bare graphene capacitance: C_{graph}, *with* the additional capacitance from the added PBASE and *Ap:* C_{PBASE} and C_{Ap}, respectively.

It was observed in the former case, that the estimated C_{EDL} was approximately constant at ~4.3 µF/cm^2, with added PBASE concentrations in the range of 0.1 nM to 1 µM - over four orders

of magnitude. It may be inferred that in this range, that the immobilized PBASE does not have a noticeable effect on the EDL. However, as the PBASE concentration was further increased, from 1 μM to 10 mM, the C_{EDL} decreases to ~3.5 μF/cm^2, with no further changes at larger concentrations. The saturation of the capacitance at low (/high) concentrations could be due to the inadequate (/sufficient) coverage of the graphene surface by the PBASE. A new circuit model was invoked to explain the observed phenomena, where the C_{EDL} at higher PBASE concentration was represented through a series combination of the capacitance arising from the added PBASE, *i.e.*, C_{PBASE} *along* with C_{graph}. At low (/high) PBASE concentration, there would be a high (/low) C_{graph}, and the C_{EDL} would tend to the capacitance related to the PBASE (/graphene). Indeed, the observed value of ~3.5 μF/cm^2 is in accord with the expected value measured on the basal plane of graphene.[164,165] In the range of PBASE concentrations between 1 μM and 10 mM, *both* the C_{PBASE} *along* with C_{graph} needs to be considered (see **Figure 4.6** for more details).

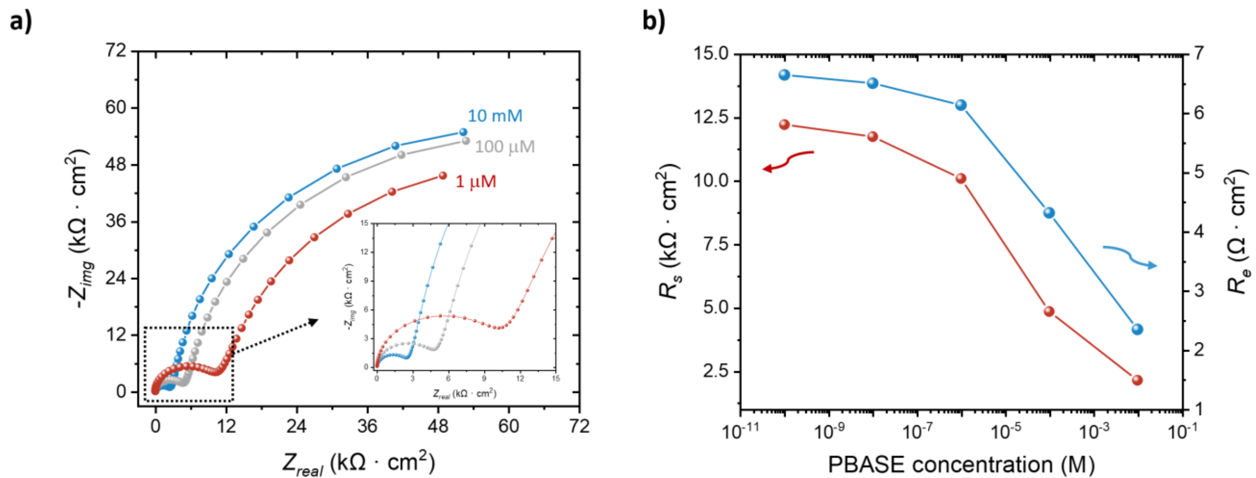

Figure 4. 6 (a) Nyquist plot for the graphene FET immobilized with PBASE concentration of 10 mM, 100 μM, and 1 μM for 30 minutes. The *inset* shows a magnified view of the impedance spectra at high frequency. (b) The variation of the solution resistance: R_s, and the electrode resistance: R_e, with PBASE concentration.

The EIS related Nyquist plot from the graphene FET immobilized with various PBASE concentrations were measured and are shown in **Figure 4.6 (a)**. The extracted R_s and R_e are plotted as a function of the PBASE concentration in **Figure 4.6 (b)**. It was seen that the GFET immobilized with 0.1 nM of PBASE has the largest value of $R_s \sim 12$ kΩ/cm^2, close to that of the DMF solvent (with R_s of 11.4 ~ 18.9 kΩ/cm^2 corresponding to the reported range of 1.6 ~ 2.6 μΩ^{-1} cm^{-1} [166]). Such an aspect suggests that with PBASE concentrations lower than 1 μM, the characteristics are effectively comparable to DMF, and hence may be considered as dilute solutions. However, with increasing PBASE concentration the R_s decreases, *e.g.,* to ~ 2 kΩ/cm^2 at a concentration of 10 mM. A corresponding decrease of the R_e was observed with increasing PBASE concentrations: **Figure 4.6 (b)**. It was previously indicated that the immobilization of PBASE on the graphene surface enhances graphene conductivity, due to (i) enhanced carrier concentration, through doping from PBASE linker constituents[167], and (ii) appearance of new states around the conduction band edge of the graphene due to charge transfer.[168]

We next report on the further modulation of capacitance when the T30695 *Ap* was added to specific amount of PBASE, *i.e.,* 1 μM, 100 μM, and 10mM, placed on the graphene surface. The chosen concentrations correspond to those at which the C_{EDL} tends to that of the C_{PBASE}, C_{graph}, and of an intermediate value, respectively. The consequent measurement of the C_{EDL}, is shown in **Figure 4.5 (b).** Here, two major trends were observed, subsequent to *Ap* addition in the range of 10 nM to 100 μM: (i) a steady decrease in C_{EDL} from ~4.3 μF/cm^2 to ~2.9 μF/cm^2 with a PBASE concentration of 1 μM, (ii) a minimum in the C_{EDL} at a PBASE concentration of 100 μM and 10 mM. Given that the C_{EDL} would be inversely proportional to the effective thickness of the layer related to the influence of the bioreceptors immobilized onto the graphene surface[169], the decline in C_{EDL} in (i) may be attributed to an increasing thickness from the attached *Ap* and serves as an

indicator of the surface coverage. The influence of the added *Ap* on reducing C_{EDL} was then considered through the series addition of another capacitor, *i.e.,* C_{Ap}, to the C_{graph} and C_{PBASE}, as indicated in the *inset* to **Figure 4.5 (b)**. The appearance of the minimum in the C_{EDL} in (ii) could be linked to the surface distribution and coverage of the *Ap* onto the PBASE/graphene. There is, for instance, the likelihood of *Ap* interaction arising from the self-complementary nature of *Ap* sequences[139], through which there would be a deficit (/excess) charge in the presence (/absence) of interaction/s. Given the area of the placed graphene (~0.001 cm^2) and the size of the pyrene group of PBASE (with a carbon-carbon distance ~140 pm[170]), the number of ester groups (with [PBASE] $\geq$ 10 mM) available to bind with the *Ap* may be estimated to be ~ 3×10^{11}, assuming adjacency of the pyrene groups. With *Ap* concentrations of 100 nM, there would be ~ 6×10^{11} *Ap* molecules in 10 µL, providing an adequate number for binding with PBASE. Considering that the T30695 *Ap* is composed of 16 nucleotides and that the persistence length could be ~ 0.8 nm[171], *Ap* aggregation would be expected. Such aspects were sought to be understood by a direct examination and imaging of the graphene surface, *e.g.,* through atomic force microscopy (AFM). **Figure 4.7** indicates the related micrographs for 100 nM *Ap* functionalized graphene surfaces, obtained for three representative times of *Ap* incubation.

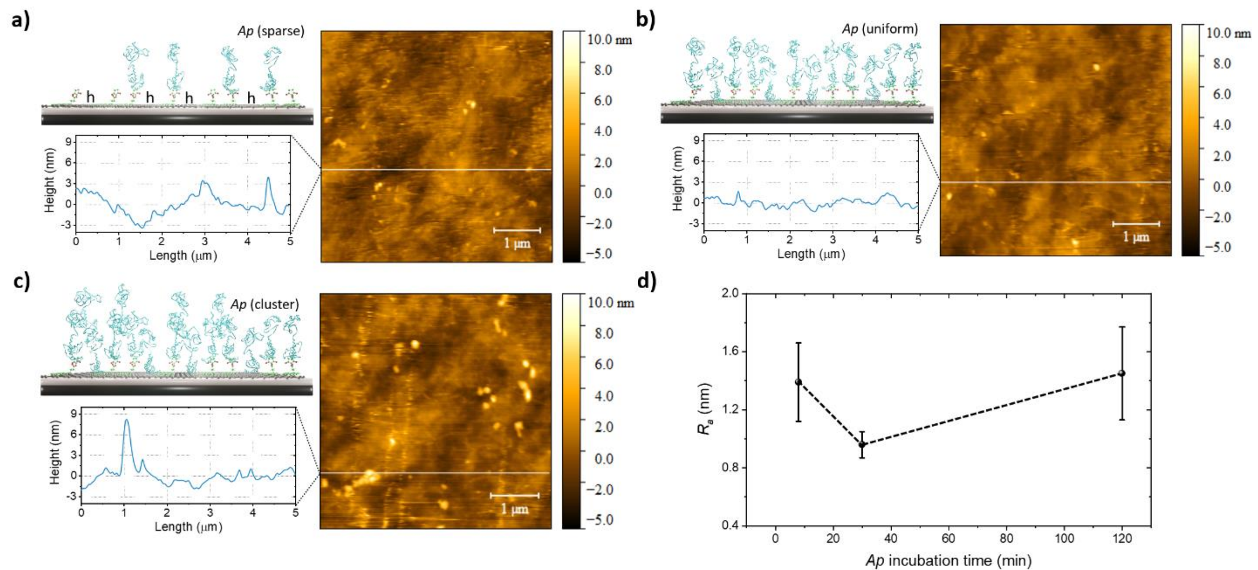

Figure 4. 7 AFM imaging of graphene surface covered with 100 nM *Ap,* after **(a)** 8 minutes, **(b)** 30 minutes, and **(c)** 120 minutes. A schematic of the inferred coverage is indicated on the *left* of each image. In **(a)**, the h represents the PBASE unlinked graphene surface. The height profiles correspond to the line trace shown in the AFM images. **(d)** The *RMS* roughness variation as a function of the *Ap* incubation time, decreases from ~1.4 nm to a minimum of ~ 0.9 nm at ~ 30 min of incubation, following which there is a further increase to ~1.5 nm, at larger incubation time.

A comparison of the graphene surface incubated with *Ap* for three representative times is indicated: **Figure 4.7 (a)**: 8 minutes, **Figure 4.7 (b)**: 30 minutes, and **Figure 4.7 (c)**: 120 minutes. The rationale for the choice of the times was related to the sensitivity of the device as will be explained further, say, with reference to **Figure 4.13**. A more uniform coverage, with a roughness of ~ 0.9 nm, was obtained in the case of 30 minutes of incubation time. In contrast, graphene surfaces incubated with the *Ap* for shorter (/longer) times, *cf.* **Figure 4.7 (a)** and **(c),** exhibit more clustered distribution of the *Ap* with higher surface *RMS* roughness: **Figure 4.7 (d)** (also see **Figure 4.8** and **4.9**).

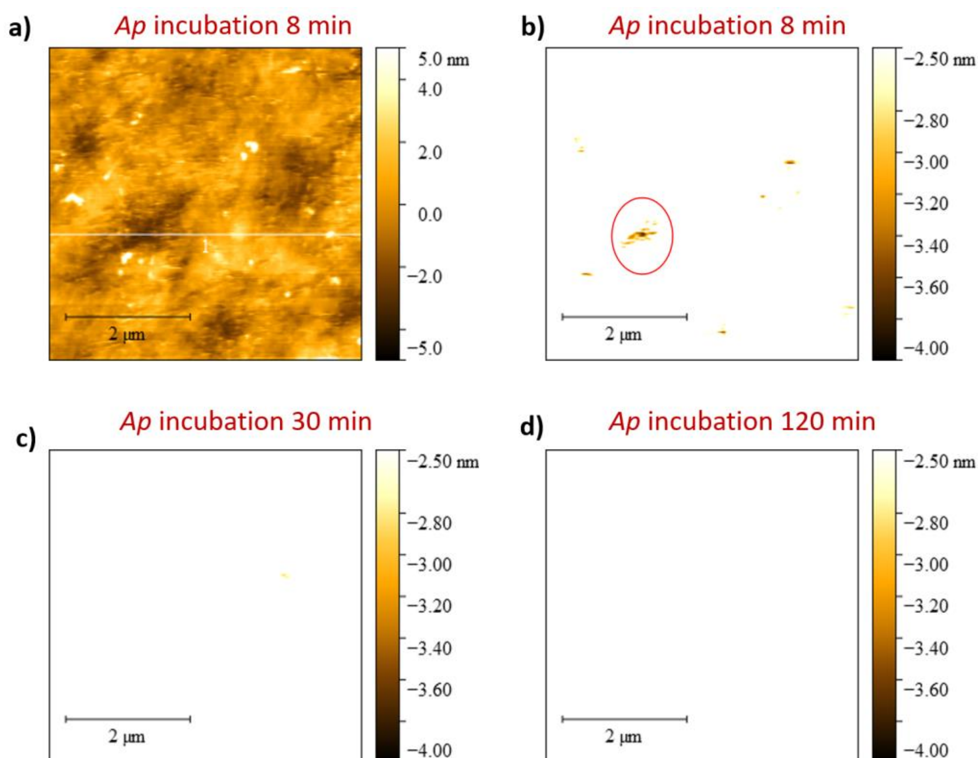

Figure 4. 8 AFM imaging (over a 5 µm x5 µm area) for the (a) 8 minutes *Ap* incubated graphene surface, and (b) corresponding image with height scale in the range of -2.50 nm to -4.00 nm, indicating the possibility of spaces, gaps, or holes on the surface – see **Figure 4.7**, on the surface. The red circle indicates the spot with the possibility of missing PBASE linker/s. (c) and (d) represent the AFM images for an *Ap* incubation of 30 minutes and 120 minutes, respectively.

Detailed AFM imaging was performed on the fully functionalized surfaces, consisting of graphene – PBASE linker- aptamer (*Ap*) ensemble. **Figure 4.8** yields insight related to the distribution of the ensemble on the surface, as a function of *Ap* incubation time. The presence of gaps or unfilled spaces on the surface is seen in **Figure 4.8 (a),** indicating a surface roughness span in the range of – 5 nm (indicating the gaps on the surface) to + 5 nm (indicating the height above the surface)**.** When the scale of measurement is restricted to the range of -2.5 nm to -4.0 nm, the gaps may be better observed as in the red circle of **Figure 4.8 (b),** with an *Ap* incubation time of ~ 8 minutes. The size of the gaps is reduced with increasing incubation time, *i.e.,* at *both* **(c)** 30 minutes, and **(d)** 120 minutes. While the former situation corresponds to optimal coverage, the

latter was considered to be a result of *Ap* agglomeration – see **Figure 4.7 (c)** in the main text. Correspondingly, the root mean square (RMS) roughness, which provides a measure of surface smoothness, is modulated – as indicated in **Figure 4.7 (d)** of the main text, as well as in **Figure 4.9**.

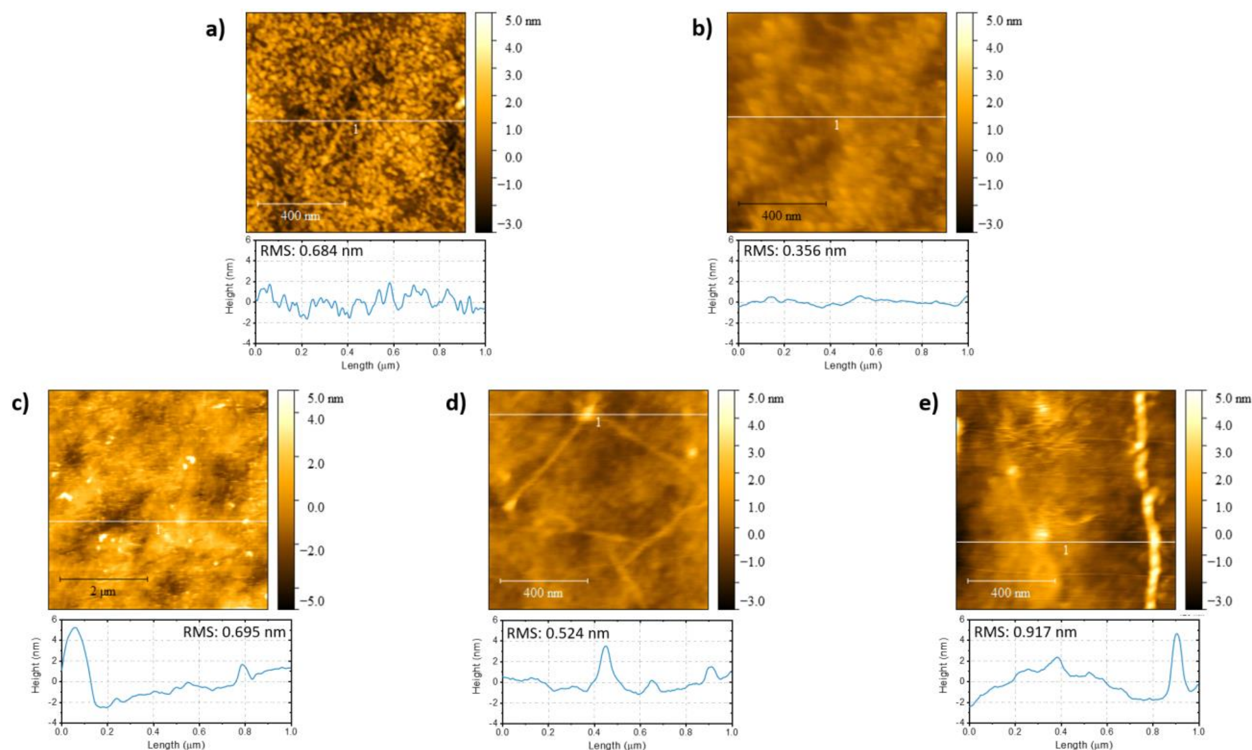

Figure 4. 9 AFM imaging (over a 1 μm x1 μm area) for the (a) bare graphene, (b) PBASE attached graphene, and subsequently with the *Ap* incubated for (c) 8 minutes, (d) 30 minutes, and (e) 120 minutes. The corresponding height profile and RMS roughness are shown.

The higher resolution AFM images, through scans over a 1 μm x1 μm area, of graphene, graphene surface functionalized with PBASE, and *Ap* with various incubation time are shown along with corresponding height profiles and RMS roughness in **Figure 4.9**. The RMS roughness for bare graphene (of ~ 0.68 nm: **Figure 4.9 (a)**) is reduced through the PBASE addition (to ~ 0.36 nm: **Figure 4.9 (b)**). While the lowest roughness (of ~ 0.52 nm) was obtained with subsequent *Ap* incubation time of 30 minutes: **Figure 4.9 (d)**, an increased roughness was seen at smaller

incubation times of 8 minutes (of ~ 0.70 nm: **Figure 4.9 (c)**) as well as at larger incubation times of 120 minutes (of ~ 0.92 nm: **Figure 4.9 (e)**) - due to the non-uniform coverage with gaps or *Ap* clustering, respectively.

Generally, the roughness of the bare graphene is reduced subsequent to PBASE addition.[172,173] It was further observed that *Ap* adsorption occurs preferentially in the vicinity of defects, *e.g.,* grain boundaries[174], wrinkles[175], and vacancies[176], on the graphene, and subsequently spreads across the surface. Such clustering, as manifested through a larger *RMS* roughness, could prompt the steric hindrance and degrade the binding affinity of *Ap*. The minimum in the *net* C_{EDL} of ~ 2.3 μF/cm^2, on the graphene sensing surface, with a PBASE and added *Ap* concentration of 10 mM and 100 nM, respectively: **Figure 4.5 (b)**, may then be interpreted in terms of a balance between high binding affinity of the *Ap* with the Pb^{2+} analyte *vs.* adequate surface density of the linker – *Ap* moiety, while avoiding steric hindrance issues. Based on the hypothesis that the corresponding minimum charge state would be the most sensitive for further analyte charge detection, it was decided to use related concentrations of PBASE and *Ap* as a basis for the detection of Pb^{2+} analytes.

4.5 The LoD dependency of GFET aptasensor with varying Ap incubation condition

4.5.1 The correlation between sensor LoD and higher Ap concentrations (~10 μM)

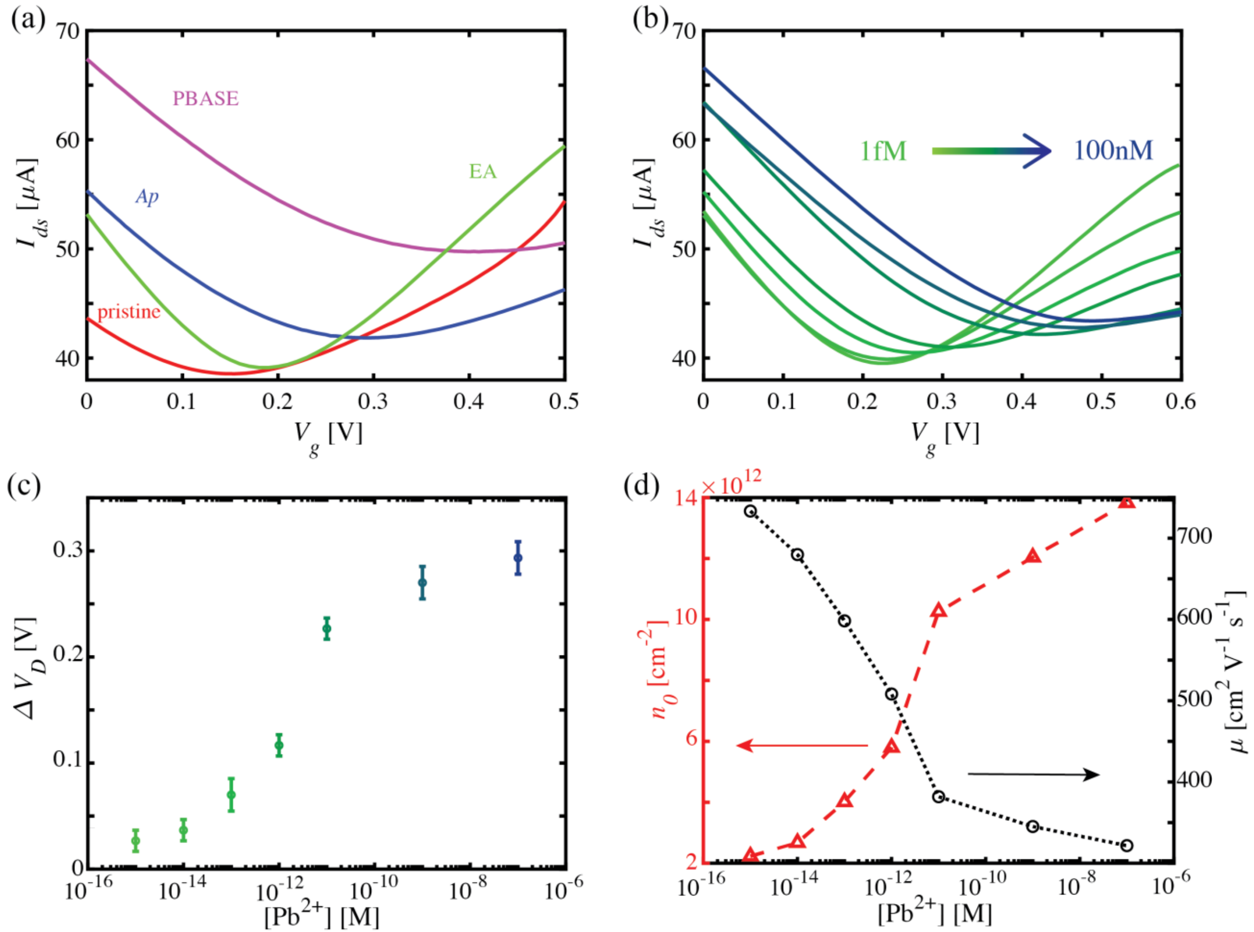

Figure 4. 10 (a) The variation of the I_{ds}-V_g characteristics as a function of the preparation of the GFET for Pb^{2+} detection, comparing (i) pristine graphene, with the characteristic after (ii) attachment of the PBASE linker onto the graphene: purple, followed by (iii) addition of the Ap (10 μM): blue, and then (iv) ethanolamine (EA) addition: green. (b) The change in the I_{ds}-V_g characteristics as a function of Pb^{2+} concentration ([Pb^{2+}]) in the range of 100 aM to 100 nM. The $(V_g)_{min}$ is termed the Dirac voltage (V_D). (c) The change in the V_D with [Pb^{2+}]. (d) The determined charge carrier density n_0: red triangles, and the hole mobility (μ): black open circles, as a function of the estimated [Pb^{2+}].

Given the extreme responsivity of the graphene surface, it is important to first monitor the variation of the V_D arising just from the preparation of the GFET towards Pb^{2+} detection: **Figure 4.10 (a)**. We outline the related modulations of the electrical signals. In sequence, (i) a positive shift of V_D ~ 0.25 V was observed after attaching the PBASE linker onto the graphene, due to the

positive charge transfer from the PBASE to the graphene [177], (ii) the addition of the *Ap* (10 μM, diluted in 1X PBS: phosphate buffered saline solution) induced an opposite/negative V_D shift of ~ - 0.1 V after 30 minutes (min) of incubation[178], and (iii) finally, the EA addition yields again a negative V_D shift of ~ - 0.1 V. The net V_D change, just due to the preparation, is ~ 0.05 V, and sets a baseline for subsequent measurement related to Pb^{2+} addition. The electrical measurements were performed after ~ 10 min of incubation with various concentrations of Pb^{2+} (from 1 fM upwards: **Figure 4.10 (b)**) in aqueous electrolyte background – prepared through mixing $Pb(NO_3)_2$ with DI water. The saturation of the ΔV_D with $[Pb^{2+}] > 1$ nM: **Figure 4.10 (c)**, indicates that the majority of the attached *Ap* has combined with the added Pb^{2+}. Different $[Pb^{2+}]$ yield proportional amounts of the *APG* and could be correlated to the magnitude of the ΔV_D.

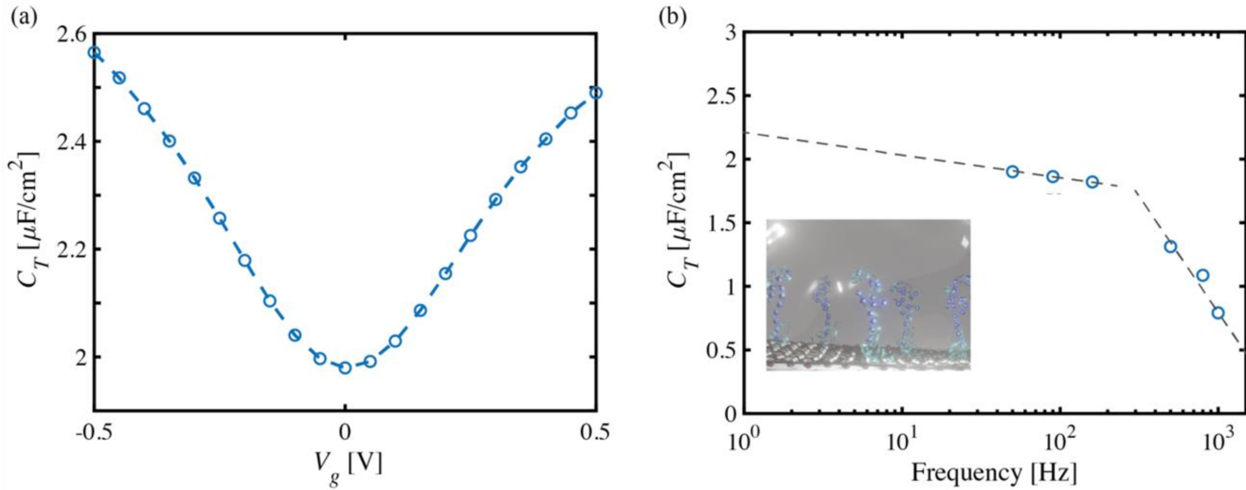

Figure 4. 11 (a) Measured C_T of the GFET as a function of the V_g, (b) The variation of the C_T (at V_g =0) under at AC frequency. The inset represents the deployed capacitance model.

A continuous ΔV_D shift to a more positive value with increasing $[Pb^{2+}]$ was observed: **Figure 4.10 (b)** and **(c).** Such variation was understood in terms of increased *p*-doping of the graphene channel induced *via* the *APG* formation.[51,52,179] We quantify the extent of the related

positive charge (/*hole*) induction, through a [Pb^{2+}] accrual induced carrier density (n_0).[180-182] The n_0 was parameterized through the product of a total capacitance (C_T) and the ΔV_D, through:

$$n_0 = \frac{C_T(\Delta V_D)}{e} \tag{2}$$

The C_T (total capacitance) estimation was done by a Capacitance Bridge (AH 2700, Andeen Hagerling) with an *ac* voltage excitation of ~ 30 mV. The source and drain were grounded and the C_T was measured between the connected source and drain pads of the graphene channel with respect to the gate probe, as a function of the **(a)** V_g, as well as (**b)** *ac* voltage frequency: **Figure. 4.11.** As a function of the V_g (at 80 Hz), a U-shaped capacitance characteristic in **Figure 4.11 (a)** indicates a change of C_Q at different gate induced carrier density (n_g). The C_T as a function of frequency (AC frequency of 50 Hz, 80 Hz, 160 Hz, 500 Hz, 800 Hz and 1 kHz.), see **Figure 4.11** (**b**). A cut-off frequency at ~200 Hz was observed, below which there is a plateauing of the C_T at ~2 μF/cm^2. The carrier (/hole) mobility (μ) in the graphene was then estimated from the following relation [180-182]:

$$R_{channel} = \frac{L/W}{e\mu n_{tot}} = \frac{L/W}{e\mu\sqrt{\left(\frac{C_T}{e}\right)^2 \left(V_g - V_D\right)^2 + {n_0}^2}} = \frac{V_{ds}}{I_{ds}} \tag{3}$$

The $R_{channel}$ is the resistance of the graphene channel, with L (= 500 μm) and W (= 200 μm) as the channel length and width. The $(C_T/e)(V_g\text{-}V_D)=n_g$ is the gate induced carrier density at different V_g with respect to the V_D, and n_{tot} (= $\sqrt{{n_0}^2 + {n_g}^2}$) is a *net* carrier density[181]. The variation of the ΔV_D with [Pb^{2+}] is shown in **Figure 4.10 (c),** and the estimated μ and n_0 is shown in **Figure 4.10 (d).** It was observed that higher [Pb^{2+}] leads to increasing n_0 from ~ 2 x 10^{12} cm^{-2}

to ~ 14 x 10^{12} cm^{-2} and an associated decreased μ from ~740 cm^2/Vs to ~ 320 cm^2/Vs, arising from the additional scattering of the carriers on the graphene surface due to *APG* formation.

To further understand the observed response, we probed the binding affinity of *APG* to the graphene, deploying the Hills-Langmuir model.[183] Here, the ΔV_D is a function of the [Pb^{2+}], through the relation:

$$\Delta V_D = A\frac{[\mathrm{Pb}^{2+}]^h}{K_d^h+[\mathrm{Pb}^{2+}]^h} + B \quad (4)$$

The *A* is the maximum ΔV_D response, presumably obtained when all *Ap* binding sites are occupied. The *B* is a fit to the lowest expected ΔV_D as for a *blank sample* (GFET without [Pb^{2+}]). The K_d is an equilibrium constant (= $\frac{[APG]}{[Ap][\mathrm{Pb}^{2+}]}$) related to the *APG* formation, *i.e.,* with respect to the equilibrium:

$$[Ap] + [\mathrm{Pb}^{2+}] \rightleftharpoons [APG] \quad (5)$$

The square brackets indicate the respective concentrations. When the K_d equals the [Pb^{2+}], the *Ap* on graphene surface is half occupied by Pb^{2+}. The *h* is a coefficient related to the mutual interaction as manifested through a defined *cooperativity* [183]. It was observed that the *A* in **Eqn. (4),** was increased with a longer incubation time, representing higher response, as also seen through an increased ΔV_D with higher [Pb^{2+}]: see *inset* to **Figure 4.12 (a)** - due to a larger [*APG*] on the graphene surface.

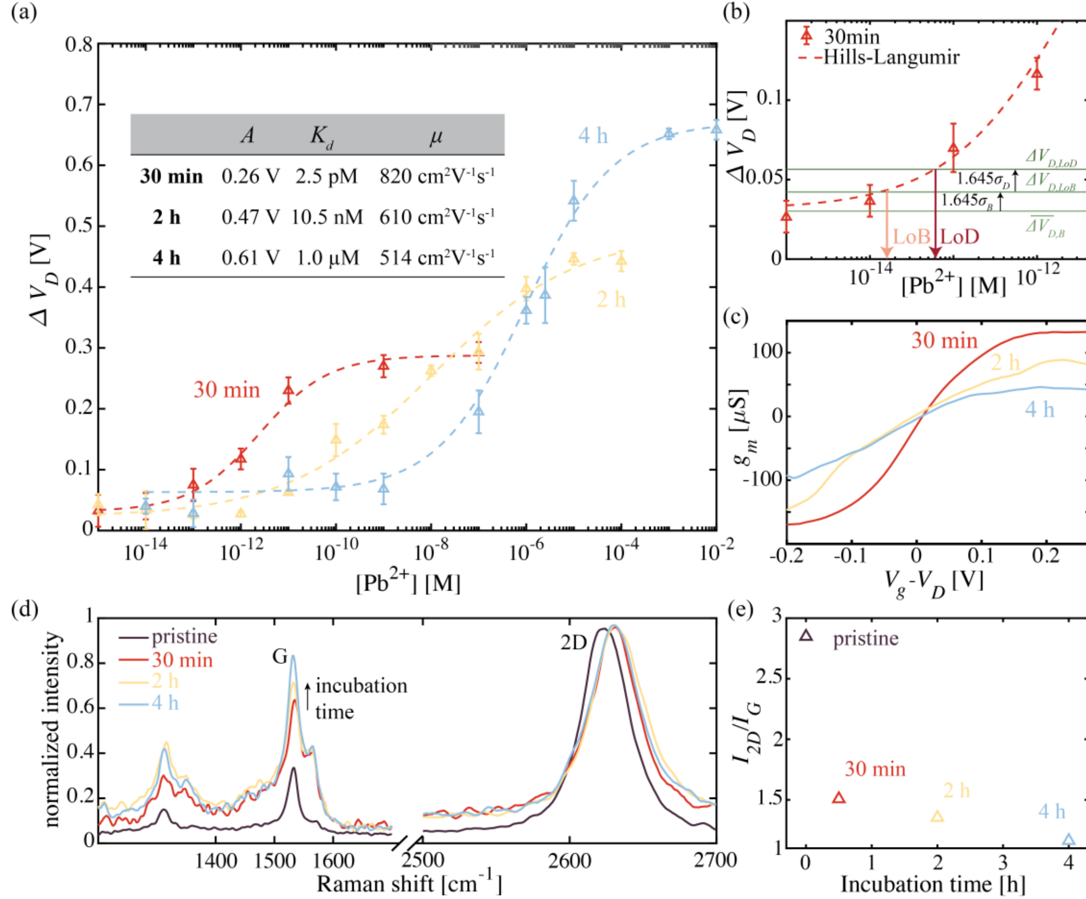

Figure 4. 12 (a) The change in the V_D (ΔV_D) with [Pb^{2+}], as a function of the *Ap* incubation time. A Hills-Langmuir model (with parameters listed in the *inset*) incorporating the influence of the *Ap* incubation times, i.e., at 30 min: red, 2 h: yellow, and 4 h: blue, was used for modeling the associated *Ap* occupation and the binding kinetics. An LoD of ~ 61 fM; ~ 7 pM and ~ 5 nM, were obtained respectively. The error bars were obtained through measurements on four devices tested at each concentration. (b) The determination of the LoB (Limit of Blank) and LoD (Limit of Detection) for [Pb^{2+}] with respect to the (ΔV_D) for 30 min *Ap* incubation. (c) The variation of the transconductance (g_m) with respect to the V_g, for different *Ap* incubation times. (d) The Raman spectrum (normalized to maximum intensity) of the surface of *pristine* graphene compared to that on the graphene surface subsequent to 30 mins, 2 h, and 4 h of *Ap* incubation. The shift of the 2D peak of graphene with increased *Ap* addition shifted to higher wavenumber indicative of *p*-type doping. The intensity of the *G* band (I_G) and *D* band (I_D) also increased with *Ap* incubation due to the doping (e). The ratio between 2D band intensity (I_{2D}) and I_G steadily decreased with longer *Ap* incubation time.

The fit value of *h* for all incubation times was less than 1, indicating *negative* cooperativity arising from (i) the increasingly impeded binding of the *Ap* to the Pb^{2+}, due to proximate *APG* formation, as well as (ii) increased Pb^{2+} repulsion by induced positive charge carrier density from

the *APG*.[184] At higher *immobilized* [*Ap*] on graphene, induced through longer incubation time, the n_0 increases as more charges from the *Ap* are involved. As seen in the *inset* to **Figure 4.12 (a)**, the *h* was reduced from 0.59 to 0.47 with increased incubation time – from ~ 30 mins to ~ 4 h.

The plots of ΔV_D *vs* Pb^{2+} concentration: **Figure 4.12 (a)**, indicate the necessity for considering the LoD and sensor response. A limit of blank (LoB) and an LoD, as a function of *Ap* incubation time, was estimated through the relations [185], also see **Figure 4.12 (b).**

$$\begin{aligned} \overline{\Delta V_{D,B}} + 1.645\sigma_B &= \Delta V_{D,LoB} \leftrightarrow LoB \\ \Delta V_{D,LoB} + 1.645\sigma_D &= \Delta V_{D,LoD} \leftrightarrow LoD \end{aligned} \tag{6}$$

Here, the $\overline{\Delta V_{D,B}}$ and σ_B represents the average and standard deviation of the ΔV_D measurements of GFET on *blank* samples, *i.e.,* with no Pb^{2+} analyte *and* only with deionized water. The aspect that 90% of the measurements would be accounted for is indicated through the $1.645\sigma_B$ value correspondent to a standard normal distribution.[185] For example, with 30 mins *Ap* incubation, we obtained, from the fits in **Figure 4.12(a)**, that $\overline{\Delta V_{D,B}}$ = 0.030 V and σ_B of 0.0073 V. The determined LoB is 16.2 fM - corresponding to the $\Delta V_{D,LoB}$ = 0.042 V. Subsequently, the LoD was determined from the σ_D (= 0.0085 V) per the standard deviation of responses relative to the lowest [Pb^{2+}] detectable (~ 1 fM). With an estimated $\Delta V_{D,LoD}$ of 0.057 V, the LoD was estimated at 61 fM.

Table 4. 1 The determined Limit of Detection (LoD) as a function of the Ap incubation time

Incubation time	$\overline{\Delta V_{D,B}}$	σ_B	$\Delta V_{D,LoB}$	**LoB**	σ_D	$\Delta V_{D,LoD}$	**LoD**
30 min	0.030 V	0.0073 V	0.042 V	16.2 fM	0.0085 V	0.057 V	61.1 fM
2 h	0.022 V	0.0168 V	0.050 V	0.6 pM	0.0150 V	0.074 V	7.3 pM
4 h	0.063 V	0.0139 V	0.086 V	0.9 nM	0.0163 V	0.113 V	5.5 nM

Similarly, the LoB and the LoD was determined for the measurements on the GFET with 2 h, and 4 h of *Ap* incubation time (**Table 4.1**), and correlated to a K_d of 10.5 nM and 1.0 µM, respectively. The change in the *immobilized* [*Ap*] – through the K_d - from pM to µM, indicates an effective increase in the interaction of the *Ap* with the PBASE on graphene, presumably due to diffusional limitations.

A higher LoD with longer *Ap* incubation time, *i.e.,* larger *immobilized* [*Ap*], could be attributed to a decrease in μ, and correlated to the FET device transconductance[186]: $g_m = \partial I_{ds}/\partial V_g$ (at a given V_{ds}). For example, with 30 mins, 2 h and 4 h incubation at different V_g: **Figure 4.12 (c)**, we observed a higher g_m (with a maximum ~ 130 µS) in the case of 30 min, while the maximum g_m reduces for 2 h and 4 h incubation (with a maximum ~ 90 µS and ~ 50 µS, respectively). The μ obtained through Eqn. (3), yielded a lower (/higher) value of 514 (/820) cm^2/Vs with *Ap* incubation time of 4 (/0.5) h, respectively. The decrease in μ may be associated with an increased n_0 at higher *immobilized* [*Ap*]. Since maximal sensing response may be reached when GFET is operated at maximal g_m [187187], a higher μ with a higher g_m would be critical in optimizing the LoD.

Further investigation of carrier doping was done through Raman spectroscopy (at 532 nm, Renishaw inVia) on the *pristine* graphene and then on graphene *with* the immobilized *Ap* at different incubation times (30 min, 2 h, and 4 h): **Figure 4.12 (d)**. It was observed that the 2D peak of graphene with the *Ap* shifted to higher wavenumber (from ~ 2660 cm^{-1} to ~ 2667 cm^{-1}), indicative of hole doping [188,189]. The intensity of the *G* band (I_G) and *D* band (I_D) also increased

with *Ap* incubation as related to an increased n_0 [190,191]. The ratio between 2D band intensity (I_{2D}) and I_G decreases from ~ 2.9 to ~ 1.5 with the addition of the *Ap* as well as longer incubation time: **Figure 4.12 (e)**.

4.5.2 The correlation between sensor LoD and optimized Ap concentrations (~100 nM)

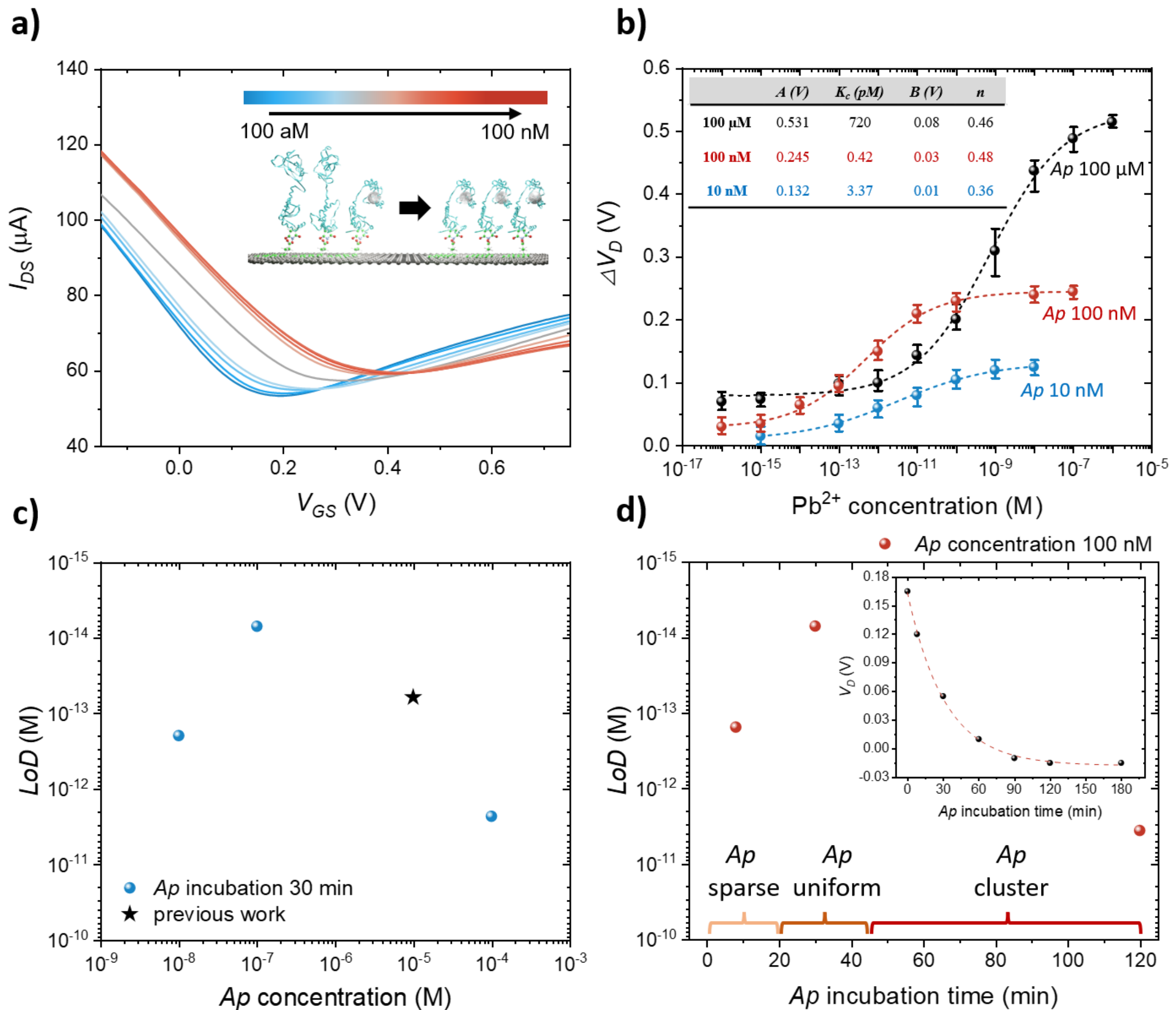

Figure 4. 13 (a) The I_{ds}-V_g characteristics as a function of the added Pb^{2+}, *i.e.,* the [Pb^{2+}], in the range of 100 aM to 100 nM under a fixed *Ap* addition of 100 nM. (b) The change in the Dirac voltage: ΔV_D, as a function of the [Pb^{2+}] with various *Ap* additions, all incubated for 30 minutes; the measured data were fit to the Hill-Langmuir model, as represented through the dashed line/s. The *inset* represents the fitting parameters related to the Hills - Langmuir model. (c) The estimated LoD as a function of the added *Ap* concentration, at a fixed incubation time of 30 minutes. (d) the *Ap* incubation time, at a fixed concentration of 100 nM. The *inset* is the recorded variation of the V_D, at an *Ap* concentration of 100 nM, plotted as a function of the incubation time.

The details related to the results of the detection of the amount of Pb^{2+}, *i.e.,* the [Pb^{2+}], at the optimized PBASE and *Ap* concentrations of 10 mM and 100 nM, respectively are indicated in **Figure 4.13**. We first indicate, in **Figure 4.13 (a),** the recorded changes in the I_{ds}-V_g characteristics from the addition of Pb^{2+} (indicated in the top *inset* in the range of 100 aM to 100 nM) under such fixed PBASE and *Ap* concentrations. An increase in the V_D was observed due to Pb^{2+} addition and consequent *APG* (*Ap*-Pb^{2+}-G-quadruplex) formation. In this context, it was indicated that the *APG* leads to a conformational variation favoring the negatively charged *Ap* to be closer to the GFET surface, subsequently inducing positive charge carriers (/holes: h^+) into the graphene channel of the FET.[141,148,149]

The change in the V_D, *i.e.,* the ΔV_D, as a function of the [Pb^{2+}] is plotted in **Figure 4.13 (b),** at the optimal *Ap* concentration of 100 nM as well as at 10 nM and 100 μM, for comparison. For understanding the related variation, the binding kinetics between the Pb^{2+} and the *Ap* was considered through a fit of the ΔV_D variation through a Hill-Langmuir (H-L) model[183], of the form:

$$\Delta V_D = A\frac{[Pb^{2+}]^n}{K_c^n+[Pb^{2+}]^n} + B \tag{7}$$

Here, *A* is the maximum response obtained when all the *Ap*-binding sites are fully occupied, K_c is an equilibrium constant related to *APG* formation from interaction between the *Ap* and the Pb^{2+}, *n* is the Hills coefficient related to the cooperativity of binding interaction[183], and *B* is a parameter related to the lowest expected ΔV_D for a *blank* sample, *i.e.,* analyte in the absence of Pb^{2+}. We carefully estimated the metrics for sensor sensitivity, such as the limit of blank (LoB) and LoD based on the following relations:[185]

$$\Delta V_{D,Blank} + 1.645\sigma_{Blank} = \Delta V_{D,LoB} \leftrightarrow LoB$$

$$\Delta V_{D,LoB} + 1.645\sigma_D = \Delta V_{D,LoD} \leftrightarrow LoD \tag{8}$$

Here, $\Delta V_{D,Blank}$ and σ_{Blank} indicate the average and standard deviation of ΔV_D measured through the FET on *blank* samples, respectively and σ_D is the standard deviation of the response measured when the lowest detectable [Pb^{2+}], *i.e.,* ~100 aM, as in **Figure 4.13 (a).** Consequently, an LoD of ~ 7 fM was estimated when the FET was functionalized with an *Ap* concentration of 100 nM. The sensor response approaches saturation at $[Pb]^{2+} \geq 100$ nM, suggesting that most of the added Pb^{2+} could be now bound to the available *Ap* sites – indicating an *optimized state of sensing*. There is now limited availability of the binding sites for the Pb^{2+} onto the *Ap*. The fitting parameters used for the estimation of the LoB and LoD are indicated in **Table 4.2** as well as in **Figure 4.13 (b)** *inset*.

Table 4. 2 The estimated LoB (Limit of Blank) and LoD (Limit of Detection) as a function of added *Ap* concentration, with the *Ap* incubated for 30 minutes.

***Ap* concentration**	$\overline{\Delta V_{D,B}}$	σ_B	$\Delta V_{D,LoB}$	**LoB**	σ_D	$\Delta V_{D,LoD}$	**LoD**
10 nM	0.012 V	0.0061 V	0.022 V	11 fM	0.012 V	0.041 V	200 fM
100 nM	0.028 V	0.0055 V	0.037 V	0.73 fM	0.010 V	0.054 V	7.0 fM
100 µM	0.079 V	0.0063 V	0.089 V	0.21 pM	0.012 V	0.11 V	2.3 pM

The change of LoD as a function of the added *Ap* concentration is indicated in **Figure 4.13 (c)**. The remarkable aspect is that the LoD corresponds to the *lowest possible value*, per the theoretical arguments indicated in **Figure 4.1 (a).** At alternate *Ap* concentrations, say of 10 nM and 10 µM, the LoD is much larger at ~200 fM and ~ 61 fM, respectively. Further, the kinetic aspects related to achieving the minimum possible LoD were investigated through changing *Ap* incubation time at optimized *Ap* concentration of 100 nM. It was found, for instance, that the magnitude of V_D diminishes over time prior to reaching a constant value (see *inset* to **Figure 4.13 (d)**). Consequently, three distinct times, *i.e.,* 8 minutes, 30 minutes, and 120 minutes, were chosen

as representative, conforming to sparse, uniform, and clustered distribution of the *Ap* on the graphene surface, respectively. The change of LoD as a function of varying incubation time: **Figure 4.13 (d)**, was estimated from the H-L model, and it was observed that the LoD was related to the incubation time, with a minimal value achieved at ~ 30 minutes while *Ap* incubation time of 8, and 120 minutes yields LoD of ~ 150 fM and 4.0 pM, respectively (*see* **Figure 4.14** and **Table 4.3**).

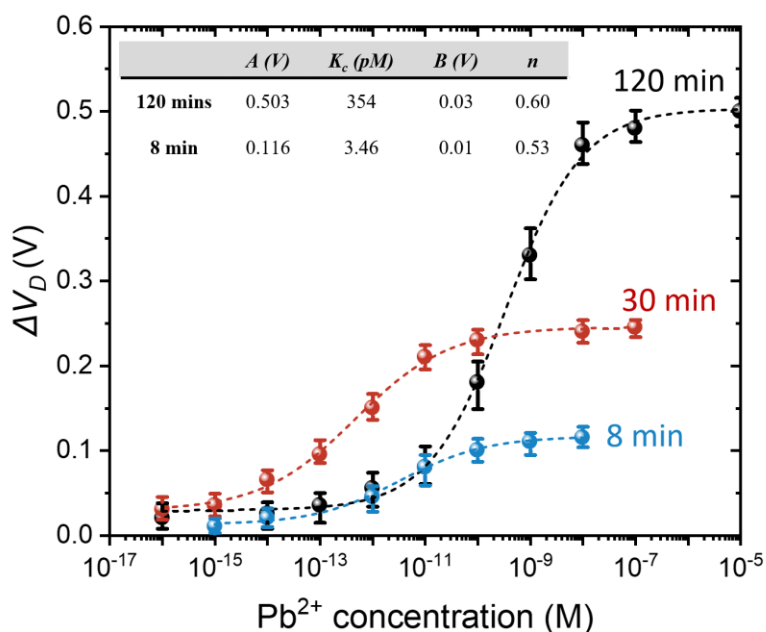

Figure 4. 14 The variation of DV_D, as a function of [Pb^{2+}] at various *Ap* incubation times, with the data fit to the Hill-Langmuir model (dashed line).

Table 4. 3 Calculated LoB and LoD as a function of the *Ap* incubation time, with *Ap* concentration of 100 nM.

***Ap* incubation time**	$\overline{\Delta V}_{D,B}$	σ_B	$\Delta V_{D,LoB}$	**LoB**	σ_D	$\Delta V_{D,LoD}$	**LoD**
8 min	0.012	0.0033	0.017	14 fM	0.0069	0.028	150 fM
120 min	0.029	0.0053	0.038	490 fM	0.012	0.058	4.0 pM

Such a time may be correlated to the uniform coverage of the PBASE linker – *Ap* moiety, as indicated previously through **Figure 4.8 (b)**. At smaller (/larger) times, inadequate (/excess) *Ap* is placed onto the graphene surface – both cases yielding lower likelihood of Pb^{2+} ions in the analyte interacting and binding with the *Ap* linked to the sensing channel. Indeed, with increased incubation time, *Ap* crowding could lead to steric hindrance degrading the binding efficiency.

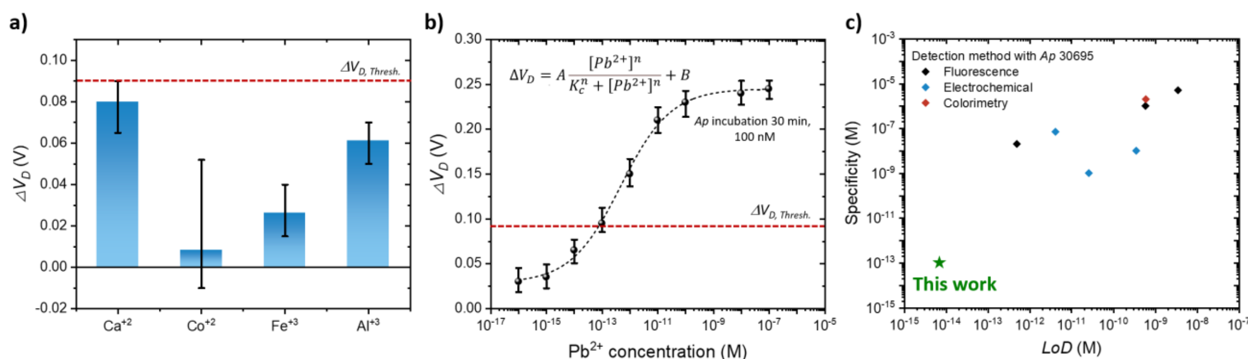

Figure 4. 15 (a) The ΔV_D measured from 100 nM of ions, *e.g.*, Ca^{2+}, Co^{2+}, Fe^{3+}, and Al^{3+}, that may confound the detection of the chosen Pb^{2+} analyte. The threshold ΔV_D ($\Delta V_{D,\ Thresh.}$) represents the lower ΔV_D limit of the GFET aptasensor that can distinctly identify the presence of Pb^{2+} (b) $\Delta V_{D,\ Thresh.}$ Overlaid on the variation of ΔV_D as a function of [Pb^{2+}], fitted with the H-L model in *inset*. The optimized GFET aptasensor can *specifically* discriminate between Pb^{2+} and other ions, when the electrolyte concentration ≥ 100 fM. (c) The comparison of LoD and corresponding specificity reported from Pb^{2+} specific biosensor with T30695 *Ap*.

Concomitant with the record low LoD, the specificity of the optimized sensor towards Pb^{2+}*over* other ions that may be present in typical Pb^{2+} containing solutions[192-194] , *e.g.,* Ca^{2+}, Co^{2+}, Fe^{+3}, and Al^{3+}, was evaluated. Here, the ΔV_D obtained by adding alternate ion-containing nitrates, over a range of concentrations, was observed. A threshold ΔV_D of ~ 0.1 V (= $\Delta V_{D,\ Thresh}$) was obtained with ~ 100 nM of Ca^{2+} ions: **Figure 4.15 (a)**, with smaller ΔV_D for other ions. Through superposing the $\Delta V_{D,\ Thresh.}$ value over the H-L plot, as in **Figure 4.15 (b)**, it was inferred that the chosen T30695 *Ap* would not be able to *specifically* discriminate between Pb^{2+} at the 100

fM level with Ca^{2+} ions simultaneously present at the 100 nM level, at the chosen $\Delta V_{D,\ Thresh}$. The obtained specificity is several orders of magnitude better compared to previous reports, as indicated in **Figure 4.15 (c)**, and attributed to (i) proper choice of the *Ap,* along with (ii) enhanced $\Delta G_{bind,Ap}$ and ΔG_{net}, as discussed in the context of Eqn. (1) and **Figure 4.1 (a)**. Further enhancement in specificity could be obtained through improved $\Delta G_{bind,Ap}$ by *Ap* design[195-197], *e.g.,* through reducing the stability of G-quadruplex formation by other ions.[198-201]

Our work has achieved the *best possible* sensitivity, consistent with thermodynamic predictions, for the detection of a specific analyte, such as the Pb^{2+}. It has been demonstrated that the optimal selection of an analyte specific *Ap* – with the highest binding energy, coupled with its organized placement onto the linker-graphene moiety, is critical. Through seminal measurements of the electrical double layer capacitance (C_{EDL}) and associated modeling, it was shown that achieving a minimum C_{EDL} is integral to the highest sensitivity and provides a metric for optimizing biosensor performance for *any* analyte. The maximization of the charge sensing modality from the analyte while reducing parasitic electrical contributions is consequently achieved. The proof of success of proper *Ap* selection as well as C_{EDL} minimum monitoring is the *record* LoD of ~ 7 fM, coupled with unprecedented sensitivity of ~ 100 nM - *both* orders of magnitude better compared to extant reports in literature. The kinetic considerations related to biomolecule sensing were investigated and it was concluded that the incubation time may be considered an appropriate parameter – the value of which may be inferred through both atomic force microscopy as well as through the current-voltage variation in the FET. Future work should focus on probing the influence of the inevitable intrinsic as well as extrinsic defects in the sensing layer of the FET on the linker-analyte interface, through related electrical as well as structural characterization, on modulating the sensor performance.

4.6 Acknowledgement

Chapter 4, in full, is a reprint of the material as it appears in Lee, Alex, and Prabhakar Bandaru. "Femtomolar Level-Specific Detection of Lead Ions in Aqueous Environments, Using Aptamer-Derivatized Graphene Field-effect Transistors." *ACS Appl. Nano Mater. 2023, 6, 3, 2228-2235*, and "Towards the ultimate limit of analyte detection, in graphene based field-effect transistors". The dissertation author was the primary investigator and author of this paper.

Conclusion and Future Work

5.1 Summary

In this presented thesis research, we have investigated both electrical and sensing application of the oxide and graphene transistors, respectively. The development of high-performance *p*-type oxide semiconductors will help to resolve the current challenges faced in unipolar application of oxide semiconductor and could also open up the new application in ambipolar-TFT based CMOS inverters that can be used for developing a novel logic circuit. For display TFT applications, high performance *p*-channel oxide-TFT could potentially have more advantages in comparison to the *p*-channel LTPS-TFT (*e.g.* low-cost of production due to avoiding utilization of excimer laser) that is used for state-of-arts display TFT. The development of high-performance *p*-type oxide transistor requires the comprehensive study of defect termination methods to suppress the high subgap defects, which hinder the device modulation and make device to exhibit poor performance. The hydrogen annealing effectively terminated the V_o that contributed to the high subgap defects in *p*-type oxide SnO, improving the *p*-channel device performance as well as opening a new opportunity for ambipolar device applications.

For Pb^{2+} detection, it is expected that the development of GFET sensor could solve the issues regarded to the high-cost and non-specific binding involved in the conventional methods of the Pb^{2+} detection (*e.g.* ICP-MS) and commercially available Pb^{2+} detecting home-kits, respectively. The theoretical limit of LoD in our proposed GFET aptasensor based on the thermodynamics involved in the *Ap*–linker–channel material was explored. The proper optimization of the sensor interface (*e.g. Ap* concentrations and the incubation time) achieved the record LoD and specificity in femtomolar range, matching to our proposed thermodynamic

prediction based on the interaction among *Ap*–linker–channel material. In addition, the future approaches needed to reach the ultimate single molecule detection is discussed.

The summary of the presented dissertation on developing oxide semiconductor and graphene transistor for electrical and sensing application can be listed as follow:

In Chapter 2. *p*-channel SnO-TFT was developed by PLD and NH_3 hydrogen annealing. Thermal annealing in hydrogen ambient using a pure NH_3 at 360 °C offers good TFT characteristics with the saturation mobilities of ∼1.4−1.8 $cm^2\ V^{-1}s^{-1}$ and an on-to-off current ratio of $\sim 10^5$ because of the hydrogen termination of the subgap hole trap originating from V_o. Computational device and material analysis revealed that TFT operation is significantly influenced by a near-VB donor-like defect, primarily originating from an V_o. Hydrogen can effectively terminate the V_o by forming Sn−H bonds. Although the current device performance is not yet satisfactory and relatively behind the performance of a-IGZO *n*-channel TFTs, a complementary inverter consisting of *p*-channel SnO and *n*-channel a-IGZO TFTs demonstrated a maximum voltage gain of about 50. This achievement marks an important advancement toward the development of cost-effective next-generation oxide electronics.

In Chapter 3, ambipolar SnO-TFT was developed by controlling the back-channel subgap defects in SnO. The understanding of device operation mode in SnO is crucial to both improving the device performance and expanding the application of oxide semiconductor. It was found that back-channel subgap defects that involve deep donor-like and deep acceptor-like states control the device operation modes of SnO-TFT. High-density defects remove the ambipolarity from SnO-TFT and make the device to only operate in *p*-channel mode. ALD Al_2O_3 passivation effectively reduces these defects and produces good ambipolar SnO-TFTs with mobility of ~ 1.2 $cm^2\ V^{-1}\ s^{-1}$. and *n*-channel mobility of ~ 0.03 $cm^2\ V^{-1}\ s^{-1}$, respectively. The complementary-like inverter is

fabricated using two identical ambipolar SnO-TFTs and exhibits the voltage gain of ~ 64.1 and ~ 48.8 for the first and third quadrants, respectively. The presented study gives insight into the potential usage of oxide semiconductors in novel ambipolar-TFT based CMOS inverters.

In Chapter 4, a highly sensitive and specific Pb^{2+} detecting GFET aptasensor was designed and developed by considering the kinetic characteristics of the graphene FET surface – PBASE linker – *Ap* bioreceptor. The binding energy between the 1) channel surface and linker 2) linker and bioreceptor, and 3) bioreceptor and target analyte was considered for the thermodynamic prediction for sensor performance. The sensitivity was probed in terms of optimal packing of the ensemble, through a minimal charge state/capacitance point of view (EIS) and atomic force microscopy (AFM). The effect of the optimization of *Ap* distribution on graphene surface was explored by determining LoD obtained from Hills model fit of the measurement of the electrical current (I) – voltage (V) characteristics. I-V measurement indicated that the higher *Ap* incubation time and concentration will lead to the degradation of the binding affinity of *Ap* toward the analyte due to the steric hinderance as observed from EIS and AFM. Through the fine tuning of the linker and receptor interaction with the sensing surface, a record limit of detection (~7 fm) as well as specificity (~100 fm) in the femtomolar range and in excellent accord with thermodynamic prediction, was observed. Our presented work provides a new perspective in advancing biosensor technology, aiming for the ultimate goal of single molecule detection.

5.2 Future Work

5.2.1. Nanosheet p-type oxide semiconductor and optimization of SnO-TFT (Ch.2 and Ch.3)

The channel thickness of the SnO in the presented studies (Chapter 2 and 3) is in the range of 7~ 14 nm because SnO is deposited by the conventional physical vapor deposition (PVD) method *e.g.* PLD. Utilizing PVD method typically leading to deposition of electrically inactive incubation layer with a few nm thicknesses due to the nature of the three-dimensional island growth. To grow the ultrathin oxide material, a new strategy such as a liquid-metal printing method could be used to fabricate the SnO-TFT and oxide-TFT based CMOS inverter circuit with thickness of SnO thin film ~ 1 nm. Several studies have successfully synthesized atomically thin metal oxide film *e.g.* Ga_2O_3, HfO_2, and Gd_2O_3.[202] A liquid-metal printing method is a cost and energy-efficient method that could potentially extend its usage to large-scale electronics depending on the size of liquid-metal area.

The optimization of SnO-TFT could be done by adapting double-gate structure and high *k* dielectric. With sufficiently thin channel and gate oxide layers, the strong coupling of the biases applied to the two gates will allow efficient modulation of the channel potential in comparison to single gate structure[203], leading to improvement in device parameter such as *s*-value. The device optimization can be integrated with development of nanosheet thin film to advance the current performance of SnO-TFT to the next level.

5.2.2. Developing the sensor toward single molecule analyte detection (Ch.4)

The presented research suggested how the role of thermodynamic involved in channel – linker – bioreceptor could be used to determine the sensing sensitivity and specificity. Therefore, enhancing the ΔG_{net} is the key to improve the performance of the sensor LoD approach toward the single molecule analyte detection. The presented study revealed that the estimated ΔG_{net} required to reach single molecule detection is ~ 2740 kJ/mol, which require the improvement of ΔG_{net} components $\Delta G_{bind, Ap}$, $\Delta G_{Ap\text{-}PBASE}$, and $\Delta G_{PBASE\text{-}graphene}$. For instance, the recent study indicated that $\Delta G_{PBASE\text{-}graphene}$ could improve from ~105 to ~251kJ/mol by adapting pyrene maleimide (Pymal) as a linker-graphene instead of commonly used PBASE.[152] It is expected that the increasing the number of pi-stacking of aromatic molecules on graphene surface improves the overall stability of the system.[152] Likewise, further enhancement in specificity could be also done through improvement in $\Delta G_{bind, Ap}$ by careful *Ap* design, *e.g,* through reducing the stability of G-quadruplex formation by other ions.

Besides the taking advantage of the thermodynamics involved with sensing components, it is important to explore the influence of the intrinsic and extrinsic defects in the sensing layer. It was reported that the curved deformation morphology (micro- and nano-meter scale) of the sensing layer (*e.g.* graphene) can modulate the Debye length.[204] Increasing Debye length in ionic solution would lead to the decrease of the screening of the DNA/RNA molecules, contributing to the enhancement of sensitivity as compared to flat and unmodified graphene.[204] In addition, the change of the electrical bandgap in vicinity of the deformed graphene region could potentially change the local conductivity as well, leading to enhanced sensitivity. Therefore, careful control of the deformation of graphene sensing layer could be incorporated with the design of the sensor for single molecule detection.

REFERENCES

1. Park, J. W.; Kang, B. H.; Kim, H. J. A Review of Low-temperature Solution-processed Metal Oxide Thin-film Transistors for Flexible Electronics. *Adv. Funct. Mater.* **2020**, *30* (20), 1904632.

2. Petti, L.; Münzenrieder, N.; Vogt, C.; Faber, H.; Büthe, L.; Cantarella, G.; Bottacchi, F.; Anthopoulos, T. D.; Tröster, G. Metal Oxide Semiconductor Thin-Film Transistors for Flexible Electronics. Applied Physics Reviews 2016, 3 (2).

3. Faber, H.; Das, S.; Lin, Y.-H.; Pliatsikas, N.; Zhao, K.; Kehagias, T.; Dimitrakopulos, G.; Amassian, A.; Patsalas, P. A.; Anthopoulos, T. D. Heterojunction Oxide Thin-Film Transistors with Unprecedented Electron Mobility Grown from Solution. Sci Adv 2017, 3 (3), e1602640.

4. Reese, C.; Roberts, M.; Ling, M.-M.; Bao, Z. Organic Thin Film Transistors. Mater. Today 2004, 7 (9), 20–27.

5. Newman, C. R.; Frisbie, C. D.; da Silva Filho, D. A.; Brédas, J.-L.; Ewbank, P. C.; Mann, K. R. Introduction to Organic Thin Film Transistors and Design of N-Channel Organic Semiconductors. Chem. Mater. 2004, 16 (23), 4436–4451.

6. Borchert, J. W.; Zschieschang, U.; Letzkus, F.; Giorgio, M.; Weitz, R. T.; Caironi, M.; Burghartz, J. N.; Ludwigs, S.; Klauk, H. Flexible Low-Voltage High-Frequency Organic Thin-Film Transistors. Sci Adv 2020, 6 (21), eaaz5156.

7. Cong, Y.; Han, D.; Dong, J.; Zhang, S.; Zhang, X.; Wang, Y. Fully Transparent High Performance Thin Film Transistors with Bilayer ITO/Al-Sn-Zn-O Channel Structures Fabricated on Glass Substrate. Sci. Rep. 2017, 7 (1), 1497.

8. Nakamura, K.; Kobayashi, A.; Ueno, K.; Ohta, J.; Fujioka, H. AlN/InAlN Thin-Film Transistors Fabricated on Glass Substrates at Room Temperature. Sci. Rep. 2019, 9 (1), 6254.

9. Su, L.-Y.; Huang, J. Demonstration of Radio-Frequency Response of Amorphous IGZO Thin Film Transistors on the Glass Substrate. Solid State Electron. 2015, 104, 122–125.

10. Rullyani, C.; Sung, C.-F.; Lin, H.-C.; Chu, C.-W. Flexible Organic Thin Film Transistors Incorporating a Biodegradable CO2-Based Polymer as the Substrate and Dielectric Material. Sci. Rep. 2018, 8 (1), 1–10.

11. Fortunato, G.; Pecora, A.; Maiolo, L. Polysilicon Thin-Film Transistors on Polymer Substrates. Mater. Sci. Semicond. Process. 2012, 15 (6), 627–641.

12. Lee, S.-K.; Jang, H. Y.; Jang, S.; Choi, E.; Hong, B. H.; Lee, J.; Park, S.; Ahn, J.-H. All Graphene-Based Thin Film Transistors on Flexible Plastic Substrates. Nano Lett. 2012, 12 (7), 3472–3476.

13. Kuo, Y. Thin Film Transistor Technology—Past, Present, and Future. Electrochem. Soc. Interface 2013, 22 (1), 55.

14. Fernández, M. R.; Casanova, E. Z.; Alonso, I. G. Review of Display Technologies Focusing on Power Consumption. Sustain. Sci. Pract. Policy 2015, 7 (8), 10854–10875.

15. Nomura, K.; Ohta, H.; Takagi, A.; Kamiya, T.; Hirano, M.; Hosono, H. Room-Temperature Fabrication of Transparent Flexible Thin-Film Transistors Using Amorphous Oxide Semiconductors. Nature 2004, 432, 488−492.

16. Kamiya, T.; Nomura, K.; Hosono, H. Present Status of Amorphous In−Ga−Zn−O Thin-Film Transistors. Sci. Technol. Adv. Mater. 2010, 11, 044305.

17. Lee, J. H.; Kim, D. H.; Yang, D. J.; Hong, S. Y.; Yoon, K. S.;Hong, P. S.; Jeong, C. O.; Park, H. S.; Kim, S. Y.; Lim, S. K.; Kim, S.S.; Son, K. S.; Kim, T. S.; Kwon, J. J.; Lee, S. Y. World's Largest (15-Inch) XGA AMLCD Panel Using IGZO Oxide TFT. SID SymposiumDigest of Technical Papers, 2008; p 625.

18. Shin, W.-S.; Ahn, H.-A.; Na, J.-S.; Hong, S.-K.; Kwon, O.-K.;Lee, J.-H.; Um, J.-G.; Jang, J.; Kim, S.-H.; Lee, J.-S. A Driving Methodof Pixel Circuit Using a-IGZO TFT for Suppression of ThresholdVoltage Shift in AMLED Displays. IEEE Electron Device Lett. 2017, 38,760−762.

19. Um, J. G.; Jeong, D. Y.; Jung, Y.; Moon, J. K.; Jung, Y. H.; Kim,S.; Kim, S. H.; Lee, J. S.; Jang, J. Active-Matrix GaN μ-LED DisplayUsing Oxide Thin-Film Transistor Backplane and Flip Chip LED Bonding. Adv. Electron. Mater. 2019, 5, 1800617.

20. Hung, M. H.; Chen, C. H.; Lai, Y. C.; Tung, K. W.; Lin, W. T; Wang, H. H.; Chan, F. J.; Cheng, C. C.; Chuang, C. T.; Huang, Y. S.; Yeh, C. N.; Liu C. Y.; Tseng, J. P.; Chiang, M. F.; Lin, Y. C. Ultra Low Voltage 1-V RFID Tag Implement in a-IGZO TFT Technology on Plastic. In *2017 IEEE International Conference on RFID (RFID)* **2017**, pp 193–197.

21. Chasin, A.; Volskiy, V.; Libois, M.; Myny, K.; Nag, M.; Rockelé, M.; Vandenbosch, G. A. E.; Genoe, J.; Gielen, G.; Heremans, P. An Integrated a-IGZO UHF Energy Harvester for Passive RFID Tags. *IEEE Trans. Electron Devices* **2014**, *61*, 3289–3295.

22. Meister, T.; Ishida, K.; Shabanpour, R.; Boroujeni, B. K.; Carta, C.; Ellinger, F.; Münzenrieder, N.; Petti, L.; Salvatore, G. A.; Tröster, G.; Wagner, M.; Ghesquiere, P.; Kiefl, S.; Krebs, M. Bendable Energy-Harvesting Module with Organic Photovoltaic, Rechargeable Battery, and a-IGZO TFT Charging Electronics. In *2015 European Conference on Circuit Theory and Design (ECCTD)*; 2015, pp 1-4.

23. Wu, S. H.; Jia, X.; Kui, M.; Shuai, C. C.; Hsieh, T. Y.; Lin, H. C.; Chen, D.; Lin, C. B.; Wu, J. Y.; Yew, T. R.; Endo, Y.; Kato, K.; Yamazaki, S. Extremely Low Power C-Axis Aligned Crystalline In-Ga-Zn-O 60 nm Transistor Integrated with Industry 65 nm Si MOSFET for IoT Normally-off CPU Application. In *2016 IEEE Symposium on VLSI Technology*; 2016, pp 1–2.

24. Wu, S. H.; Jia, X. Y.; Li, X.; Shuai, C. C.; Lin, H. C.; Lu, M. C.; Wu, T. H.; Liu, M. Y.; Wu, J. Y.; Matsubayashi, D.; Kato, K.; Yamazaki, S. Performance Boost of Crystalline In-Ga-Zn-O Material and Transistor with Extremely Low Leakage for IoT Normally-off CPU Application. In *2017 Symposium on VLSI Technology*; 2017, pp T166–T167.

25. Gutierrez-Heredia, G.; Rodriguez-Lopez, O.; Garcia-Sandoval, A.; Voit, W. E. Highly Stable Indium-Gallium-Zinc-Oxide Thin-Film Transistors on Deformable Softening Polymer Substrates. *Adv. Electron. Mater.* **2017**, *3*, 1700221.

26. Jin, S. H.; Kang, S.-K.; Cho, I.-T.; Han, S. Y.; Chung, H. U.; Lee, D. J.; Shin, J.; Baek, G. W.; Kim, T.-I.; Lee, J.-H.; Rogers, J. A. Water-Soluble Thin Film Transistors and Circuits Based on Amorphous Indium-Gallium-Zinc Oxide. *ACS Appl. Mater. Interfaces* **2015**, *7*, 8268–8274.

27. Fortunato, E.; Martins, R. Where Science Fiction Meets Reality? With Oxide Semiconductors! *Phys. Status Solidi RRL* **2011**, *5*, 336–339.

28. Fortunato, E.; Barros, R.; Barquinha, P.; Figueiredo, V.; Park, S.-H. K.; Hwang, C.-S.; Martins, R. Transparent P-Type SnOx Thin Film Transistors Produced by Reactive Rf Magnetron Sputtering Followed by Low Temperature Annealing. *Appl. Phys. Lett.* **2010**, *97*, 052105.

29. Ogo, Y.; Hiramatsu, H.; Nomura, K.; Yanagi, H.; Kamiya, T.; Hirano, M.; Hosono, H. P-Channel Thin-Film Transistor Using P-Type Oxide Semiconductor, SnO. *Appl. Phys. Lett.* **2008**, *93*, 032113.

30. Ogo, Y.; Hiramatsu, H.; Nomura, K.; Yanagi, H.; Kamiya, T.; Kimura, M.; Hirano, M.; Hosono, H. Tin Monoxide as an S-Orbital-Based P-Type Oxide Semiconductor: Electronic Structures and TFT Application. *Phys. Status Solidi* **2009**, *206*, 2187–2191.

31. K. Rajshekar, D. Kannadassan: P-Type Cu2O TFTs for Active Matrix Displays: Physical Modeling and Numerical Simulation

32. Hosono, H. Current Status and Future Challenge of Oxide Semiconductors. *in 2012 19th International Workshop on Active-Matrix Flat Panel Displays and Devices (AM-FPD).* **2012,** 1-4.

33. Barros, R.; Saji, K. J.; Waerenborgh, J. C.; Barquinha, P.; Pereira, L.; Carlos, E.; Martins, R.; Fortunato, E. Role of Structure and Composition on the Performances of P-Type Tin

Oxide Thin-Film Transistors Processed at Low-Temperatures. *Nanomaterials (Basel)* **2019**, *9*, 320-334.

34. Wang, Z.; Nayak, P. K.; Caraveo-Frescas, J. A.; Alshareef, H. N. Recent Developments in P-Type Oxide Semiconductor Materials and Devices. Adv. Mater. 2016, 28 (20), 3831–3892.

35. Hu, Y.; Hwang, J.; Lee, Y.; Conlin, P.; Schlom, D. G. First Principles Calculations of Intrinsic Mobilities in Tin-Based Oxide Semiconductors SnO, SnO2, and Ta2SnO6. Journal of Applied 2019.

36. Shang, Z.-W.; Hsu, H.-H.; Zheng, Z.-W.; Cheng, C.-H. Progress and Challenges in P-Type Oxide-Based Thin Film Transistors. Nanotechnology Reviews 2019, 8 (1), 422–443.

37. H. Hosono, Y. Ogo, H. Yanagi, T. Kamiya, *Electrochem. Solid-State Lett.* 2011, **14**, H13.

38. N. F. Quackenbush, J. P. Allen, D. O. Scanlon, S. Sallis, J. A. Hewlett, A. S. Nandur, B. Chen, K. E. Smith, C. Weiland, D. A. Fischer, J. C. Woicik, B. E. White, G. W. Watson, L. F. J. Piper, *Chem. Mater.* 2013, **25**, 3114.

39. Jeong, C.-Y.; Lee, D.; Han, Y.-J.; Choi, Y.-J.; Kwon, H.-I. Subgap States in P-Channel Tin Monoxide Thin-Film Transistors from Temperature-Dependent Field-Effect Characteristics. *Semiconductor Science and Technology*. 2015, 085004.

40. Kim, H. J.; Park, S. Y.; Jung, H. Y.; Son, B. G.; Lee, C.-K.; Lee, C.-K.; Jeong, J. H.; Mo, Y.-G.; Son, K. S.; Ryu, M. K.; et al. Role of Incorporated Hydrogen on Performance and Photo-Bias Instability of Indium Gallium Zinc Oxide Thin Film Transistors. *J. Phys. D Appl. Phys.* **2012**, *46*, 055104.

41. Kriss, R., Pieper, K. J., Parks, J., & Edwards, M. A. (2021). Challenges of detecting lead in drinking water using at-home test kits. Environmental Science & Technology, 55(3), 1964-1972.

42. Nguyen, H., Sung, Y., O'Shaughnessy, K., Shan, X., & Shih, W. C. (2018). Smartphone nanocolorimetry for on-demand lead detection and quantitation in drinking water. Analytical chemistry, 90(19), 11517-11522.

43. Maity, A., Sui, X., Tarman, C. R., Pu, H., Chang, J., Zhou, G., Ren, R., Mao, S. and Chen, J. (2017). Pulse-driven capacitive lead ion detection with reduced graphene oxide field-effect transistor integrated with an analyzing device for rapid water quality monitoring. ACS sensors, 2(11), 1653-1661.

44. Pieper, K. J., Tang, M., & Edwards, M. A. (2017). Flint water crisis caused by interrupted corrosion control: Investigating "ground zero" home. Environmental science & technology, 51(4), 2007-2014.

45. Pieper, K. J.; Martin, R.; Tang, M.; Walters, L.; Parks, J.; Roy, S.; Devine, C.; Edwards, M. A. (2018). Evaluating water lead levels during the Flint water crisis. Environmental science & technology, 52(15), 8124-8132.

46. Masten, S. J., Davies, S. H., & Mcelmurry, S. P. (2016). Flint water crisis: what happened and why?. Journal-American Water Works Association, 108(12), 22-34.

47. Lopez, P. D. United States Environmental Protection Agency Letter to Commissioner. (2019).

48. Lanphear, B. P.; Hornung, R.; Khoury, J.; Yolton, K.; Baghurst, P.; Bellinger, D. C.; Canfield, R. L.; Dietrich, K. N.; Bornschein, R.; Greene, T.; Rothenberg, S. J.; Needleman, H. L.; Schnaas, L.; Wasserman, G.; Graziano, J.; Roberts, R. (2005). Low-level environmental lead exposure and children's intellectual function: an international pooled analysis. Environmental health perspectives, 113(7), 894-899.

49. Wilbur, S. A Comparison of the Relative Cost and Productivity of Traditional Metals Analysis Techniques versus ICP-MS in High Throughput Commercial Laboratories. Agilent Technologies Application Note 2005.

50. Tighe, M., Bielski, M., Wilson, M., Ruscio-Atkinson, G., Peaslee, G. F., & Lieberman, M. (2020). A sensitive XRF screening method for lead in drinking water. Analytical chemistry, 92(7), 4949-4953.

51. Li, Y., Wang, C., Zhu, Y., Zhou, X., Xiang, Y., He, M., & Zeng, S. (2017). Fully integrated graphene electronic biosensor for label-free detection of lead (II) ion based on G-quadruplex structure-switching. Biosensors and Bioelectronics, 89, 758-763.

52. Xu, K., Meshik, X., Nichols, B. M., Zakar, E., Dutta, M., & Stroscio, M. A. (2014). Graphene-and aptamer-based electrochemical biosensor. Nanotechnology, 25(20), 205501.

53. Su, Y. C.; Hsu, W. E. Review Field Effect Transistor Biosensing: Devices and Clinical Applications. *ECS J. Solid State Sci. Technol. 2018, 7, Q3196*

54. Mao, S.; Chang, J.; Pu, H.; Lu, G.; He, Q.; Zhang, H.; Chen, J. Two-Dimensional Nanomaterial-Based Field-Effect Transistors for Chemical and Biological Sensing. *Chem. Soc. Rev.* **2017**, *46* (22), 6872–6904.

55. Nehra, A.; Pal Singh, K. Current Trends in Nanomaterial Embedded Field Effect Transistor-Based Biosensor. *Biosens. Bioelectron.* **2015**, *74*, 731–743.

56. Mu, L.; Chang, Y.; Sawtelle, S. D.; Wipf, M.; Duan, X.; Reed, M. A. Silicon Nanowire Field-Effect Transistors—A Versatile Class of Potentiometric Nanobiosensors. *IEEE Access* **2015**, *3*, 287–302.

57. Schwierz, F. Graphene Transistors. *Nat. Nanotechnol.* **2010**, *5* (7), 487–496.

58. Rumyantsev, S.; Liu, G.; Shur, M. S.; Potyrailo, R. A.; Balandin, A. A. Selective Gas Sensing with a Single Pristine Graphene Transistor. *Nano Lett.* **2012**, *12* (5), 2294–2298.

59. Fu, W.; Jiang, L.; van Geest, E. P.; Lima, L. M. C.; Schneider, G. F. Sensing at the Surface of Graphene Field-Effect Transistors. *Adv. Mater.* **2017**, *29* (6).

60. Li, J.; Tyagi, A.; Huang, T.; Liu, H.; Sun, H.; You, J.; Alam, M. M.; Li, X.; Gao, Z. Aptasensors Based on Graphene Field-Effect Transistors for Arsenite Detection. *ACS Appl. Nano Mater.* **2022**, *5* (9), 12848–12854.

61. Forouzanfar, S.; Alam, F.; Pala, N.; Wang, C. Review—A Review of Electrochemical Aptasensors for Label-Free Cancer Diagnosis. *J. Electrochem. Soc.* **2020**, *167* (6), 067511.

62. Ten Years Progress of Electrical Detection of Heavy Metal Ions (HMIs) Using Various Field-Effect Transistor (FET) Nanosensors: A Review

63. Guo, W.; Zhang, C.; Ma, T.; Liu, X.; Chen, Z.; Li, S.; Deng, Y. Advances in Aptamer Screening and Aptasensors' Detection of Heavy Metal Ions. J. Nanobiotechnology 2021, 19 (1), 166.

64. Ping, J.; Vishnubhotla, R.; Xi, J.; Ducos, P.; Saven, J. G.; Liu, R.; Johnson, A. T. C. All-Electronic Quantification of Neuropeptide-Receptor Interaction Using a Bias-Free Functionalized Graphene Microelectrode. ACS Nano 2018, 12 (5), 4218–4223.

65. Seo, G.; Lee, G.; Kim, M. J.; Baek, S.-H.; Choi, M.; Ku, K. B.; Lee, C.-S.; Jun, S.; Park, D.; Kim, H. G.; Kim, S.-J.; Lee, J.-O.; Kim, B. T.; Park, E. C.; Kim, S. I. Rapid Detection of COVID-19 Causative Virus (SARS-CoV-2) in Human Nasopharyngeal Swab Specimens Using Field-Effect Transistor-Based Biosensor. ACS Nano 2020, 14 (4), 5135–5142.

66. Majdinasab, M.; Marty, J. L. Recent Advances in Electrochemical Aptasensors for Detection of Biomarkers. Pharmaceuticals 2022, 15 (8).

67. Lei, Z.; Lei, P.; Guo, J.; Wang, Z. Recent Advances in Nanomaterials-Based Optical and Electrochemical Aptasensors for Detection of Cyanotoxins. Talanta 2022, 248, 123607.

68. Ban, D. K.; Bodily, T.; Karkisaval, A. G.; Dong, Y.; Natani, S.; Ramanathan, A.; Ramil, A.; Srivastava, S.; Bandaru, P.; Glinsky, G.; Lal, R. Rapid Self-Test of Unprocessed Viruses of SARS-CoV-2 and Its Variants in Saliva by Portable Wireless Graphene Biosensor. Proc. Natl. Acad. Sci. U. S. A. 2022, 119 (28), e2206521119.

69. Chen, F.; Qing, Q.; Xia, J.; Tao, N. Graphene Field-Effect Transistors: Electrochemical Gating, Interfacial Capacitance, and Biosensing Applications. Chem. Asian J. 2010, 5, 2144−2153.

70. Torricelli, F.; Adrahtas, D. Z.; Bao, Z.; Berggren, M.; Biscarini, F.; Bonfiglio, A.; Bortolotti, L.; Frisbie, C. D.; Macchia, E.; Malliaras, G. G.; McCulloch, I.; Moser, M.; Nguyen, T. Q.; Owens, R. M.; Salleo, A.; Spanu, A.; Torsi, L. Electrolyte-gated transistors for enhanced performance bioelectronics. Nat. Rev. Methods Primers 2021, 1, 1−24.

71. Ang, P. K.; Chen, W.; Wee, A. T. S.; Loh, K. P. Solution-gated epitaxial graphene as pH sensor. J. Am. Chem. Soc. 2008, 130, 14392− 14393.

72. Ohno, Y.; Maehashi, K.; Yamashiro, Y.; Matsumoto, K. Electrolyte-gated graphene field-effect transistors for detecting pH and protein adsorption. Nano Lett. 2009, 9, 3318−3322.

73. Wen, Y., Li, F.Y., Dong, X., Zhang, J., Xiong, Q. and Chen, P. (2013), The Electrical Detection of Lead Ions Using Gold-Nanoparticle- and DNAzyme-Functionalized Graphene Device. Advanced Healthcare Materials, 2: 271-274.

74. Falina, S., Syamsul, M., Rhaffor, N. A., Sal Hamid, S., Mohamed Zain, K. A., Abd Manaf, A., & Kawarada, H. (2021). Ten years progress of electrical detection of heavy metal ions (HMIs) using various field-effect transistor (FET) nanosensors: A Review. Biosensors, 11(12), 478.

75. Yang, D., Liu, X., Zhou, Y., Luo, L., Zhang, J., Huang, A., Mao, Q., Chen, X. & Tang, L. (2017). Aptamer-based biosensors for detection of lead (ii) ion: a review. Analytical Methods, 9(13), 1976-1990.

76. Aliakbarinodehi, N., Jolly, P., Bhalla, N., Miodek, A., De Micheli, G., Estrela, P., & Carrara, S. (2017). Aptamer-based field-effect biosensor for tenofovir detection. Scientific reports, 7(1), 1-10.

77. Nakatsuka, N., Yang, K. A., Abendroth, J. M., Cheung, K. M., Xu, X., Yang, H., Zhao, C., Zhu, B., Rim, Y.S., Yang, Y., Weiss, P.S., & Andrews, A. M. (2018). Aptamer–field-effect transistors overcome Debye length limitations for small-molecule sensing. Science, 362(6412), 319-324.

78. Sigel, H.; Da Costa, C. P.; Martin, R. B. Interactions of lead (II) with nucleotides and their constituents. Coord. Chem. Rev. 2001, 219−221, 435−461.

79. Panca, A.; Panidi, J.; Faber, H.; Stathopoulos, S.; Anthopoulos, T. D.; Prodromakis, T. Flexible Oxide Thin Film Transistors, Memristors, and Their Integration. Adv. Funct. Mater. 2023, 33 (20).

80. Zhao, C.; Tan, C.; Lien, D.-H.; Song, X.; Amani, M.; Hettick, M.; Nyein, H. Y. Y.; Yuan, Z.; Li, L.; Scott, M. C.; Javey, A. Evaporated Tellurium Thin Films for P-Type Field-Effect Transistors and Circuits. Nat. Nanotechnol. 2020, 15 (1), 53–58.

81. Kim, M.-G.; Kanatzidis, M. G.; Facchetti, A.; Marks, T. J. Low-Temperature Fabrication of High-Performance Metal Oxide Thin-Film Electronics via Combustion Processing. Nat. Mater. 2011, 10 (5), 382–388.

82. Hosono, H. How We Made the IGZO Transistor. Nature Electronics 2018, 1 (7), 428–428.

83. Lai, P.-C.; Lin, C.-L.; Kanicki, J. Novel Top-Anode OLED/a-IGZO TFTs Pixel Circuit for 8K4K AM-OLEDs. IEEE Trans. Electron Devices 2019, 66 (1), 436–444.

84. Kim, D.; Kim, Y.; Lee, S.; Kang, M. S.; Kim, D. H.; Lee, H. High Resolution a-IGZO TFT Pixel Circuit for Compensating Threshold Voltage Shifts and OLED Degradations. IEEE Journal of the Electron Devices Society 2017, 5 (5), 372–377.

85. Zhu, H.; Shin, E.; Liu, A.; Ji, D.; Xu, Y.; Noh, Y. Printable Semiconductors for Backplane TFTs of Flexible OLED Displays. Adv. Funct. Mater. 2020, 30 (20), 1904588.

86. Nomura, K.; Kamiya, T.; Hosono, H. Ambipolar Oxide Thin-Film Transistor. Adv. Mater. 2011, 23 (30), 3431–3434.

87. Liu, A.; Zhu, H.; Noh, Y.-Y. Polyol Reduction: A Low-Temperature Eco-Friendly Solution Process for P-Channel Copper Oxide-Based Transistors and Inverter Circuits. ACS Appl. Mater. Interfaces 2019, 11 (36), 33157–33164.

88. Nomura, K.; Aoki, T.; Nakamura, K.; Kamiya, T.; Nakanishi, T.; Hasegawa, T.; Kimura, M.; Kawase, T.; Hirano, M.; Hosono, H. Three-Dimensionally Stacked Flexible Integrated Circuit: Amorphous Oxide/polymer Hybrid Complementary Inverter Using N-Type a-In--Ga--Zn--O and P-Type Poly-(9, 9-Dioctylfluorene-Co-Bithiophene) Thin-Film Transistors. Appl. Phys. Lett. 2010, 96 (26).

89. Luo, H.; Liang, L.; Cao, H.; Dai, M.; Lu, Y.; Wang, M. Control of Ambipolar Transport in SnO Thin-Film Transistors by Back-Channel Surface Passivation for High Performance Complementary-like Inverters. ACS Appl. Mater. Interfaces 2015, 7 (31), 17023–17031.

90. S. H. Kim, I. H. Baek, K. Da Hye, J. J. Pyeon, T. M. Chung, S. H. Baek, J. S. Kim, J. H. Han, S. K. Kim, *J. Mater. Chem.* **2017**, *5*, 3139-3145.

91. Martins, R.; Nathan, A.; Barros, R.; Pereira, L.; Barquinha, P.; Correia, N.; Costa, R.; Ahnood, A.; Ferreira, I.; Fortunato, E. Complementary Metal Oxide Semiconductor Technology with and on Paper. *Adv. Mater.* **2011**, *23*, 4491–4496.

92. Jeong, C.-Y.; Lee, D.; Han, Y.-J.; Choi, Y.-J.; Kwon, H.-I. Subgap States in P-Channel Tin Monoxide Thin-Film Transistors from Temperature-Dependent Field-Effect Characteristics. *Semiconductor Science and Technology*. 2015, 085004.

93. Li, Y.; Yang, J.; Qu, Y.; Zhang, J.; Zhou, L.; Yang, Z.; Lin, Z.; Wang, Q.; Song, A.; Xin, Q. Ambipolar SnO_x Thin-Film Transistors Achieved at High Sputtering Power. *Appl. Phys. Lett.* **2018**, *112*, 182102.

94. Han, Y.; Choi, Y.; Cho, I.; Jin, S. H.; Lee, J.; Kwon, H. Improvement of Long-Term Durability and Bias Stress Stability in P-Type SnO Thin-Film Transistors Using a SU-8 Passivation Layer. *IEEE Electron Device Lett.* **2014**, *35*, 1260–1262.

95. Luo, H.; Liang, L.; Cao, H.; Dai, M.; Lu, Y.; Wang, M. Control of Ambipolar Transport in SnO Thin-Film Transistors by Back-Channel Surface Passivation for High Performance Complementary-like Inverters. *ACS Appl. Mater. Interfaces* **2015**, *7*, 17023–17031.

96. Caraveo-Frescas, J. A.; Nayak, P. K.; Al-Jawhari, H. A.; Granato, D. B.; Schwingenschlögl, U.; Alshareef, H. N. Record Mobility in Transparent P-Type Tin Monoxide Films and Devices by Phase Engineering. *ACS Nano* **2013**, *7*, 5160–5167.

97. Nomura, K.; Kamiya, T.; Ohta, H.; Hirano, M. Defect Passivation and Homogenization of Amorphous Oxide Thin-Film Transistor by Wet O2 Annealing. J. Phys. D Appl. Phys. 2008.

98. Ref. Yang, Y.; Wang, Y.; Yin, S. Oxygen vacancies confined in SnO2 nanoparticles for desirable electronic structure and enhanced visible light photocatalytic activity. Appl. Surf. Sci. 2017, 420, 399–406.

99. Kamiya, T.; Nakahata, K.; Tan, Y. T.; Durrani, Z. A. K.; Shimizu, I. Growth, Structure, and Transport Properties of Thin (>10 nm) N-Type Microcrystalline Silicon Prepared on Silicon Oxide and Its Application to Single-Electron Transistor. *J. Appl. Phys.* **2001**, *89*, 6265–6271.

100. Nomura, K.; Kamiya, T.; Hosono, H. Interface and Bulk Effects for Bias—light-Illumination Instability in Amorphous-In-Ga-Zn-O Thin-Film Transistors. *J. Soc. Inf. Disp.* **2010**, *18*, 789.

101. Varley, J. B.; Schleife, A.; Janotti, A.; Van de Walle, C. G. Ambipolar Doping in SnO. Appl. Phys. Lett. 2013, 103, 082118.

102. Lee, A. W.; Le, D.; Matsuzaki, K.; Nomura, K. Hydrogen-Defect Termination in SnO for P-Channel TFTs. ACS Appl. Electron. Mater. 2020, 2 (4), 1162–1168.

103. Ren, Y.; Yang, X.; Zhou, L.; Mao, J.; Han, S.; Zhou, Y. Recent Advances in Ambipolar Transistors for Functional Applications. Adv. Funct. Mater. 2019, 29 (40), 1902105.

104. Wang, Z.; Nayak, P. K.; Caraveo-Frescas, J. A. Recent Developments in p-Type Oxide Semiconductor Materials and Devices. Advanced 2016.

105. Hiramatsu, H.; Nomura, K.; Yanagi, H.; Kamiya, T. P-Channel Thin-Film Transistor Using P-Type Oxide Semiconductor, SnO. J. Phys. D Appl. Phys. 2008.

106. Kim, T.; Kim, J.-K.; Yoo, B.; Xu, H.; Yim, S.; Kim, S.-H.; Yu, H.-Y.; Jeong, J. K. Improved Switching Characteristics of P-Type Tin Monoxide Field-Effect Transistors through Schottky Energy Barrier Engineering. J. Mater. Chem. 2020, 8 (1), 201–208.

107. Yim, S.; Kim, T.; Yoo, B.; Xu, H.; Youn, Y.; Han, S.; Jeong, J. K. Lanthanum Doping Enabling High Drain Current Modulation in a P-Type Tin Monoxide Thin-Film Transistor. ACS Appl. Mater. Interfaces 2019, 11 (50), 47025–47036.

108. Wager, J. F.; Kuhn, K. Device Physics Modeling of Surfaces and Interfaces from an Induced Gap State Perspective. Crit. Rev. Solid State Mater. Sci. 2017, 42 (5), 373–415.

109. Fortunato, E.; Barquinha, P.; Martins, R. Oxide Semiconductor Thin-Film Transistors: A Review of Recent Advances. Adv. Mater. 2012, 24 (22), 2945–2986.

110. Hsu, P.-C.; Hsu, C.-J.; Chang, C.-H.; Tsai, S.-P.; Chen, W.-C.; Hsieh, H.-H.; Wu, C.-C. Sputtering Deposition of P-Type SnO Films with SnO_2 Target in Hydrogen-Containing Atmosphere. ACS Appl. Mater. Interfaces 2014, 6 (16), 13724−13729.

111. Li, Y.; Xin, Q.; Du, L.; Qu, Y.; Li, H.; Kong, X.; Wang, Q.; Song, A. Extremely Sensitive Dependence of SnOx Film Properties on Sputtering Power. Sci. Rep. 2016, 6, 36183.

112. H.C. Lin, K.L. Yeh, M.H. Lee, Y.C. Su, T.Y. Huang, S.W. Shen, H.Y. Lin, A Novel Methodology for Extracting Effective Density-of-States in Poly-Si Thin-Film Transistors. In IEDM Technical Digest. IEEE International Electron Devices Meeting, in *IEDM Tech. Dig. IEEE Int. Electron Devices Meeting* **2004**, 781–784.

113. Kimura, M.; Nakanishi, T.; Nomura, K.; Kamiya, T.; Hosono, H. Trap Densities in Amorphous-InGaZnO4 Thin-Film Transistors. Appl. Phys. Lett. 2008, 92 (13).

114. S. Yasuno, T. Kugimiya, S. Morita, A. Miki, F. Ojima, S. Sumie, *Appl. Phys. Lett*. **2011**, *98*, 102107-3.

115. D. H. Lee, K. Kawamura, K. Nomura, T. Kamiya, H. Hosono, *Electrochem. Solid-State Lett.* **2010**, *13*, H324-H327.

116. Studenikin, S. A.; Golego, N.; Cocivera, M. Carrier Mobility and Density Contributions to Photoconductivity Transients in Polycrystalline ZnO Films. J. Appl. Phys. 2000, 87 (5), 2413–2421.

117. Murphy, T. E.; Moazzami, K.; Phillips, J. D. Trap-Related Photoconductivity in ZnO Epilayers. J. Electron. Mater. 2006, 35 (4), 543–549.

118. Togo, A.; Oba, F.; Tanaka, I.; Tatsumi, K. First-Principles Calculations of Native Defects in Tin Monoxide. Phys. Rev. B Condens. Matter 2006, 74 (19), 195128.

119. Guerra-Nuñez, C.; Döbeli, M.; Michler, J.; Utke, I. Reaction and Growth Mechanisms in Al2O3 Deposited via Atomic Layer Deposition: Elucidating the Hydrogen Source. Chem. Mater. 2017, 29 (20), 8690–8703.

120. Puurunen, R. L. Surface Chemistry of Atomic Layer Deposition: A Case Study for the Trimethylaluminum/water Process. J. Appl. Phys. 2005, 97 (12), 121301.

121. Dingemans, G.; van de Sanden, M. C. M.; Kessels, W. M. M. Influence of the Deposition Temperature on the c-Si Surface Passivation by Al2O3 Films Synthesized by ALD and PECVD. Electrochem. Solid-State Lett. 2009, 13 (3), H76.

122. Groner, M. D.; Fabreguette, F. H.; Elam, J. W.; George, S. M. Low-Temperature Al2O3 Atomic Layer Deposition. Chem. Mater. 2004, 16 (4), 639–645.

123. S. Hsu, Y. Li, M. Tu, J. He, I. Chiu, P. Chen, M. Lee, J. Chen, I. Cheng, in *Proc. 23rd Int. Workshop on Active-Matrix Flatpanel Displays and Devices (AM-FPD)* **2016**, 153–156.

124. K. Ghaffarzadeh, A. Nathan, J. Robertson, S. Kim, S. Jeon, C. Kim, U. Chung, J. Lee, *Appl. Phys. Lett*. **2010**, *97*, 143510-3.

125. Risteska, A.; Chan, K.-Y.; Anthopoulos, T. D.; Gordijn, A.; Stiebig, H.; Nakamura, M.; Knipp, D. Designing Organic and Inorganic Ambipolar Thin-Film Transistors and Inverters: Theory and Experiment. Org. Electron. 2012, 13 (12), 2816–2824.

126. J. M. Rabaey, A. P. Chandrakasan, B. Nikolić, Digital integrated circuits: a design perspective. *Pearson Education*, London, **2003**.

127. Yu, W. J.; Kim, U. J.; Kang, B. R.; Lee, I. H.; Lee, E.-H.; Lee, Y. H. Adaptive Logic Circuits with Doping-Free Ambipolar Carbon Nanotube Transistors. Nano Lett. 2009, 9 (4), 1401–1405.

128. Zeng, W.-J.; Zhou, X.-Y.; Pan, X.-J.; Song, C.-L.; Zhang, H.-L. High Performance CMOS-like Inverter Based on an Ambipolar Organic Semiconductor and Low Cost Metals. AIP Adv. 2013, 3 (1), 012101.

129. Matsuzaki, K.; Katase, T.; Kamiya, T.; Hosono, H. Symmetric Ambipolar Thin-Film Transistors and High-Gain CMOS-like Inverters Using Environmentally Friendly Copper Nitride. ACS Appl. Mater. Interfaces 2019, 11 (38), 35132–35137.

130. Keefe, A. D.; Pai, S.; Ellington, A. Aptamers as Therapeutics. Nat. Rev. Drug Discov. **2010**, 9 (7), 537–550.

131. Ni, S.; Zhuo, Z.; Pan, Y.; Yu, Y.; Li, F.; Liu, J.; Wang, L.; Wu, X.; Li, D.; Wan, Y.; Zhang, L.; Yang, Z.; Zhang, B.-T.; Lu, A.; Zhang, G. Recent Progress in Aptamer Discoveries and Modifications for Therapeutic Applications. ACS Appl. Mater. Interfaces **2021**, 13 (8), 9500–9519.

132. Yoo, H.; Jo, H.; Oh, S. S. Detection and beyond: Challenges and Advances in Aptamer-Based Biosensors. Materials Advances **2020**, 1 (8), 2663–2687

133. Jiang, Y.; Liu, N.; Guo, W.; Xia, F.; Jiang, L. Highly-Efficient Gating of Solid-State Nanochannels by DNA Supersandwich Structure Containing ATP Aptamers: A Nanofluidic IMPLICATION Logic Device. *J. Am. Chem. Soc.* **2012**, *134* (37), 15395–15401.

134. Liu, M.; Song, J.; Shuang, S.; Dong, C.; Brennan, J. D.; Li, Y. A Graphene-Based Biosensing Platform Based on the Release of DNA Probes and Rolling Circle Amplification. *ACS Nano* **2014**, *8* (6), 5564–5573.

135. Liu, Y.; Liu, Y.; Matharu, Z.; Rahimian, A.; Revzin, A. Detecting Multiple Cell-Secreted Cytokines from the Same Aptamer-Functionalized Electrode. *Biosens. Bioelectron.* **2015**, *64*, 43–50.

136. Nakatsuka, N.; Yang, K.-A.; Abendroth, J. M.; Cheung, K. M.; Xu, X.; Yang, H.; Zhao, C.; Zhu, B.; Rim, Y. S.; Yang, Y.; Weiss, P. S.; Stojanović, M. N.; Andrews, A. M. Aptamer–field-Effect Transistors Overcome Debye Length Limitations for Small-Molecule Sensing. *Science* **2018**, *362* (6412), 319–324.

137. Cai, B.; Wang, S.; Huang, L.; Ning, Y.; Zhang, Z.; Zhang, G.-J. Ultrasensitive Label-Free Detection of PNA–DNA Hybridization by Reduced Graphene Oxide Field-Effect Transistor Biosensor. *ACS Nano*. **2014,** *8*, (3), 2632–2638.

138. Araujo-Rocha, M.; Piro, B.; Noël, V.; Barbault, F. Computational Studies of a DNA-Based Aptasensor: Toward Theory-Driven Transduction Improvement. *J. Phys. Chem. B* **2021**, *125* (33), 9499–9506

139. White, R. J.; Phares, N.; Lubin, A. A.; Xiao, Y.; Plaxco, K. W. Optimization of Electrochemical Aptamer-Based Sensors via Optimization of Probe Packing Density and Surface Chemistry. *Langmuir* **2008**, *24* (18), 10513–10518.

140. MacDonald, H.; Bonnet, H.; Van der Heyden, A.; Defrancq, E.; Spinelli, N.; Coche-Guérente, L.; Dejeu, J. Influence of Aptamer Surface Coverage on Small Target Recognition: A SPR and QCM-D Comparative Study. *J. Phys. Chem. C* **2019**, *123* (22), 13561–13568.

141. Dong, Y.; Lee, A.; Ban, D. K.; Wang, K.; Bandaru, P. Femtomolar Level-Specific Detection of Lead Ions in Aqueous Environments, Using Aptamer-Derivatized Graphene Field-Effect Transistors. *ACS Appl. Nano Mater.* **2023**, *6* (3), 2228–2235.

142. Kriss, R.; Pieper, K. J.; Parks, J.; Edwards, M. A. Challenges of Detecting Lead in Drinking Water Using at-Home Test Kits. *Environ. Sci. Technol.* **2021**, *55* (3), 1964–1972.

143. Edwards, M.; Triantafyllidou, S.; Best, D. Elevated Blood Lead in Young Children due to Lead-Contaminated Drinking Water: Washington, DC, 2001-2004. *Environ. Sci. Technol.* **2009**, *43* (5), 1618–1623.

144. Hanna-Attisha, M.; LaChance, J.; Sadler, R. C.; Champney Schnepp, A. Elevated Blood Lead Levels in Children Associated With the Flint Drinking Water Crisis: A Spatial Analysis of Risk and Public Health Response. *Am. J. Public Health* **2016**, *106* (2), 283–290.

145. Da Costa, C. P.; Sigel, H. Lead(II)-Binding Properties of the 5'-Monophosphates of Adenosine (AMP2-), Inosine (IMP2-), and Guanosine (GMP2-) in Aqueous Solution. Evidence for Nucleobase-lead(II) Interactions. Inorg. Chem. **2000**, 39 (26), 5985–5993

146. Sigel, H.; Da Costa, C. P.; Martin, R. B. Interactions of Lead (II) with Nucleotides and Their Constituents. Coord. Chem. Rev. **2001**, 219, 435–461.

147. T Khoshbin, Z.; Housaindokht, M. R.; Izadyar, M.; Bozorgmehr, M. R.; Verdian, A. Theoretical Design and Experimental Study of New Aptamers with the Improved Target-Affinity: New Insights into the Pb2+-Specific Aptamers as a Case Study. J. Mol. Liq. **2019**, 289, 111159.

148. Li, Y.; Wang, C.; Zhu, Y.; Zhou, X.; Xiang, Y.; He, M.; Zeng, S. Fully Integrated Graphene Electronic Biosensor for Label-Free Detection of Lead (II) Ion Based on G-Quadruplex Structure-Switching. *Biosens. Bioelectron.* **2017**, *89* (Pt 2), 758–763.

149. Xu, K.; Meshik, X.; Nichols, B. M.; Zakar, E.; Dutta, M.; Stroscio, M. A. Graphene-and aptamer-based electrochemical biosensor. Nanotechnology **2014**, 25, 205501.

150. Marochkin, I. I.; Dorofeeva, O. V. Amide Bond Dissociation Enthalpies: Effect of Substitution on NC Bond Strength. *Computational and Theoretical Chemistry* **2012**, *991*, 182–191.

151. Mishyn, V.; Hugo, A.; Rodrigues, T.; Aspermair, P.; Happy, H.; Marques, L.; Hurot, C.; Othmen, R.; Bouchiat, V.; Boukherroub, R.; Knoll, W.; Szunerits, S. The Holy Grail of Pyrene-Based Surface Ligands on the Sensitivity of Graphene-Based Field Effect Transistors. Sensors & Diagnostics **2022**, 1 (2), 235–244.

152. Thodkar, K.; Cazade, P.-A.; Bergmann, F.; Lopez-Calle, E.; Thompson, D.; Heindl, D. Self-Assembled Pyrene Stacks and Peptide Monolayers Tune the Electronic Properties of Functionalized Electrolyte-Gated Graphene Field-Effect Transistors. ACS Appl. Mater. Interfaces **2021**, 13 (7), 9134–9142.

153. Le, H. T. N.; Park, J.; Cho, S. A Probeless Capacitive Biosensor for Direct Detection of Amyloid Beta 1-42 in Human Serum Based on an Interdigitated Chain-Shaped Electrode. *Micromachines* **2020**, *11* (9).

154. Salila Vijayalal Mohan, H. K.; Chee, W. K.; Li, Y.; Nayak, S.; Poh, C. L.; Thean, A. V. Y. A Highly Sensitive Graphene Oxide Based Label-Free Capacitive Aptasensor for Vanillin Detection. *Mater. Des.* **2020**, *186*, 108208.

155. Li, X.; Magnuson, C. W.; Venugopal, A.; Tromp, R. M.; Hannon, J. B.; Vogel, E. M.; Colombo, L.; Ruoff, R. S. Large-area graphene single crystals grown by low-pressure chemical vapor deposition of methane on copper. J. Am. Chem. Soc. 2011, 133, 2816−2819.

156. Kim, S.; Shin, S.; Kim, T.; Du, H.; Song, M.; Lee, C.; Kim, K.; Cho, S.; Seo, D. H.; Seo, S. Robust graphene wet transfer process through low molecular weight polymethylmethacrylate. Carbon 2016, 98, 352−357.

157. Gao, Z., Kang, H., Naylor, C. H., Streller, F., Ducos, P., Serrano, M. D., Ping, J., Zauberman, J., Carpick, R.W., Wang, Y.J., Park, Y.W., & Johnson, A. C. (2016). Scalable production of sensor arrays based on high-mobility hybrid graphene field effect transistors. ACS Applied Materials & Interfaces, 8(41), 27546-27552.

158. Li, J.; Tyagi, A.; Huang, T.; Liu, H.; Sun, H.; You, J.; Alam, M. M.; Li, X.; Gao, Z. Aptasensors Based on Graphene Field-Effect Transistors for Arsenite Detection. *ACS Appl. Nano Mater.* **2022**, *5* (9), 12848–12854.

159. Magar, H. S.; Hassan, R. Y. A.; Mulchandani, A. Electrochemical Impedance Spectroscopy (EIS): Principles, Construction, and Biosensing Applications. Sensors 2021, 21 (19).

160. Mei, B.-A.; Munteshari, O.; Lau, J.; Dunn, B.; Pilon, L. Physical Interpretations of Nyquist Plots for EDLC Electrodes and Devices. *J. Phys. Chem. C* **2018**, *122* (1), 194–206.

161. Yang, I.; Kim, S.-G.; Kwon, S. H.; Kim, M.-S.; Jung, J. C. Relationships between Pore Size and Charge Transfer Resistance of Carbon Aerogels for Organic Electric Double-Layer Capacitor Electrodes. *Electrochim. Acta* **2017**, *223*, 21–30.

162. Nian, Y.-R.; Teng, H. Influence of Surface Oxides on the Impedance Behavior of Carbon-Based Electrochemical Capacitors. *J. Electroanal. Chem.* **2003**, *540*, 119–127.

163. Khademi, M.; Barz, D. P. J. Structure of the Electrical Double Layer Revisited: Electrode Capacitance in Aqueous Solutions. *Langmuir* **2020**, *36* (16), 4250–4260.

164. Ji, H.; Zhao, X.; Qiao, Z.; Jung, J.; Zhu, Y.; Lui, Y.; Zhang, L. L.; Macdonald, A. H.; Ruoff, R. S. Capacitance of Carbon-Based Electrical Double-Layer Capacitors. *Nat. Commun.* **2014**, *5*, 3317.

165. Gerischer, H.; McIntyre, R.; Scherson, D.; Storck, W. Density of the Electronic States of Graphite: Derivation from Differential Capacitance Measurements. *J. Phys. Chem.* **1987**, *91*, 1930.

166. Hammad, W. A.; El-Hammamy, N. H.; Morshidy, M. H.; Alkamis, K.; Darweesh, M. A. Electrical Conductivity and Thermodynamic Studies on Sodium Dimethyldithiocarbamate in Non Aqueous Solvents Dimethylformamide (DMF), at Different Temperatures. *Scientific Reports*. **2022**, 12, 15634.

167. Liu, Y.; Yuan, L.; Yang, M.; Zheng, Y.; Li, L.; Gao, L.; Nerngchamnong, N.; Nai, C. T.; Sangeeth, C. S. S.; Feng, Y. P.; Nijhuis, C. A.; Loh, K. P. Giant Enhancement in Vertical Conductivity of Stacked CVD Graphene Sheets by Self-Assembled Molecular Layers. *Nat. Commun.* **2014**, *5*, 5461.

168. Bagherzadeh-Nobari, S.; Kalantarinejad, R. Real-Time Label-Free Detection of DNA Hybridization Using a Functionalized Graphene Field Effect Transistor: A Theoretical Study. *J. Nanopart. Res.* **2021**, *23* (8), 185.

169. Yue, W.; Tang, C.; Wang, C.; Bai, C.; Liu, S.; Xie, X.; Hua, H.; Zhang, Z.; Li, D. An Electricity-Fluorescence Double-Checking Biosensor Based on Graphene for Detection of Binding Kinetics of DNA Hybridization. *RSC Adv.* **2017**, *7* (70), 44559–44567.

170. Rastegar, S. F.; Pilar, R.; Moravkova, J.; Sadovska, G.; Parvulescu, V. I.; Pastvova, J.; Plsek, J.; Kaucky, D.; Kostkova, N.; Sazama, P. Platinum Nanoparticles on 3D Graphene-like Zeolite-Templated Carbon for Benzene Hydrogenation. *Catalysis Science & Technology* **2023**, *13* (17), 5120–5130.

171. Bosco, A.; Camunas-Soler, J.; Ritort, F. Elastic Properties and Secondary Structure Formation of Single-Stranded DNA at Monovalent and Divalent Salt Conditions. *Nucleic Acids Res.* **2014**, *42* (3), 2064–2074.

172. Zhu, C.-Y.; Lin, Z.-H.; Zhang, D.-Y.; Shi, J.-Y.; Peng, S.-A.; Jin, Z. Predicting the Level of Background Current Noise in Graphene Biosensor through a Non-Covalent Functionalization Process. *Crystals* **2023**, *13* (2), 359.

173. Silvestri, A.; Zayas-Arrabal, J.; Vera-Hidalgo, M.; Di Silvio, D.; Wetzl, C.; Martinez-Moro, M.; Zurutuza, A.; Torres, E.; Centeno, A.; Maestre, A.; Gómez, J. M.; Arrastua, M.; Elicegui, M.; Ontoso, N.; Prato, M.; Coluzza, I.; Criado, A. Ultrasensitive Detection of SARS-CoV-2 Spike Protein by Graphene Field-Effect Transistors. *Nanoscale* **2023**, *15* (3), 1076–1085.

174. Fei, Z.; Rodin, A. S.; Gannett, W.; Dai, S.; Regan, W.; Wagner, M.; Liu, M. K.; McLeod, A. S.; Dominguez, G.; Thiemens, M.; Castro Neto, A. H.; Keilmann, F.; Zettl, A.; Hillenbrand, R.; Fogler, M. M.; Basov, D. N. Electronic and Plasmonic Phenomena at Graphene Grain Boundaries. *Nat. Nanotechnol.* **2013**, *8* (11), 821–825.

175. Tang, H.; Zhao, Y.; Shan, S.; Yang, X.; Liu, D.; Cui, F.; Xing, B. Wrinkle- and Edge-Adsorption of Aromatic Compounds on Graphene Oxide as Revealed by Atomic Force Microscopy, Molecular Dynamics Simulation, and Density Functional Theory. *Environ. Sci. Technol.* **2018**, *52* (14), 7689–7697.

176. Anithaa, V. S.; Shankar, R.; Vijayakumar, S. DFT-Based Investigation on Adsorption of Methane on Pristine and Defected Graphene. *Struct. Chem.* **2017**, *28* (6), 1935–1952.

177. Khan, N. I., Mousazadehkasin, M., Ghosh, S., Tsavalas, J. G., & Song, E. (2020). An integrated microfluidic platform for selective and real-time detection of thrombin biomarkers using a graphene FET. *Analyst*, *145*(13), 4494-4503.

178. Dong, X., Shi, Y., Huang, W., Chen, P., & Li, L. J. (2010). Electrical detection of DNA hybridization with single-base specificity using transistors based on CVD-grown graphene sheets. *Advanced Materials*, *22*(14), 1649-1653.

179. Liu, W., Fu, Y., Zheng, B., Cheng, S., Li, W., Lau, T. C., & Liang, H. (2011). Kinetics and mechanism of conformational changes in a G-quadruplex of thrombin-binding aptamer induced by Pb2+. *The Journal of Physical Chemistry B*, *115*(44), 13051-13056..

180. Chu, S. W., Baek, S. J., Kim, D. C., Seo, S., Kim, J. S., & Park, Y. W. (2012). Charge transport in graphene doped with diatomic halogen molecules (I2, Br2) near Dirac point. *Synthetic metals*, *162*(17-18), 1689-1693.

181. Kim, S., Nah, J., Jo, I., Shahrjerdi, D., Colombo, L., Yao, Z., Tutuc, E. & Banerjee, S. K. (2009). Realization of a high mobility dual-gated graphene field-effect transistor with Al 2 O 3 dielectric. *Applied Physics Letters*, *94*(6), 062107.

182. Dorgan, V. E., Bae, M. H., & Pop, E. (2010). Mobility and saturation velocity in graphene on SiO 2. *Applied Physics Letters*, *97*(8), 082112.

183. Kumar, N., Rana, M., Geiwitz, M., Khan, N. I., Catalano, M., Ortiz-Marquez, J. C., Kitadai, H., Weber, A., Dweik, B., Ling, X., van Opijnen, T., & Burch, K. S. (2022). Rapid, multianalyte detection of opioid metabolites in wastewater. *ACS nano*, *16*(3), 3704-3714.

184. Ping, J., Vishnubhotla, R., Vrudhula, A., & Johnson, A. C. (2016). Scalable production of high-sensitivity, label-free DNA biosensors based on back-gated graphene field effect transistors. *ACS nano*, *10*(9), 8700-8704.

185. Armbruster, D. A., & Pry, T. (2008). Limit of blank, limit of detection and limit of quantitation. *The clinical biochemist reviews*, *29*(Suppl 1), S49.

186. Kang, H., Wang, X., Guo, M., Dai, C., Chen, R., Yang, L., ... & Wei, D. (2021). Ultrasensitive detection of SARS-CoV-2 antibody by graphene field-effect transistors. *Nano Letters*, *21*(19), 7897-7904.

187. Fu, W., Feng, L., Panaitov, G., Kireev, D., Mayer, D., Offenhäusser, A., & Krause, H. J. (2017). Biosensing near the neutrality point of graphene. *Science advances*, *3*(10), e1701247.

188. Das, A., Pisana, S., Chakraborty, B., Piscanec, S., Saha, S. K., Waghmare, U. V., Novoselov, K.S., Krishnamurthy, H.R., Geim, A.K., Ferrari, A.C. & Sood, A. K. (2008). Monitoring dopants by Raman scattering in an electrochemically top-gated graphene transistor. *Nature nanotechnology*, *3*(4), 210-215.

189. Wang, X., Zhu, Y., Olsen, T. R., Sun, N., Zhang, W., Pei, R., & Lin, Q. (2018). A graphene aptasensor for biomarker detection in human serum. *Electrochimica acta*, *290*, 356-363

190. Liu, J., Li, Q., Zou, Y., Qian, Q., Jin, Y., Li, G., Jiang, K. & Fan, S. (2013). The dependence of graphene Raman D-band on carrier density. *Nano letters*, *13*(12), 6170-6175.

191. Bruna, M., Ott, A. K., Ijäs, M., Yoon, D., Sassi, U., & Ferrari, A. C. (2014). Doping dependence of the Raman spectrum of defected graphene. *Acs Nano*, *8*(7), 7432-7441

192. Qasem, N. A. A.; Mohammed, R. H.; Lawal, D. U. Removal of Heavy Metal Ions from Wastewater: A Comprehensive and Critical Review. *npj Clean Water* **2021**, *4* (1), 1–15.

193. Li, G.; Bae, Y.; Mishrra, A.; Shi, B.; Giammar, D. E. Effect of Aluminum on Lead Release to Drinking Water from Scales of Corrosion Products. *Environ. Sci. Technol.* **2020**, *54* (10), 6142–6151.

194. Azoulay, A.; Garzon, P.; Eisenberg, M. J. Comparison of the Mineral Content of Tap Water and Bottled Waters. *J. Gen. Intern. Med.* **2001**, *16* (3), 168–175.

195. Khoshbin, Z.; Housaindokht, M. R.; Izadyar, M.; Bozorgmehr, M. R.; Verdian, A. The Investigation of the G-Quadruplex Aptamer Selectivity to Pb2+ Ion: A Joint Molecular Dynamics Simulation and Density Functional Theory Study. *J. Biomol. Struct. Dyn.* **2020**, *38* (12), 3659–3675.

196. Wu, X.; Yuan, H.; Zhao, R.; Wang, P.; Yuan, M.; Cao, H.; Ye, T.; Xu, F. Mechanisms of ssDNA Aptamer Binding to Cd^{2+} in Aqueous Solution: A Molecular Dynamics Study. *Int. J. Biol. Macromol.* **2023**, *251*, 126412.

197. Khoshbin, Z.; Housaindokht, M. R. Computer-Aided Aptamer Design for Sulfadimethoxine Antibiotic: Step by Step Mutation Based on MD Simulation Approach. *J. Biomol. Struct. Dyn.* **2021**, *39* (9), 3071–3079.

198. Kankia, B. I.; Marky, L. A. Folding of the Thrombin Aptamer into a G-Quadruplex with Sr^{2+}: Stability, Heat, and Hydration. *J. Am. Chem. Soc.* **2001**, *123* (44), 10799–10804.

199. Włodarczyk, A.; Grzybowski, P.; Patkowski, A.; Dobek, A. Effect of Ions on the Polymorphism, Effective Charge, and Stability of Human Telomeric DNA. Photon Correlation Spectroscopy and Circular Dichroism Studies. *J. Phys. Chem. B* **2005**, *109* (8), 3594–3605.

200. Jissy, A. K.; Ashik, U. P. M.; Datta, A. Nucleic Acid G-Quartets: Insights into Diverse Patterns and Optical Properties. *J. Phys. Chem. C* **2011**, *115* (25), 12530–12546.

201. Mostafavi, N.; Ebrahimi, A. The Estimation of H-Bond and Metal Ion-Ligand Interaction Energies in the G-Quadruplex ⋯ Mn+ Complexes. *J. Mol. Struct.* **2018**, *1161*, 246–253.

202. Zavabeti, A.; Ou, J. Z.; Carey, B. J.; Syed, N.; Orrell-Trigg, R.; Mayes, E. L. H.; Xu, C.; Kavehei, O.; O'Mullane, A. P.; Kaner, R. B.; Kalantar-Zadeh, K.; Daeneke, T. A Liquid Metal Reaction Environment for the Room-Temperature Synthesis of Atomically Thin Metal Oxides. Science 2017, 358 (6361), 332–335.

203. Mativenga, M.; An, S.; Jang, J. Bulk Accumulation a-IGZO TFT for High Current and Turn-On Voltage Uniformity. IEEE Electron Device Lett. 2013, 34 (12), 1533–1535.

204. Hwang, M. T.; Heiranian, M.; Kim, Y.; You, S.; Leem, J.; Taqieddin, A.; Faramarzi, V.; Jing, Y.; Park, I.; van der Zande, A. M.; Nam, S.; Aluru, N. R.; Bashir, R. Ultrasensitive Detection of Nucleic Acids Using Deformed Graphene Channel Field Effect Biosensors. Nat. Commun. 2020, 11 (1), 1543.